TU Delft

Delft University of Technology

Document Version
Final published version

Citation (APA)
Elalfy, M. H. I. (2026). *Beam-Based Postbuckling-Enabled Aeroelastic Tailoring of Composite Wingbox Structures*. [Dissertation (TU Delft), Delft University of Technology]. https://doi.org/10.4233/uuid:f42a691a-3bb6-4171-9609-8e944ac2bcb2

Important note
To cite this publication, please use the final published version (if applicable).
Please check the document version above.

Copyright
In case the licence states “Dutch Copyright Act (Article 25fa)”, this publication was made available Green Open Access via the TU Delft Institutional Repository pursuant to Dutch Copyright Act (Article 25fa, the Taverne amendment). This provision does not affect copyright ownership.
Unless copyright is transferred by contract or statute, it remains with the copyright holder.

Sharing and reuse
Other than for strictly personal use, it is not permitted to download, forward or distribute the text or part of it, without the consent of the author(s) and/or copyright holder(s), unless the work is under an open content license such as Creative Commons.

Takedown policy
Please contact us and provide details if you believe this document breaches copyrights.
We will remove access to the work immediately and investigate your claim.

This work is downloaded from Delft University of Technology.

Beam-Based Postbuckling-Enabled Aeroelastic Tailoring of Composite Wingbox Structures

Mohamed H. Elalfy

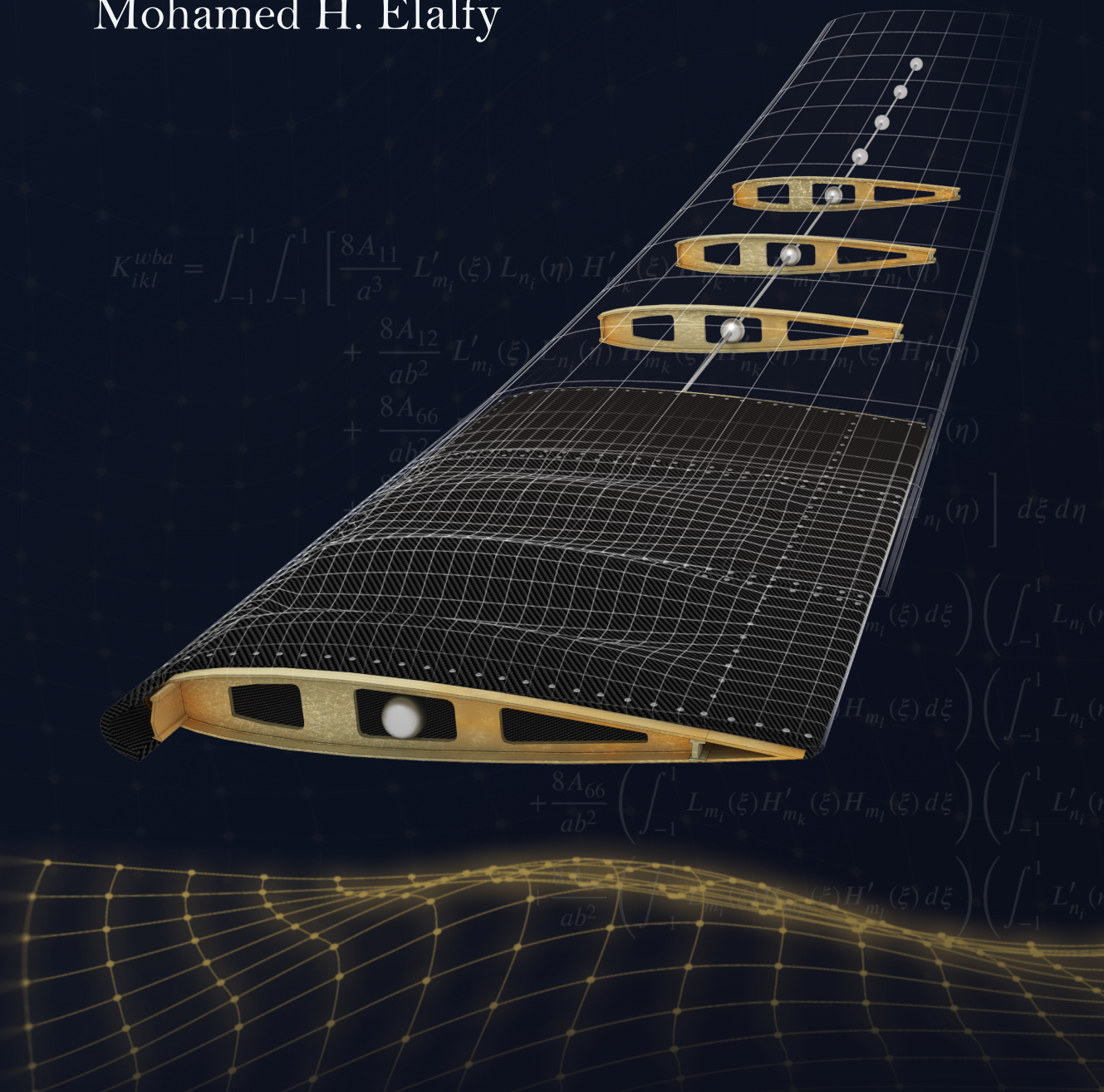

Beam-Based Postbuckling-Enabled Aeroelastic Tailoring of Composite Wingbox Structures

Beam-Based Postbuckling-Enabled Aeroelastic Tailoring of Composite Wingbox Structures

Dissertation

for the purpose of obtaining the degree of doctor at
Delft University of Technology
by the authority of the Rector Magnificus,
Prof.dr.ir. H. Bijl,
chair of the Board for Doctorates
to be defended publicly on
Wednesday, 30 September 2026 at 12:30

by

Mohamed Hassan Ibrahim ELALFY

This dissertation has been approved by the promotors.

Composition of the doctoral committee:

Rector Magnificus	Chairperson
Prof.dr.ir. R. De Breuker	Delft University of Technology, promotor
Dr.ir. S. Giovani Pereira Castro	Delft University of Technology, promotor
Independent members:	
Prof.dr.ir. R.C. Alderliesten	Delft University of Technology
Prof.dr. A. Pagani	Politecnico di Torino, Italy
Prof.dr. A. Pirrera	University of Bristol, UK
Dr. J. Sodja	Delft University of Technology
Dr.ir. E.L. Jansen	Rotterdam University of Applied Sciences
Prof.dr. K. Masania	Delft University of Technology, reserve member





Keywords: Postbuckling, Composite panels, Cross-sectional stiffness, Beam-based models, Aeroelastic tailoring, Structural mass minimisation

Front & Back: Cover designed by Ahmed Hady

Copyright © 2026 by M.H. Elalfy

ISBN 978-94-6518-442-5

An electronic version of this dissertation is available at
`http://repository.tudelft.nl/`.

For Mom, Dad, Rahma, Lana & Dr. Mostafa Abdalla

Preface

This dissertation is the result of four and a half years of research, and of the social and personal experiences that came with it. I consider it the most eventful period of my life, and the most stressful. In these years I got married, became a father, made friends, and said goodbye to someone who was dear to me. All of this has left its mark on the book in front of you. The book would not exist without the people who guided, accompanied, and supported me along the way.

Saullo, my promotor and daily supervisor, I cannot easily put into words how grateful I am, both technically and personally. You were patient with the problems that took longest to solve, and you always took the time to look into them with me and guide me through. You could tell when I was stressed or frustrated before I said anything, and you always put the person before the technicalities. When my daughter was born you were encouraging and understanding, and you understood what it takes to run a PhD alongside a family and to set priorities between them. You were never late to respond, and even during your holidays you were there whenever I needed you. I always felt free to talk to you about anything, and I enjoyed our conversations about life as much as our technical discussions.

Roeland, my promotor, you were my first contact with TU Delft, and I am grateful that you chose me for this position. Early in my PhD I took your course on aeroelasticity, one of the courses I enjoyed most. Your questions and feedback consistently sharpened my thinking and the direction of the work. You cared as much about how my personal life was going as about the progress of my PhD. I still remember the conversations we had in Florence about history, culture, and art, and the many others about football.

I would also like to thank the independent members of my doctoral committee, Prof.dr.ir. R.C. Alderliesten, Prof.dr. A. Pagani, Prof.dr. A. Pirrera, Dr. J. Sodja, and Dr.ir. E.L. Jansen, for the time they took to read this dissertation, for their feedback, and for taking part in the doctoral ceremony.

Dr. Mostafa Abdalla passed away on 22 July 2023. He taught me as an undergraduate and later supervised both my bachelor's graduation project and my master's thesis. I would not be here today without him. Even after I came to Delft, he stayed in touch and was always there whenever I wanted to discuss something. His scientific work will continue to inspire people, and so will the way he treated them. The same intelligence also ran through his sense of humour, and that combination is rare. I still miss our conversations.

Pedro and Alex, thank you for the discussions we had along the way and for the perspective you brought, and my thanks to Embraer for being part of this project.

I have been lucky to be surrounded by good people, more than I can name here. Hauke, we shared an office for most of those years, and you became a true friend. I enjoyed our coffee breaks and our discussions. When I was at my lowest you would

come and check on me without my asking, and you told me I was doing well when I did not think so. You saw the big events in my life over those years and were part of them. Xavi, thank you for your friendship and for your patience whenever I turned up and threw questions at you. You were always willing to help. Srikanth, we went through much of the same at the same time, and I valued our conversations about careers and personal priorities. Siddharth, you defended shortly before me, and having someone just ahead on the same road made the process easier. The new office was a good place to be. Ilias, we talked often about culture and history, and about how much Mediterranean cultures share, and I enjoyed the freddos you prepared. Evangelos, we worked with much of the same software, and you were always curious and ready to discuss it and to share what you knew about the code. Sam, you supported me through one of the toughest stretches of the PhD, and I still think back on the World Cup, the results sheet we kept in the corridor, and the walks we took outside.

Some of the friendships I value most from these years began outside my group. Raja, we met by chance over coffee one late evening, and we have been close ever since. You would call me in for coffee and something sweet in your office, and you never came back from anywhere without bringing something to share. Karim, we met at prayers, and we became close friends. You are one of the first people I would think of whenever I needed something, and you would offer before I asked. I enjoyed going out for lunch with you, both as a break from the workplace and for the thoughtful conversations. Hady, who I met through Karim and who has become a close friend, designed the cover of this book. Thank you for your patience in working out what I had in mind, for the many iterations it took to get there, and for teaching me a few things about design while we worked on it.

To my father and my mother, you carried my financial burdens through every year of my education, right up to the start of this PhD, and your prayers carried me through the rest. I know you worried about me as much as I worried about myself, and from further away. To my brother, whenever something went wrong you were the one who took care of it, and knowing that made the distance easier to bear. To my sister, you took me into your home for the whole of my bachelor's and looked after everything, the way our mother would have, and I have not forgotten it. I owe you all where I am today.

Rahma, my love, you left a settled career behind in Egypt to come here with me, to a new place with no friends, a different climate and culture, and no clear path of your own. What you gave up has not been replaced here, and you never once made me feel the weight of it. You carried the pressure of these years and the first two years of raising Lana at the same time. You believed in me more than I did. You were the one I relied on, the one I turned to, and the one I could bring anything to. Thank you.

Lana, you arrived in the middle of all this, and for all the effort it took you gave us back more.

Mohamed Elalfy
Delft, September 2026

Summary

The structural design of composite aircraft wings in aeroelastic optimisation frameworks is conventionally governed by a linear buckling constraint, which restricts the structural response to the pre-buckling regime across all prescribed load cases. This constraint has been shown to emerge as the active design driver in mass minimisation studies, yet it is conservative. Stiffened thin-walled composite panels are capable of sustaining load beyond the onset of buckling through stable postbuckling behaviour, and this reserve capacity remains inaccessible in conventional design practice. The consistent incorporation of postbuckling behaviour within a computationally efficient aeroelastic optimisation framework had not been realised prior to this work. This dissertation addresses that gap through three sequential contributions.

The first contribution is a semi-analytical method for predicting the postbuckling stiffness of laminated composite plates. The method is based on the Rayleigh–Ritz approach, using hierarchical polynomial shape functions as the Ritz basis. This choice accommodates general boundary conditions and yields closed-form analytical expressions for all strain-energy integrals through polynomial recurrence relations, eliminating the need for numerical integration. Two solution strategies are presented and validated against high-fidelity reference solutions: a perturbation-based approach that provides a rapid approximation of the postbuckling stiffness near the onset of buckling, and an iterative path-following scheme that traces the nonlinear equilibrium path deeper into the postbuckling regime.

The second contribution is a methodology for incorporating local panel postbuckling stiffness degradation within the cross-sectional stiffness matrix of a one-dimensional Timoshenko beam model. The panel-level stiffness reduction is integrated into the cross-section modeller, producing a degraded beam stiffness matrix that reflects the buckled state of the individual panels. The methodology is verified against nonlinear shell-based reference analyses for a range of wingbox configurations, confirming that buckling onset and the subsequent postbuckling load-displacement response are captured consistently up to the onset of cross-sectional sagging.

The third contribution integrates the developed postbuckling methodology within a reduced-order beam-based aeroelastic optimisation framework and applies it to the FLEXOP demonstrator wing. A buckling-constrained reference design is compared against a postbuckling-enabled design, with an intermediate case included to isolate the effect of constraint removal from the effect of physically consistent postbuckling stiffness degradation. Gradient-based optimisation is performed with lamination parameters and panel thicknesses as design variables, subject to strain, aeroelastic stability, angle of attack, and lamination parameter feasibility constraints.

The results establish four principal conclusions. First, for the demonstrator wing and load cases considered, the conventional buckling constraint imposes a substan-

tial mass penalty: removing it while retaining physically consistent postbuckling physics reduces structural mass by approximately 50% relative to the conventional reference. Second, physical consistency is required to obtain a valid design: without postbuckling stiffness degradation, the structural response under load is underestimated, so the resulting design is not sized against the response it would actually exhibit. Third, incorporating postbuckling physics shifts the governing failure mode from buckling in the conventional reference design to material strength failure in the physically consistent postbuckling design, driven by the elevated strain levels produced by panel stiffness degradation. Fourth, the aeroelastic response of the postbuckling-enabled design differs substantially from that of the unconstrained design at equivalent structural mass. This demonstrates that panel stiffness degradation modifies the aeroelastic response independently of the mass reduction associated with constraint removal.

Collectively, the work demonstrates that postbuckling behaviour can be incorporated within a computationally efficient, gradient-based aeroelastic optimisation framework. Panel-level stiffness degradation is computed semi-analytically, embedded into the beam cross-sectional stiffness matrix, and incorporated into the aeroelastic response. The results establish that postbuckling-enabled aeroelastic tailoring can substantially reduce the structural mass of composite wings while maintaining a physically consistent and aeroelastically stable design.

Samenvatting

Het structurele ontwerp van composieten vliegtuigvleugels in raamwerken voor aeroelastische optimalisatie wordt normaliter bepaald door een lineaire plooibeperking, die de analyse beperkt tot het pre-plooiregime voor de voorgeschreven belastingssituaties. Deze nevenvoorwaarde is de bepalende ontwerpfactor in het minimaliseren van de massa, maar is tegelijkertijd conservatief. Dunwandige, verstijfde composieten panelen zijn in staat om krachten te dragen nadat het paneel plooit, maar dit wordt niet meegenomen in traditionele ontwerpen. Voor deze thesis bestond er nog geen efficiënt aeroelastisch optimalisatieraamwerk dat post-plooigedrag op een consistente manier meeneemt. In deze dissertatie wordt deze onderzoekslacune gedicht door drie sequentiële bijdragen.

De eerste bijdrage is een semi-analytische methode voor het voorspellen van de post-plooistijfheid van gelamineerde, composieten panelen. De methode is gebaseerd op de Rayleigh-Ritz methode, waar gebruik wordt gemaakt van hiërarchische polynomische vormfuncties als basis. Deze keuze is geschikt voor generieke randvoorwaarden en resulteert in analytische uitdrukkingen in gesloten vorm voor alle integralen van de rek-energie, dankzij de polynomische recurrentierelaties. De dissertatie beschrijft twee oplossingsstrategieën en valideert deze aan de hand van nauwkeurige referentieoplossingen. De eerste methode gebruikt een kleine verstoring om snel de post-plooistijfheid te schatten bij het begin van de plooi. De andere methode gebruikt een iteratief padvolgend algoritme om het niet-lineaire gedeelte van het evenwichtspad te volgen verder in het post-plooiregime.

De tweede bijdrage is een methodologie voor het meenemen van de lokale post-plooistijfheid in de stijfheidsmatrix horend bij de doorsnede van een één-dimensionaal Timoshenko-balkmodel. De stijfheidsafname van het paneel is geïntegreerd in het doorsnede-model, wat een gedegradeerde balkstijfheidsmatrix oplevert, passend bij de geplooide staat van de panelen. De methodologie wordt geverifieerd met niet-lineaire referentieanalyses op basis van schaalelementen, voor een scala aan vleugeldoosconfiguraties. Dit bevestigt dat de aanvang van het plooien van de panelen, en de post-plooi last-verplaatsingsresponse consistent worden voorspeld, tot aan het begin van het inzakken van de dwarsdoorsnede.

De derde bijdrage integreert de ontwikkelde post-plooimethodologie in een gereduceerde-orde balkgebaseerd aeroelastisch optimalisatieraamwerk, en past het toe op de FLEXOP demonstratievleugel. Een plooibeperkt referentieontwerp wordt vergeleken met een ontwerp waarbij post-plooien is toegestaan. Een tussenliggend geval is opgenomen om het effect van het verwijderen van de nevenvoorwaarde te isoleren ten opzichte van de fysisch consistente post-plooistijfheidsdegradatie.

Deze resultaten leiden tot vier belangrijke conclusies. In de eerste plaats, de traditionele plooibeperking leidt tot een substantiële massaverhoging; het verwijderen van deze beperking en tegelijkertijd het in acht nemen van de post-plooifysica,

resulteert in een massaverlaging van ongeveer 50% ten opzichte van het referentieontwerp. Ten tweede, fysische consistentie is vereist om een valide ontwerp te verkrijgen: zonder post-plooistijfheidsdegradatie wordt de structurele respons onderschat en kunnen de krachten niet worden weerstaan door het resulterende ontwerp. Ten derde, het meenemen van post-plooifysica verschuift de dominante faalmodus van plooien in het referentieontwerp naar materiaalsterkte, dankzij de verhoogde rek door de verlaagde paneelstijfheid. Ten vierde, de aeroelastische respons van het post-plooiontwerp wijkt wezenlijk af van het niet-beperkte ontwerp bij een gelijkwaardige structurele massa. Dit toont aan dat paneelstijfheidsdegradatie een krachtenherverdeling veroorzaakt, onafhankelijk van de massaverlaging die wordt bereikt door het verwijderen van beperkingen.

Alles tezamen toont dit werk aan dat post-plooigedrag meegenomen kan worden in een efficiënt, gradiëntgebaseerd aeroelastisch optimalisatieraamwerk. Paneelstijfheidsdegradatie wordt semi-analytisch berekend; wordt meegenomen in de dwarsdoorsnedestijfheidsmatrix van de balk; en wordt meegenomen in de aeroelastische respons. De resultaten stellen vast dat aeroelastische aanpassingen, gebaseerd op post-plooigedrag, de structurele massa van composieten vleugels significant kan verlagen, terwijl een fysisch consistent en aeroelastisch stabiel ontwerp behouden blijft.

Nomenclature

Roman Symbols

a_i	Ritz parameters associated with ϕ_i^w
$\boldsymbol{a}$	Buckling mode shape
A	Plate in-plane dimension in the x-direction
A_{ij}	Membrane stiffness matrix terms
A_{ij}^{PB}	Degraded membrane stiffness terms in the postbuckling regime
AR	Aspect ratio, $AR = A/B$
b_i	Ritz parameters associated with ϕ_i^u
B	Plate in-plane dimension in the y-direction
$\mathbf{B}_0, \mathbf{B}_1$	Kinematic operators
c_i	Ritz parameters associated with ϕ_i^v
$\mathbf{C}$	Constitutive matrix
D_{ij}	Bending stiffness matrix terms
e_{x0}, e_{y0}	Strains applied at the plate edges
E_{11}, E_{22}	Longitudinal and transverse Young's moduli
g_{xy0}	Shear strain applied at the plate edges
g_{aoa}	Angle of attack constraint
g_{buc}	Buckling constraint
g_{lp}	Lamination parameter feasibility constraint
g_{stab}	Aeroelastic stability constraint
g_{str}	Strain constraint
G_{12}	In-plane shear modulus
h^k	Panel thickness of design region k
$h_{\min}, h_{\max}$	Minimum and maximum allowable panel thickness
H_i	Integral of the Lobatto polynomials
$\mathbf{J}$	Aeroelastic Jacobian
$\mathbf{K}$	Panel elastic stiffness matrix
$\mathbf{K}_{\mathrm{cs}}$	Cross-sectional Timoshenko stiffness matrix
$\mathbf{K}_g$	Panel geometric stiffness matrix
L	Total lift
L_i	Lobatto polynomials
m	Number of half waves in the x-direction; polynomial degree index in ζ
$m(\boldsymbol{x})$	Structural mass of the wingbox
n	Number of half waves in the y-direction; polynomial degree index in η

N	Number of terms retained in the Ritz expansion
N_0	Analytical critical buckling load
N_r	Number of design regions
N_x, N_y, N_{xy}	In-plane stress resultants
$\bar{N}_x, \bar{N}_y, \bar{N}_{xy}$	Average force resultants at the plate edges
P_i	Legendre polynomials
$\boldsymbol{p}$	Generalised momenta (Chapter 3); structural degrees of freedom (Chapter 4)
$\boldsymbol{q}$	Cross-sectional displacement vector
r_{buc}	Inverse buckling factor
r_{str}	Strain failure index
$\boldsymbol{R}_0$	Aeroelastic residual
t_{ply}	Ply thickness
u, v, w	Displacement components
u_0, v_0	Displacements applied at the edges $x = A$ and $y = B$
V	Volume
V_{iA}, V_{iD}	Membrane and bending lamination parameters
V_{onset}	Velocity at the onset of panel buckling
W	Work done by external forces (Chapter 3); aircraft weight (Chapter 4)
$\boldsymbol{x}$	Design variable vector
x, y, z	Cartesian coordinates

GREEK SYMBOLS

α	Angle of attack
$\alpha_{\max}$	Maximum allowable angle of attack
γ^0_{xy}	Midplane shear strain
δ	Perturbation parameter controlling the offset from the equilibrium path
ϵ	Perturbation expansion parameter
$\epsilon^0_x, \epsilon^0_y$	Midplane direct strains
$\boldsymbol{\varepsilon}$	Strain vector
ζ	Natural coordinate, $\zeta = 2x/A - 1$
η	Natural coordinate, $\eta = 2y/B - 1$
$\theta(z)$	Local ply orientation through the laminate thickness
$\kappa_x, \kappa_y, \kappa_{xy}$	Curvatures
λ	Scaling factor applied to the edge strains
λ_{cr}	Critical multiplier for the applied edge displacement
λ_f	Full strain multiplier at which the average resultant forces are evaluated
λ_i	Eigenvalues of the aeroelastic state matrix
ν	Poisson's ratio
ξ	Polynomial argument on the reference domain
Π	Total potential energy

$\boldsymbol{\sigma}$	Stress vector
$\phi_i^u, \phi_i^v, \phi_i^w$	Shape functions
$\boldsymbol{\phi}$	Null-space vector

SUB/SUPERSCRIPTS

cr	Critical, at buckling onset
cs	Cross-sectional
f	Full
max	Maximum
min	Minimum
0	Midplane quantity
PB	Postbuckling quantity
$(1), (2)$	First- and second-order perturbation quantities
$\overline{(\cdot)}$	Average over the plate edge
$(\cdot)^\top$	Transpose
$(\cdot)_{,x}$	Partial differentiation with respect to x

Contents

Preface v

Summary vii

Samenvatting ix

Nomenclature xi

1 Introduction 1
- 1.1 Motivation . . . 1
- 1.2 State of the Art . . . 3
- 1.3 Research Questions . . . 4
- Bibliography . . . 5

2 An Efficient Semi-Analytical Approach for Postbuckling Analysis of Laminated Composite Plates with Straight Edges 9
- 2.1 Introduction . . . 10
- 2.2 Problem Definition . . . 12
- 2.3 Hierarchical Polynomial Properties . . . 15
- 2.4 Solution to Equilibrium Equations . . . 17
- 2.5 Results . . . 20
- 2.6 Conclusion . . . 29
- Bibliography . . . 31
- Appendix . . . 37

3 Beam-like models for the post-buckling behaviour of wingbox structures 51
- 3.1 Introduction . . . 52
- 3.2 Methodology . . . 54
- 3.3 Results and Discussion . . . 60
- 3.4 Conclusion . . . 68
- Bibliography . . . 69
- Appendix . . . 73

4 Postbuckling-Enabled Aeroelastic Wing Optimisation 87
- 4.1 Introduction . . . 88
- 4.2 Methodology . . . 89
- 4.3 Results . . . 97
- 4.4 Conclusion . . . 105
- Bibliography . . . 108

5 Conclusion and Future Research **111**
5.1 Conclusions 111
5.2 Future Research 114
Bibliography 117

Curriculum Vitæ **119**

1

Introduction

1.1. Motivation

The primary structure of commercial aircraft has advanced through a succession of introductions of new material systems and structural concepts, from the all-metal stressed skin to the fibre metal laminate and the composite wingbox, as shown in Figure 1.1. Although this evolution has yielded significant advances, considerable potential for structural efficiency gains remains unexploited.

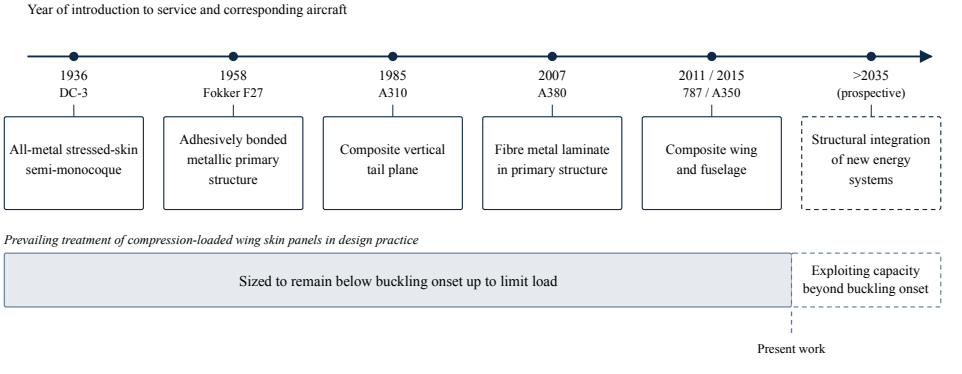

Figure 1.1: Representative introductions of new material systems and structural concepts into primary airframe structure, shown against the prevailing treatment of compression-loaded wing skin panels in design practice.

The semi-monocoque construction made the skin a load-carrying member, with the skin, frames, and stringers acting together to carry and distribute the applied loads. Adhesive bonding became an important joining technology alongside mechanical fastening (Higgins, 2000), and fibre metal laminates were subsequently developed at Delft University of Technology, with early structural work focusing on wing panels (Vermeeren, 2003). The bonded metal-composite layup allows the fibre

layers to bridge cracks developing in the metallic layers, retarding crack growth and improving damage tolerance relative to a monolithic metallic structure.

The use of composite materials has since extended to the complete primary load path of the wing. In a laminated composite, fibre orientations can be selected to align stiffness with the primary load directions (Kassapoglou, 2010). This freedom is exploitable where the principal load directions are well defined, as in a wingbox loaded predominantly in bending and torsion. It enables aeroelastic tailoring, in which the structural deformation response under aerodynamic loading is deliberately shaped to improve aeroelastic performance (Shirk et al., 1986, Weisshaar and Duke, 2006). Aeroelastic tailoring has been demonstrated extensively in composite wing design and is exploited within modern aeroelastic optimisation frameworks (De Breuker, 2011, Werter and De Breuker, 2016, Sodja et al., 2018, Dillinger et al., 2019).

Within these frameworks, buckling is consistently imposed as a design constraint, restricting the structural response to the pre-buckling regime across all prescribed load cases (Sodja et al., 2018, Dillinger et al., 2019). This constraint is conservative. Some thin-walled composite structures are capable of sustaining load beyond the onset of buckling through stable postbuckling behaviour (Kassapoglou, 2010, Singer et al., 2003). Stiffened panels, in particular, can exhibit a stable postbuckling path, in which local skin buckling precedes collapse by a factor of two or more (Falzon et al., 2000, Zimmermann et al., 2006). The ultimate failure load can significantly exceed the initial buckling load, indicating that substantial load-carrying capacity remains available beyond buckling onset (Falzon et al., 2000, Murphy et al., 2005, Zimmermann et al., 2006, Zhang et al., 2024). The POSICOSS and COCOMAT projects identified this reserve in composite stiffened airframe structures, establishing the exploitation of the postbuckling regime as a necessary step towards more structurally efficient airframe designs (Zimmermann et al., 2006, Degenhardt et al., 2006).

The load-carrying capacity of composite wing structures therefore remains only partly exploited, since sizing panels to remain below buckling onset limits the design to the stable pre-buckling regime rather than to failure. Exploiting the reserve beyond that limit raises the structural efficiency these structures achieve. The case is stronger for hydrogen-fuelled and battery-electric designs, which introduce fundamentally different structural demands, including large cryogenic tank volumes, high energy mass fractions, and unconventional load distributions. These demands make exploiting the reserve a structural necessity (Tiwari et al., 2024, de Vries et al., 2024). Removing the buckling constraint and permitting panels to operate beyond buckling onset has the potential to reduce structural mass significantly, enabling designs that meet the structural efficiency required by future aircraft configurations. This dissertation presents a methodology for exploiting the load-carrying capacity beyond buckling onset and quantifies its effect on the structural mass of composite wings. Postbuckling behaviour is incorporated within a computationally efficient aeroelastic optimisation framework to enable this quantification.

1.2. State of the Art

Composite wing optimisation frameworks, from high-fidelity shell-based approaches to reduced-order beam-based methods, have predominantly treated buckling as a hard design constraint. In high-fidelity aerostructural optimisation, for example, Kenway et al. (2014) imposed panel-level buckling constraints across wingbox components including skins and spars, while Stodieck et al. (2017) imposed it in a composite tailoring framework based on a three-dimensional finite element wingbox model. In reduced-order beam-based frameworks, buckling is similarly imposed as one of several structural constraints in mass minimisation, including (Othman et al., 2019, Sodja et al., 2018, Dillinger et al., 2019). In Sodja et al. (2018), buckling emerges as the first active constraint in the optimisation process, directly governing panel thicknesses and laminate stiffness distributions. The load-carrying capacity available beyond buckling onset therefore remains unexploited in these designs.

Accurate prediction of postbuckling behaviour is well established experimentally and analytically, but the direct coupling of nonlinear postbuckling analysis with optimisation schemes carries a computational cost driven by the need for repeated nonlinear equilibrium evaluations. This has so far prevented its direct use within aeroelastic optimisation frameworks (Bisagni and Lanzi, 2002, Mitrotta et al., 2025). Reduced-order alternatives, including asymptotic Koiter-based methods and surrogate models, alleviate this cost but rely on assumptions that limit their generality and restrict their applicability to specific boundary conditions or design spaces (Henrichsen et al., 2016, Bisagni and Lanzi, 2002). This motivates the need for computationally efficient postbuckling models suitable for integration within aeroelastic optimisation frameworks, where repeated evaluations are required.

A limited number of studies have incorporated postbuckling within structural optimisation, demonstrating potential for mass reduction (Qu et al., 2012, Daoud and Calomfirescu, 2010, Moors et al., 2019). These studies, however, are limited to structural optimisation and do not account for the aeroelastic coupling that postbuckling stiffness degradation introduces.

High-fidelity aeroelastic analyses have demonstrated that postbuckling modifies the structural response and flutter characteristics of composite wings (De Oliveira et al., 2014), and more recent work has shown that the conventional treatment of buckling as a hard constraint imposes a quantifiable mass penalty even in a purely structural context (Mitrotta et al., 2025). These studies rely on computationally expensive nonlinear solution strategies that are incompatible with the repeated coupled analyses required within aeroelastic optimisation loops. An efficient method for predicting postbuckling stiffness, suitable for the repeated evaluations demanded by optimisation, is therefore lacking. The extension to coupled aeroelastic optimisation is furthermore identified as an open problem, and the consistent incorporation of postbuckling within a computationally efficient, coupled aeroelastic optimisation framework remains unaddressed.

1.3. Research Questions

The gap identified above is addressed through the following research questions:

1. How can the postbuckling stiffness of locally buckled composite panels be predicted efficiently under general boundary conditions, for integration within low-fidelity aeroelastic optimisation frameworks for conceptual design?

2. How can local panel postbuckling be represented within a beam-like model of a wingbox structure, and what are the limitations of such a low-fidelity representation in capturing the three-dimensional postbuckling response?

3. What is the effect of allowing postbuckling on the structural mass and aeroelastic response of composite wings optimised within a coupled aeroelastic framework?

The remainder of this dissertation is structured as follows. Chapter 2 addresses Research Question 1 (RQ1) by presenting a semi-analytical postbuckling formulation for composite plates based on hierarchical polynomials, which yields closed-form expressions for the postbuckling stiffness under general boundary conditions. Chapter 3 addresses RQ2 by developing a methodology to incorporate local panel postbuckling stiffness degradation within the cross-sectional stiffness matrix of a one-dimensional Timoshenko beam model, and examines the limitations of this low-fidelity representation against high-fidelity shell-based analyses. Chapter 4 addresses RQ3 by embedding the postbuckling model within Proteus, a reduced-order beam-based aeroelastic optimisation framework developed at TU Delft, and applying it to the FLEXOP demonstrator wing (Sodja et al., 2018) through a controlled three-case optimisation study.

Bibliography

C. Bisagni and L. Lanzi. Post-buckling optimisation of composite stiffened panels using neural networks. *Composite Structures*, 58(2):237–247, 2002. ISSN 0263-8223. doi: https://doi.org/10.1016/S0263-8223(02)00053-3.

F. Daoud and M. Calomfirescu. Optimization of composite aircraft structures in consideration of postbuckling behavior. In *International Journal of Structural Stability and Dynamics*, volume 10, pages 905–916, 10 2010. doi: 10.1142/S0219455410003804.

R. De Breuker. *Energy-based Aeroelastic Analysis and Optimisation of Morphing Wings*. PhD thesis, Delft University of Technology, 2011.

L. C. De Oliveira, R. Degenhardt, and T. Klimmek. Aeroelastic behavior of composite wings in post buckling regime. *29th Congress of the International Council of the Aeronautical Sciences, ICAS 2014*, pages 1–8, 2014.

R. de Vries, R. E. Wolleswinkel, M. Hoogreef, and R. Vos. A new perspective on battery-electric aviation, part ii: Conceptual design of a 90-seater. In *AIAA SCITECH 2024 Forum*. American Institute of Aeronautics and Astronautics, Jan. 2024. doi: 10.2514/6.2024-1490.

R. Degenhardt, R. Rolfes, R. Zimmermann, and K. Rohwer. COCOMAT - Improved material exploitation of composite airframe structures by accurate simulation of postbuckling and collapse. *Composite Structures*, 73(2):175–178, 5 2006. ISSN 02638223. doi: 10.1016/j.compstruct.2005.11.042.

J. K. S. Dillinger, M. M. Abdalla, Y. M. Meddaikar, and T. Klimmek. Static aeroelastic stiffness optimization of a forward swept composite wing with cfd-corrected aero loads. *CEAS Aeronautical Journal*, 10(4):1015–1032, May 2019. ISSN 1869-5590. doi: 10.1007/s13272-019-00397-y.

B. Falzon, K. Stevens, and G. Davies. Postbuckling behaviour of a blade-stiffened composite panel loaded in uniaxial compression. *Composites Part A: Applied Science and Manufacturing*, 31(5):459–468, 2000. ISSN 1359-835X. doi: https://doi.org/10.1016/S1359-835X(99)00085-8.

S. R. Henrichsen, P. M. Weaver, E. Lindgaard, and E. Lund. Post-buckling optimization of composite structures using koiter's method. *International Journal for Numerical Methods in Engineering*, 108(8):902–940, 2016. doi: https://doi.org/10.1002/nme.5239.

A. Higgins. Adhesive bonding of aircraft structures. *International Journal of Adhesion and Adhesives*, 20(5):367–376, 2000. ISSN 0143-7496. doi: https://doi.org/10.1016/S0143-7496(00)00006-3.

C. Kassapoglou. *Design and Analysis of Composite Structures: With Applications to Aerospace Structures*. Wiley, Sept. 2010. ISBN 9780470972700. doi: 10.1002/9780470972700.

G. K. Kenway, J. R. Martins, and G. J. Kennedy. Aerostructural optimization of the common research model configuration. In *AIAA AVIATION 2014 -15th AIAA/ISSMO Multidisciplinary Analysis and Optimization Conference*. American Institute of Aeronautics and Astronautics Inc., 2014. ISBN 9781624102837. doi: 10.2514/6.2014-3274.

F. Mitrotta, A. Pirrera, T. Macquart, J. Cooper, A. Pereira do Prado, and P. Higino Cabral. Proof of concept of a nonlinear structural stability constraint for aeroelastic optimisation. *The Aeronautical Journal*, 129(1335):1237–1264, 2025. doi: 10.1017/aer.2024.151.

G. Moors, C. Kassapoglou, S. F. M. de Almeida, and C. A. E. Ferreira. Weight trades in the design of a composite wing box: effect of various design choices. *CEAS Aeronautical Journal*, 10(2):403–417, 6 2019. ISSN 18695590. doi: 10.1007/s13272-018-0321-4.

A. Murphy, M. Price, C. Lynch, and A. Gibson. The computational post-buckling analysis of fuselage stiffened panels loaded in shear. *Thin-Walled Structures*, 43 (9):1455–1474, 2005. ISSN 0263-8231. doi: https://doi.org/10.1016/j.tws.2005.03.010.

M. F. Othman, G. H. Silva, P. H. Cabral, A. P. Prado, A. Pirrera, and J. E. Cooper. A robust and reliability-based aeroelastic tailoring framework for composite aircraft wings. *Composite Structures*, 208:101–113, 1 2019. ISSN 02638223. doi: 10.1016/j.compstruct.2018.09.086.

S. Qu, D. Kennedy, and C. A. Featherston. A multilevel framework for optimization of an aircraft wing incorporating postbuckling effects. *Proceedings of the Institution of Mechanical Engineers, Part G: Journal of Aerospace Engineering*, 226(7): 830–845, 7 2012. ISSN 0954-4100. doi: 10.1177/0954410011415158.

M. H. Shirk, T. J. Hertz, and T. A. Weisshaar. Aeroelastic tailoring - theory, practice, and promise. *Journal of Aircraft*, 23(1):6–18, 1986. doi: 10.2514/3.45260.

A. Singer, J, A. Arbocz, J, A. Weller, T, and R. Cheney, JA. Buckling Experiments: Experimental Methods in Buckling of Thin-Walled Structures. Shells, Built-up Structures, Composites and Additional Topics, Volume 2. *Applied Mechanics Reviews*, 56(1):B5–B5, 01 2003. ISSN 0003-6900. doi: 10.1115/1.1523358.

J. Sodja, N. P. Werter, and R. De Breuker. Design of a flying demonstrator wing for manoeuvre load alleviation with cruise shape constraint. In *AIAA/ASCE/AHS/ASC Structures, Structural Dynamics, and Materials Conference, 2018*, number 210049. American Institute of Aeronautics and Astronautics Inc, AIAA, 2018. ISBN 9781624105326. doi: 10.2514/6.2018-2153.

O. Stodieck, J. E. Cooper, P. M. Weaver, and P. Kealy. Aeroelastic tailoring of a representative wing box using tow-steered composites. *AIAA Journal*, 55:1425–1439, 2017. ISSN 00011452. doi: 10.2514/1.J055364.

S. Tiwari, M. J. Pekris, and J. J. Doherty. A review of liquid hydrogen aircraft and propulsion technologies. *International Journal of Hydrogen Energy*, 57:1174–1196, 2024. ISSN 0360-3199. doi: https://doi.org/10.1016/j.ijhydene.2023.12.263.

C. A. J. R. Vermeeren. An historic overview of the development of fibre metal laminates. *Applied Composite Materials*, 10:189–205, 2003. doi: 10.1023/A:1025533701806.

T. A. Weisshaar and D. K. Duke. Induced drag reduction using aeroelastic tailoring with adaptive control surfaces. *Journal of Aircraft*, 43(1):157–164, 2006. doi: 10.2514/1.12040.

N. P. Werter and R. De Breuker. A novel dynamic aeroelastic framework for aeroelastic tailoring and structural optimisation. *Composite Structures*, 158:369–386, 12 2016. ISSN 02638223. doi: 10.1016/j.compstruct.2016.09.044.

G. Zhang, Y. Hu, B. Yan, M. Tong, and F. Wang. Buckling and post-buckling analysis of composite stiffened panels: A ten-year review (2014–2023). *Thin-Walled Structures*, 205:112525, 2024. ISSN 0263-8231. doi: https://doi.org/10.1016/j.tws.2024.112525.

R. Zimmermann, H. Klein, and A. Kling. Buckling and postbuckling of stringer stiffened fibre composite curved panels - tests and computations. *Composite Structures*, 73:150–161, 5 2006. ISSN 02638223. doi: 10.1016/j.compstruct.2005.11.050.

2

An Efficient Semi-Analytical Approach for Postbuckling Analysis of Laminated Composite Plates with Straight Edges

Postbuckling in thin-walled aircraft structures can lead to a redistribution of loads while the structure continues to carry load. This behaviour is particularly important in stiffened panels, where local buckling does not necessarily imply failure. Accurately modelling this behaviour is essential, but the analysis is often computationally expensive. A computationally efficient methodology is developed to predict postbuckling behaviour, supporting preliminary design and multidisciplinary optimisation of aerospace structures. The formulation is based on the Rayleigh–Ritz method using hierarchical polynomials as shape functions. These polynomials enable closed-form integration of the energy functional and allow the application of various boundary conditions. Two solution schemes are implemented: a perturbation-based expansion and an iterative correction method based on the Normal Flow Algorithm. The solutions are verified against results from the literature and finite element simulations. Results show that the methodology accurately predicts postbuckling behaviour while substantially reducing computational cost. The efficiency and flexibility in modelling different boundary conditions make the approach well-suited for integration into structural design and optimisation frameworks that require repeated postbuckling evaluations.

This chapter is based on: M. H. Elalfy, R. De Breuker, and S. G. P. Castro, "An efficient semi-analytical approach for postbuckling analysis of laminated composite plates with straight edges," *Thin-Walled Structures*, vol. 222, p. 114394, 2026. doi:10.1016/j.tws.2025.114394

2.1. Introduction

Thin-walled aircraft structures are expected to experience instability as a dominant failure mode (Grisham, 1978). A typical airframe is made of multiple elements that may undergo instability separately or collectively, referred to as local and global buckling, respectively. These structures are mainly composed of a thin skin reinforced by ribs and stringers. The skin is more likely to buckle locally between the reinforcements, usually carrying significant load after buckling (Grisham, 1978). When a panel buckles locally, its stiffness is reduced, and there is load redistribution towards the edges supported by reinforcements, and to the reinforcements themselves, up to the point where strength-driven failure modes become active.

Early attempts to estimate postbuckling stiffness relied on simplified analytical or reduced-order formulations for metallic and composite panels. Grisham (1978) introduced a prestrain-based procedure that implicitly captured stiffness degradation, while VICONOPT (Williams et al., 1991) and the extension by Anderson (1997) applied constant reduction factors to the initial stiffness matrix. Similar ideas underlie the effective-width formulations used by Collier et al. (2002) and later implemented in HyperSizer® (Collier et al., 2009), where portions of the cross-section assumed to have lost load-carrying capacity are discounted. These approaches are computationally efficient, but they rely on simplifying assumptions and are typically restricted to idealized boundary conditions or specific load cases.

Möcker and Reimerdes (2006), within the POSICOSS project, proposed a strip-element formulation to reduce the number of degrees of freedom and computational time. Trigonometric functions were used as shape functions to represent displacements in simply supported panels. While efficient, the method required a large number of terms to accurately capture postbuckling behaviour, which increased the overall cost. Moreover, the use of trigonometric functions limited the applicability to simply supported boundary conditions. Surrogate and response-surface models (Rikards et al., 2006, Lanzi and Giavotto, 2006) offered additional speed by approximating nonlinear behaviour from a limited number of simulations, though are restricted by the design space and specific load cases. Analytical expressions tailored to specific geometries, such as the omega-stringer formulation of Schilling and Mittelstedt (2023) and the outstand-plate solution of Becque (2022), highlight the potential of simplified, geometry-specific approximations, albeit with limited generality.

Parallel to these efforts, analytical and perturbation-based methods have provided deeper insight into the initial postbuckling regime. The classical asymptotic framework introduced by Koiter (1967) provided the foundation for the analysis of the initial postbuckling behaviour of elastic structures. Building on this framework, Arbocz and Hol (1990) extended the theory to account for modal interactions and imperfection sensitivity, while Castro and Jansen (2021) later developed a displacement-based formulation that formalised Koiter's reduced-order structure for composite plate applications. Koiter–Newton hybrid formulations for composite plates, such as the method of Liang et al. (2014), embed Koiter's asymptotic framework within iterative solution schemes to improve robustness in practice. Accelerated Koiter-based algorithms (Sun et al., 2020) have further been proposed to

enhance convergence efficiency in the neighbourhood of critical points. Perturbation-based analytical solutions have also been applied to laminated plates, such as the formulation of Hui-shen (1990), where the deflection amplitude is used as the perturbation parameter to derive closed-form expressions for simply supported configurations.

Taheri and Moradi (2000) proposed the differential quadrature method (DQM) to solve geometrically nonlinear problems, thus suitable for postbuckling analysis. The authors coupled DQM with an arc-length continuation technique to solve the von Kármán plate equations, including initial imperfections. They demonstrated that with relatively few grid points, DQM could accurately reproduce the post-buckling load–deflection path of composite plates, in good agreement with finite element results. Raju et al. (2013) applied the DQM for variable-angle tow laminates, and White et al. (2014) used DQM for initial post-buckling analysis of this class of composites. Liu et al. (2025) have also applied DQM for initial post-buckling of composites in their recent study, focusing on lattice shells with axially varying stiffness. Ansari et al. (2020), and Lv et al. (2023), applied DQM to study thermal post-buckling on functionally graded composites.

Semi-analytical formulations have long offered a balance between physical fidelity and computational efficiency in nonlinear analysis of composite plates. Milazzo and Oliveri (2017) proposed a Rayleigh–Ritz formulation based on First-Order Shear Deformation Theory for stiffened and variable-angle tow composite plates with cracks and delaminations. They used Legendre polynomials as trial functions and Gauss–Legendre quadrature to evaluate the integrals of the energy terms. Semi-analytical solutions have also been developed for specialised configurations, including the postbuckling formulations for infinitely long anisotropic plates proposed by Diaconu and Weaver (2006) and further explored in their earlier approximate Galerkin-based formulation (Diaconu and Weaver, 2005), both of which employ assumed-mode representations to capture the nonlinear response. Bisagni and Vescovini (2009) developed a variational Ritz formulation for stiffened composite panels that yields a closed-form expression for the linear buckling load, with the out-of-plane displacement coupled to the Airy stress function. The subsequent post-buckling response is obtained through Newton–Raphson iterations, and numerical integration remains necessary for some nonlinear terms. More recently, Dillen and Mittelstedt (2025) developed a non-dimensional Ritz formulation for simply supported composite plates with bending–twisting coupling, combining orthogonalised polynomial trial functions with an efficient integral-evaluation scheme to improve the accuracy and robustness of postbuckling predictions. Complementary to these modelling efforts, Köllner and Lüer (2025) proposed a path-following framework formulated at the level of the total potential energy, which provides an efficient means of tracing nonlinear equilibrium paths in semi-analytical plate formulations.

This work is motivated by the need for efficient semi-analytical tools that provide closed-form expressions for the postbuckled in-plane stiffness under general boundary conditions, particularly in multidisciplinary optimisation settings, such as wingbox design, where multiple panels may buckle and rapid repeated evaluations are required. The perturbation-based formulation of Seresta et al. (2008) pro-

vides a useful foundation for such semi-analytical modelling of straight-edge plates. As formulated in their work, the use of trigonometric shape functions limits the approach to simply supported boundary conditions, and the strain-energy terms are evaluated numerically, which further constrains the efficiency of the method for repeated postbuckling calculations. It is worth noting that symbolic integration has also been successfully implemented for a Ritz formulation using trigonometric functions in cylindrical coordinates, as demonstrated by Köllner (2021). In the present work, hierarchical polynomials are adopted as the Ritz basis, which allows the formulation to accommodate general boundary conditions. This choice also leads to closed-form analytical expressions for all required strain-energy integrals through recurrence relations, without relying on symbolic or numerical integration. The formulation also revisits and clarifies steps in the original method of Seresta et al. (2008) that were not fully detailed. Two solution methods are presented: a perturbation-based approach that yields the reduced stiffness matrix in terms of tensor evaluations, and an iterative correction scheme that extends the solution into the postbuckling regime. The methods are verified by comparison with results from the literature and finite element simulations. The resulting framework is computationally efficient and general in terms of boundary condition representation, and therefore suitable for integration into multidisciplinary design and optimisation environments where repeated evaluations of postbuckling response are required. The remainder of the chapter is structured as follows. Section 2.2 presents the problem formulation. Section 2.3 describes the tensor evaluation procedure. Section 2.4 outlines the two solution schemes. Section 2.5 presents the numerical results and validation, followed by conclusions in Section 2.6.

2.2. Problem Definition

The formulation is implemented for a laminate of dimensions $A \times B$, subject to edge displacements at $x = A$ and $y = B$. Figure 2.1 shows an example plate that is under prescribed edge displacements in the x and y directions.

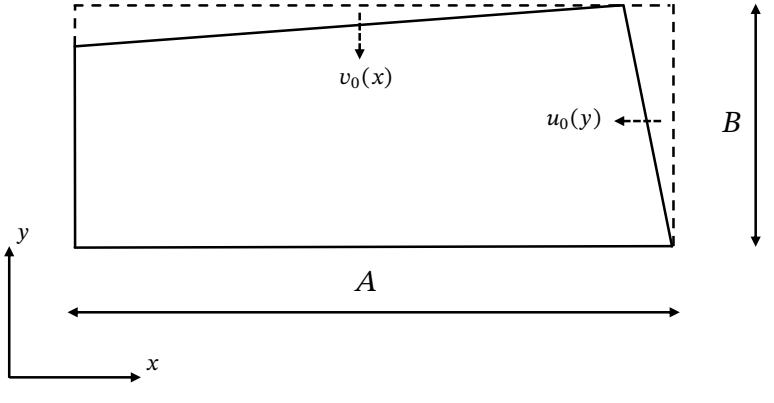

Figure 2.1: Composite laminate subject to edge displacements in the x and y directions.

Assuming a displacement field approximated by:

$$\begin{aligned} w(x,y) &= \sum_{i=2}^{N} a_i \phi_i^w \\ u(x,y) &= -\lambda e_{x0} x - \lambda \frac{g_{xy0}}{2} y + \sum_{i=2}^{N} b_i \phi_i^u \\ v(x,y) &= -\lambda e_{y0} y - \lambda \frac{g_{xy0}}{2} x + \sum_{i=2}^{N} c_i \phi_i^v, \end{aligned} \tag{2.1}$$

where $w(x,y)$ represents the out-of-plane displacement, and $u(x,y)$ and $v(x,y)$ are the in-plane displacements in the x- and y-directions, respectively. The coefficients a_i, b_i, and c_i are the Ritz parameters associated with the shape functions ϕ_i^w, ϕ_i^u, and ϕ_i^v, and N is the number of terms retained in the Ritz expansion. e_{x0}, e_{y0} and g_{xy0} represent strains that could be applied at the edges and λ is a scaling factor for these strains. In case of the absence of g_{xy0}, and if the shape functions are zero at the boundaries, the edge strain values are simply:

$$e_{x0} = u_0/A, \quad e_{y0} = v_0/B, \tag{2.2}$$

where u_0 and v_0 are the displacements applied at the edges $x = A$ and $y = B$ respectively.

Seresta et al. (2008) employed trigonometric shape functions, which limited their analysis to simply supported plates. In this work, incorporating hierarchical Legendre polynomials instead gives more flexibility in dealing with various boundary conditions. Another advantage is the ability to evaluate integrals involving hierarchical polynomials in a closed form without the need for numerical integration, as demonstrated in Appendix 2.B. The shape functions are defined as follows:

$$\begin{aligned} \phi_i^u &= L_m(\zeta) L_n(\eta) \\ \phi_i^v &= L_m(\zeta) L_n(\eta) \\ \phi_i^w &= H_m(\zeta) H_n(\eta), \end{aligned} \tag{2.3}$$

where $\zeta = 2x/A - 1$ and $\eta = 2y/B - 1$ are the natural coordinates on the reference domain, such that $\zeta, \eta \in [-1, 1]$. Also, L_i represents Lobatto Polynomials and H_i represents the integral of the Lobatto Polynomials, both expressed as follows (Szabó and Babuška, 2021):

$$\begin{aligned} L_{i+1}(\xi) &= \int_{-1}^{\xi} P_i(s) ds, \quad i \geq 1 \\ H_{i+1}(\xi) &= \int_{-1}^{\xi} L_i(s) ds, \quad i \geq 3, \end{aligned} \tag{2.4}$$

where s is a dummy variable, ξ may represent either ζ or η, and P_i represents Legendre Polynomials. Within this hierarchical basis, the lower-order polynomial

terms inherently control the boundary behaviour, enabling the direct representation of clamped, simply supported, or free edges, while the higher-order terms enrich the displacement field inside the domain. Figure 2.2 shows this behaviour for the first few polynomial orders. The explicit expressions for the lower-order polynomials are given in Section 2.3, Equation 2.21, where they are introduced for use in subsequent derivations.

For thin plates, strains are described in terms of mid-plane strains and curvatures by applying Kirchhoff plate theory assumptions (Seresta et al., 2008, Kassapoglou, 2013), as follows:

$$\epsilon_x = \epsilon_x^0 + z\kappa_x, \quad \epsilon_y = \epsilon_y^0 + z\kappa_y, \quad \gamma_{xy} = \gamma_{xy}^0 + z\kappa_{xy}. \tag{2.5}$$

To account for moderate large rotations, the mid-plane strains and curvatures can be computed as Seresta et al. (2008):

$$\begin{aligned} &\epsilon_x^0 = u_{,x} + \frac{1}{2}\left(w_{,x}\right)^2, \quad \epsilon_y^0 = v_{,y} + \frac{1}{2}\left(w_{,y}\right)^2, \quad \gamma_{xy}^0 = u_{,y} + v_{,x} + w_{,x}w_{,y}, \\ &\kappa_x = -w_{,xx}, \quad \kappa_y = -w_{,yy}, \quad \kappa_{xy} = -2w_{,xy}\,, \end{aligned} \tag{2.6}$$

where a comma followed by a subscript denotes partial differentiation, for example:

$$u_{,x} = \frac{\partial u}{\partial x}, \qquad v_{,y} = \frac{\partial v}{\partial y}, \qquad w_{,xy} = \frac{\partial^2 w}{\partial x\,\partial y}\,.$$

For symmetric balanced laminates, the total potential becomes (Seresta et al., 2008, Kassapoglou, 2013):

$$\begin{aligned} \Pi(u,v,w) = \frac{1}{2}\int_0^A \int_0^B \Big[&A_{11}\left(\epsilon_x^0\right)^2 + 2A_{12}\epsilon_x^0\epsilon_y^0 + A_{22}\left(\epsilon_y^0\right)^2 + A_{66}\left(\gamma_{xy}^0\right)^2 \\ &+ D_{11}\kappa_x^2 + 2D_{12}\kappa_x\kappa_y + 2D_{16}\kappa_x\kappa_{xy} + 2D_{26}\kappa_y\kappa_{xy} + D_{22}\kappa_y^2 + D_{66}\kappa_{xy}^2\Big]\, dydx. \end{aligned} \tag{2.7}$$

Substituting the mid-plane strains and curvatures expressions from Equation 2.6 into the total potential expression Equation 2.7:

$$\begin{aligned} \Pi(u,v,w) = \frac{1}{2}\int_0^A \int_0^B \Big[&A_{11}\Big(e_{x_0}^2 - 2e_{x_0}b_i\phi_{i,x}^u - e_{x_0}a_ia_j\phi_{i,x}^w\phi_{j,x}^w + b_ib_j\phi_{i,x}^u\phi_{j,x}^u \\ &+ a_ia_jb_k\phi_{i,x}^w\phi_{j,x}^w\phi_{k,x}^u + \frac{1}{4}a_ia_ja_ka_l\phi_{i,x}^w\phi_{j,x}^w\phi_{k,x}^w\phi_{l,x}^w\Big) + 2A_{12}\Big(e_{x_0}e_{y_0} - e_{x_0}c_i\phi_{i,y}^v \\ &- e_{y_0}b_i\phi_{i,x}^u - \frac{1}{2}e_{x_0}a_ia_j\phi_{i,y}^w\phi_{j,y}^w - \frac{1}{2}e_{y_0}a_ia_j\phi_{i,x}^w\phi_{j,x}^w + b_ic_j\phi_{i,x}^u\phi_{j,y}^v \\ &+ \frac{1}{2}a_ia_jb_k\phi_{i,y}^w\phi_{j,y}^w\phi_{k,x}^u + \frac{1}{2}a_ia_jc_k\phi_{i,x}^w\phi_{j,x}^w\phi_{k,y}^v + \frac{1}{4}a_ia_ja_ka_l\phi_{i,x}^w\phi_{j,x}^w\phi_{k,y}^w\phi_{l,y}^w\Big) \\ &+ A_{22}\Big(e_{y_0}^2 - 2e_{y_0}c_i\phi_{i,y}^v - e_{y_0}a_ia_j\phi_{i,y}^w\phi_{j,y}^w + c_ic_j\phi_{i,y}^v\phi_{j,y}^v + a_ia_jc_k\phi_{i,y}^w\phi_{j,y}^w\phi_{k,y}^v \\ &+ \frac{1}{4}a_ia_ja_ka_l\phi_{i,y}^w\phi_{j,y}^w\phi_{k,y}^w\phi_{l,y}^w\Big) \end{aligned}$$

$$
\begin{aligned}
&+ A_{66}\Big(g_{xy_0}^2 - 2g_{xy_0}b_i\phi_{i,y}^u - 2g_{xy_0}c_i\phi_{i,x}^v + b_ib_j\phi_{i,y}^u\phi_{j,y}^u + 2b_ic_j\phi_{i,y}^u\phi_{j,x}^v + c_ic_j\phi_{i,x}^v\phi_{j,x}^v \\
&- 2g_{xy_0}a_ia_j\phi_{i,x}^w\phi_{j,y}^w + 2a_ia_jb_k\phi_{i,x}^w\phi_{j,y}^w\phi_{k,y}^u + 2a_ia_jc_k\phi_{i,x}^w\phi_{j,y}^w\phi_{i,x}^v \\
&+ a_ia_ja_ka_l\phi_{i,x}^w\phi_{j,y}^w\phi_{k,x}^w\phi_{l,y}^w\Big) \\
&+ D_{11}\Big(a_ia_j\phi_{i,xx}^w\phi_{j,xx}^w\Big) + 2D_{12}\Big(a_ia_j\phi_{i,xx}^w\phi_{j,yy}^w\Big) + D_{22}\Big(a_ia_j\phi_{i,yy}^w\phi_{j,yy}^w\Big) \\
&+ D_{16}\Big(4a_ia_j\phi_{i,xx}^w\phi_{j,xy}^w\Big) + D_{26}\Big(4a_ia_j\phi_{i,yy}^w\phi_{j,xy}^w\Big) + D_{66}\Big(4a_ia_j\phi_{i,xy}^w\phi_{j,xy}^w\Big)\Big]\,dydx.
\end{aligned}
\tag{2.8}
$$

Minimising the total potential energy with respect to the Ritz coefficients b_i, c_i and a_i, respectively, results in the following equilibrium equations:

$$
\begin{aligned}
&- g_l^u + K_{il}^{ub}b_i + K_{il}^{uc}c_i + K_{ijl}^{uaa}a_ia_j = 0 \\
&- g_l^v + K_{il}^{vb}b_i + K_{il}^{vc}c_i + K_{ijl}^{vaa}a_ia_j = 0 \\
&K_{il}a_i - \lambda\bar{K}_{il}^g a_i + K_{ikl}^{wba}b_ia_k + K_{ikl}^{wca}c_ia_k + K_{ijkl}^{waaa}a_ia_ja_k = 0,
\end{aligned}
\tag{2.9}
$$

where:

$$
\begin{aligned}
g_l^u &= g_l^{ux}e_{x0} + g_l^{uy}e_{y0} + g_l^{uxy}g_{xy0} \\
g_l^v &= g_l^{vx}e_{x0} + g_l^{vy}e_{y0} + g_l^{vxy}g_{xy0} \\
\bar{K}_{il}^g &= \bar{K}_{il}^{gx}e_{x0} + \bar{K}_{il}^{gy}e_{y0} + \bar{K}_{il}^{gxy}g_{xy0}.
\end{aligned}
\tag{2.10}
$$

Definitions of the tensors introduced in Equations 2.9 and 2.10 are given in Appendix 2.A.

2.3. Hierarchical Polynomial Properties

Hierarchical polynomials exhibit interesting properties, making them an ideal choice for shape functions.

Legendre Polynomials

1. Mutually orthogonal

$$\int_{-1}^{1} P_m(\xi)P_n(\xi)d\xi = 0 \quad , m \neq n \tag{2.11}$$

2. Average over the domain equals zero as shown in Figure 2.2

$$\int_{-1}^{1} P_n(\xi)d\xi = 0 \quad , n \geq 1 \tag{2.12}$$

3. Recurrence Property

$$(n+1)P_{n+1}(\xi) = (2n+1)\xi P_n(\xi) - nP_{n-1}(\xi) \tag{2.13}$$

multiplying both sides by P_n and taking the integral over the domain, the following relation is obtained:

$$\int_{-1}^{1} P_n^2(\xi)d\xi = \frac{2}{2n+1} \quad , n \geq 1. \tag{2.14}$$

LOBATTO POLYNOMIALS

1. Value of the polynomials is zero at the boundaries (except for the first two polynomials)

$$L_n(-1) = L_n(1) = 0 \quad , n \geq 2 \tag{2.15}$$

2. Can be defined in terms of Legendre Polynomials using recurrence properties

$$(2n+1)P_n(\xi) = \frac{d}{d\xi}\left(P_{n+1}(\xi) - P_{n-1}(\xi)\right), \tag{2.16}$$

which is obtained by differentiating Equation 2.13. Then the relation between Legendre and Lobatto polynomials is obtained by integrating both sides with respect to ξ,

$$(2n+1)L_{n+1}(\xi) = P_{n+1}(\xi) - P_{n-1}(\xi) \tag{2.17}$$

or alternatively described as follows:

$$L_n(\xi) = \frac{1}{2n-1}\left(P_n(\xi) - P_{n-2}(\xi)\right) \quad , n \geq 2. \tag{2.18}$$

"H" POLYNOMIALS

1. Value of the polynomials is zero at the boundaries (except for the first two polynomials)

$$H_n(-1) = H_n(1) = 0 \quad , n \geq 2 \tag{2.19}$$

2. Can be defined in terms of Legendre Polynomials using recurrence properties

$$\begin{aligned} H_n(\xi) = \frac{1}{2n-3}\Bigg(&\frac{1}{2n-1}\left(P_n(\xi) - P_{n-2}(\xi)\right) \\ &-\frac{1}{2n-5}\left(P_{n-2}(\xi) - P_{n-4}(\xi)\right)\Bigg) \quad , n \geq 4. \end{aligned} \tag{2.20}$$

Note that the first polynomials can also be described in terms of Legendre polynomials as follows:

$$\begin{aligned} L_0 &= \frac{1}{2}P_0 + \frac{1}{2}P_1\,, & L_1 &= \frac{1}{2}P_0 - \frac{1}{2}P_1 \\ H_0 &= \frac{1}{2}P_0 - \frac{12}{20}P_1 + \frac{1}{10}P_3\,, & H_1 &= \frac{1}{2}P_0 + \frac{12}{20}P_1 - \frac{1}{10}P_3 \\ H_2 &= \frac{1}{6}P_0 - \frac{1}{10}P_1 - \frac{1}{6}P_2 + \frac{1}{10}P_3\,, & H_3 &= \frac{-1}{6}P_0 - \frac{1}{10}P_1 + \frac{1}{6}P_2 + \frac{1}{10}P_3. \end{aligned} \tag{2.21}$$

Given Equation 2.3 and applying the properties discussed in this section, closed-form solutions are derived for the integral terms of Equation 2.9. The details of the derivation are given in Appendix 2.B.

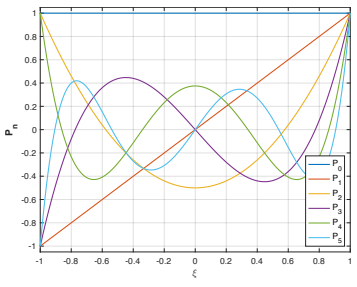

(a) Legendre Polynomials

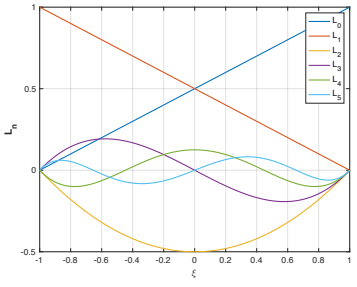

(b) Lobatto Polynomials

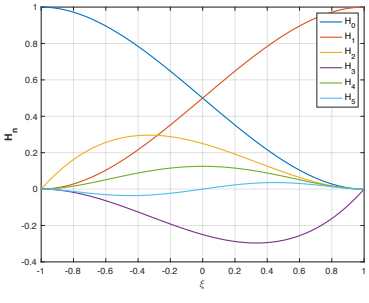

(c) "H" Polynomials

Figure 2.2: Hierarchical Polynomials.

2.4. Solution to Equilibrium Equations

A condensation approach will be followed to simplify the system of Equation 2.9. The first two equations of that system can be combined as follows:

$$-\left\{ \begin{array}{c} {g_l}^{ux} \\ {g_l}^{vx} \end{array} \right\} e_{x0} - \left\{ \begin{array}{c} {g_l}^{uy} \\ {g_l}^{vy} \end{array} \right\} e_{y0} - \left\{ \begin{array}{c} {g_l}^{uxy} \\ {g_l}^{vxy} \end{array} \right\} g_{xy0} + \left[\begin{array}{cc} k_{li}^{ub} & k_{li}^{uc} \\ k_{li}^{vb} & k_{li}^{vc} \end{array} \right] \left\{ \begin{array}{c} b_i \\ c_i \end{array} \right\} + \left\{ \begin{array}{c} {K_{lji}}^{uaa} \\ {K_{lji}}^{vaa} \end{array} \right\} a_i a_j = 0, \tag{2.22}$$

which can be described as follows:

$$-g_l^x e_{x0} - g_l^y e_{y0} - g_l^{xy} g_{xy0} + K_{lp}^a e_p + K_{lji}^{uvaa} a_i a_j = 0. \tag{2.23}$$

Solving for the Ritz coefficients b_i and c_i,

$$e_p = \left(K_{pl}^a\right)^{-1} \left[g_l^x e_{x_0} + g_l^y e_{y_0} + g_l^{xy} g_{xy_0} - K_{lji}^{uvaa} a_i a_j \right]. \tag{2.24}$$

The third equation of the system of Equation 2.9 can be rewritten as follows:

$$\begin{aligned} K_{li} a_i - \lambda \left(\bar{K}_{li}^{gx} e_{x_0} + \bar{K}_{li}^{gy} e_{y_0} + \bar{K}_{li}^{gxy} g_{xy_0} \right) a_i \\ + \left[K_{lkp}^{wba} K_{lkp}^{wca} \right] e_p a_k + K_{lkji}^{waaa} a_i a_j a_k = 0. \end{aligned} \tag{2.25}$$

Substituting the solution obtained in Equation 2.24 into Equation 2.25 leads to the following nonlinear equilibrium equation:

$$\left[K_{li} - \lambda K_{li}^{g}\right] a_i + K_{lkji}^{\mathrm{NL}} a_i a_j a_k = 0, \tag{2.26}$$

where:

$$K_{li}^{g} = K_{li}^{gx} e_{x_0} + K_{li}^{gy} e_{y_0} + K_{li}^{gxy} g_{xy_0} \tag{2.27}$$

and

$$\begin{aligned} K_{li}^{g_x} &= \bar{K}_{li}^{gx} - \left[K_{lip}^{wba} K_{lip}^{wca}\right] \left(K^{a}\right)_{ps}^{-1} g_s^{x} \\ K_{li}^{g_y} &= \bar{K}_{li}^{gy} - \left[K_{lip}^{wba} K_{lip}^{wca}\right] \left(K^{a}\right)_{ps}^{-1} g_s^{y} \\ K_{li}^{g_{xy}} &= \bar{K}_{li}^{gxy} - \left[K_{lip}^{wba} K_{lip}^{wca}\right] \left(K^{a}\right)_{ps}^{-1} g_s^{xy} \end{aligned} \tag{2.28}$$

and

$$K_{lkji}^{\mathrm{NL}} = K_{lkji}^{waaa} - \left[K_{lkp}^{wba} K_{lkp}^{wca}\right] \left(K^{a}\right)_{ps}^{-1} K_{sji}^{uvaa}. \tag{2.29}$$

Two approaches will be presented to solve the nonlinear equilibrium equation and assess the postbuckling behaviour. The first is based on the perturbation approach, while the second is an iterative scheme based on the Normal Flow Algorithm.

2.4.1. PERTURBATION APPROACH

The perturbation expansion approach follows the procedure of Seresta et al. (2008), with additional intermediate steps shown for clarification and a few equations not explicitly given in earlier work derived for completeness. The nonlinear equilibrium equation, which depends on uniform strains and Ritz coefficients, is therefore expanded into a perturbation series as follows:

$$\begin{aligned} e_{x0} &= e_{x_0}^{(0)} + \epsilon \cancelto{0}{e_{x_0}^{(1)}} + \epsilon^2 e_{x_0}^{(2)} + \cdots & e_{y0} &= e_{y_0}^{(0)} + \epsilon \cancelto{0}{e_{y_0}^{(1)}} + \epsilon^2 e_{y_0}^{(2)} + \cdots \\ g_{xy0} &= g_{xy_0}^{(0)} + \epsilon \cancelto{0}{g_{xy_0}^{(1)}} + \epsilon^2 g_{xy_0}^{(2)} + \cdots & a_i &= \cancelto{0}{a_i^{(0)}} + \epsilon a_i^{(1)} + \epsilon^2 a_i^{(2)} + \cdots . \end{aligned} \tag{2.30}$$

Here, the superscripts (0), (1), and higher orders correspond to prebuckling, buckling, and postbuckling states, respectively. Accordingly, the in-plane first-order terms vanish at buckling, and $a_i^{(0)} = 0$ for the imposed loading condition. Note that λ is dropped for the remainder of the perturbation derivation, since the perturbation expansion introduces its own scaling of the applied edge strains through ϵ, which cannot be merged with the single-parameter scaling represented by λ. The expansions defined in Equation 2.30 are then substituted back into Equation 2.26.

$$\begin{aligned} &\Big[K_{li} - \Big(K_{li}^{gx}\left(e_{x_0}^{(0)} + \epsilon^2 e_{x_0}^{(2)} + \ldots\right) + K_{li}^{gy}\left(e_{y_0}^{(0)} + \epsilon^2 e_{y_0}^{(2)} + \ldots\right) \\ &+ K_{li}^{gxy}\left(g_{xy_0}^{(0)} + \epsilon^2 g_{xy_0}^{(2)} + \ldots\right)\Big)\Big]\left(\epsilon a_i^{(1)} + \epsilon^2 a_i^{(2)} + \epsilon^3 a_i^{(3)} + \ldots\right) \\ &+ K_{lkji}^{\mathrm{NL}}\left(\epsilon a_i^{(1)} + \epsilon^2 a_i^{(2)} + \epsilon^3 a_i^{(3)} + \ldots\right)\left(\epsilon a_j^{(1)} + \epsilon^2 a_j^{(2)} + \epsilon^3 a_j^{(3)} + \ldots\right) \\ &\left(\epsilon a_k^{(1)} + \epsilon^2 a_k^{(2)} + \epsilon^3 a_k^{(3)} + \ldots\right) = 0. \end{aligned} \tag{2.31}$$

Equating coefficients of successive powers of ϵ yields the linear and nonlinear relations (cf. Seresta et al., 2008). The equation corresponding to the power of ϵ gives the linear buckling eigenvalue problem from which critical buckling loads and modes can be assessed:

$$\left[K_{li} - \left(K_{li}^{gx} e_{x_0}^{(0)} + K_{li}^{gy} e_{y_0}^{(0)} + K_{li}^{gxy} g_{xy_0}^{(0)}\right)\right] a_i^{(1)} = 0, \tag{2.32}$$

where ($e_{x_0}^{(0)}$, $e_{y_0}^{(0)}$ and $g_{xy_0}^{(0)}$) are the critical edge strains at buckling, and $a_i^{(1)}$ represents the eigenvectors corresponding to the critical applied edge strains. Equating the coefficient of ϵ^2 leads to the following equation:

$$\left[K_{li} - \left(K_{li}^{gx} e_{x_0}^{(2)} + K_{li}^{gy} e_{y_0}^{(2)} + K_{li}^{gxy} g_{xy_0}^{(2)}\right)\right] a_i^{(2)} = 0. \tag{2.33}$$

The coefficient of ϵ^3 gives another equation (Seresta et al., 2008):

$$\begin{aligned}&\left[K_{li} - \left(K_{li}^{gx} e_{x_0}^{(0)} + K_{li}^{gy} e_{y_0}^{(0)} + K_{li}^{gxy} g_{xy_0}^{(0)}\right)\right] a_i^{(3)} \\ &- \left(K_{li}^{gx} e_{x_0}^{(2)} + K_{li}^{gy} e_{y_0}^{(2)} + K_{li}^{gxy} g_{xy_0}^{(2)}\right) a_i^{(1)} + K_{lkji}^{\mathrm{NL}} a_i^{(1)} a_j^{(1)} a_k^{(1)} = 0,\end{aligned} \tag{2.34}$$

which is the first equation to exhibit nonlinear terms, but is singular. Multiplying Equation 2.34 by $a_l^{(1)}$ makes it solvable as the first term goes to zero from the linear buckling eigenvalue analysis, leading to the following form:

$$\left(K_{li}^{gx} e_{x_0}^{(2)} + K_{li}^{gy} e_{y_0}^{(2)} + K_{li}^{gxy} g_{xy_0}^{(2)}\right) a_i^{(1)} a_l^{(1)} = K_{lkji}^{\mathrm{NL}} a_i^{(1)} a_j^{(1)} a_k^{(1)} a_l^{(1)}. \tag{2.35}$$

Second-order perturbed edge strain parameters are obtained by varying each of them independently, while keeping the others equal to zero (Seresta et al., 2008):

$$e_{y0}^{(2)} = g_{xy0}^{(2)} = 0, \qquad e_{x0}^{(2)} = \frac{K_{lkji}^{NL} a_i^{(1)} a_j^{(1)} a_k^{(1)} a_l^{(1)}}{K_{li}^{gx} a_i^{(1)} a_l^{(1)}} \tag{2.36}$$

$$e_{x0}^{(2)} = g_{xy0}^{(2)} = 0, \qquad e_{y0}^{(2)} = \frac{K_{ijkl}^{NL} a_i^{(1)} a_j^{(1)} a_k^{(1)} a_l^{(1)}}{K_{li}^{gy} a_i^{(1)} a_l^{(1)}} \tag{2.37}$$

$$e_{x0}^{(2)} = e_{y0}^{(2)} = 0, \qquad g_{xy0}^{(2)} = \frac{K_{lkji}^{NL} a_i^{(1)} a_j^{(1)} a_k^{(1)} a_l^{(1)}}{K_{li}^{gxy} a_i^{(1)} a_l^{(1)}}. \tag{2.38}$$

An approximation of the postbuckled stiffness can be obtained by relating the second-order perturbed stress resultants to the corresponding second-order edge strains. In Seresta et al. (2008), the second-order perturbed stress resultants were introduced, but no explicit expressions were provided. For clarity, these expressions are derived here, starting from the in-plane stress resultants in terms of the mid-plane strains (Kassapoglou, 2013):

$$N_x = A_{11}\epsilon_x^0 + A_{12}\epsilon_y^0. \tag{2.39}$$

Using Equations 2.6 and 2.30 and expanding till the first power of ϵ, then extracting the coefficient of ϵ^2:

$$N_x^{(2)} = \frac{1}{2}\left(A_{11} a_i^{(1)} a_j^{(1)} \phi_{i,x}^w \phi_{j,x}^w + A_{12} a_i^{(1)} a_j^{(1)} \phi_{i,y}^w \phi_{j,y}^w\right). \tag{2.40}$$

The average resultant in the x direction is then obtained as:

$$\bar{N}_x^{(2)} = \frac{1}{AB}\int_0^A \int_0^B N_x^{(2)}(x,y)\, dydx, \tag{2.41}$$

$\bar{N}_y^{(2)}$ and $\bar{N}_{xy}^{(2)}$ are evaluated analogously. The postbuckled stiffnesses are then evaluated as follows:

$$A_{11}^{\mathrm{PB}} = \frac{\bar{N}_x^{(2)}}{e_{x0}^{(2)}},\ A_{12}^{\mathrm{PB}} = \frac{\bar{N}_x^{(2)}}{e_{y0}^{(2)}},\ A_{21}^{\mathrm{PB}} = \frac{\bar{N}_y^{(2)}}{e_{x0}^{(2)}},\ A_{22}^{\mathrm{PB}} = \frac{\bar{N}_y^{(2)}}{e_{y0}^{(2)}},\ A_{66}^{\mathrm{PB}} = \frac{\bar{N}_{xy}^{(2)}}{g_{xy0}^{(2)}}. \tag{2.42}$$

2.4.2. Iterative Scheme (Normal Flow Algorithm)

The Normal Flow Algorithm (NFA) has proven efficient and robust for tracing nonlinear equilibrium paths compared to conventional techniques (Ragon et al., 2002). In this work, it is employed as a corrector step within a prediction–correction iterative framework. The algorithm starts from the linear buckling solution and proceeds through successive prediction–correction steps, where convergence is enforced along a direction normal to the Davidenko flow (Ragon et al., 2002, Allgower and Georg, 1990).

The full derivation of the iterative scheme, including the governing equations and implementation details, is provided in Appendix 2.D. The focus here is on its application to the present postbuckling problem and its verification through representative numerical cases.

2.5. Results

A composite panel of dimensions (A = 254 mm (10 in) and B = 254 mm (10 in)) is considered, with the ply properties listed in Table 2.1. Multiple laminates with different ply orientations are evaluated. SI units are used throughout the chapter; the corresponding imperial values are provided in parentheses where space permits; otherwise, they are reported in Appendix 2.E for consistency with benchmark cases in the literature. For clarity, the conversion factors used in this section are stated explicitly: 1 in = 25.4 mm, 1 lbf/in = 0.0001751 kN/mm, and 10^6 psi = 6.89476 GPa (equivalently, 6.89476 kN/mm^2).

Table 2.1: Elastic properties of a unidirectional composite ply (Seresta et al., 2008). Imperial equivalents: 1 GPa = 145.04×10^3 psi, 1 mm = 0.03937 in.

E_{11} [GPa]	E_{22} [GPa]	G_{12} [GPa]	ν	t_{ply} [mm]
127.60	11.03	5.74	0.35	0.127

2.5.1. Linear Buckling Analysis

The linear buckling analysis is done by solving the eigenvalue problem:

$$\left[K_{li} - \lambda \left(K_{li}^{gx} e_{x_0}^{(0)} + K_{li}^{gy} e_{y_0}^{(0)} + K_{li}^{gxy} g_{xy_0}^{(0)}\right)\right] a_i^{(1)} = 0, \tag{2.43}$$

which can be rewritten in an alternative form in terms of the average resultants as follows:

$$\begin{aligned}\Big[K_{li} - \lambda \Big(&\left(a_{11}K_{li}^{gx} + a_{21}K_{li}^{gy}\right) N_{xx}^{(0)} + \left(a_{12}K_{li}^{gx} + a_{22}K_{li}^{gy}\right) N_{yy}^{(0)} \\ &+ a_{66}K_{li}^{gxy} N_{xy}^{(0)}\Big)\Big] a_i^{(1)} = 0,\end{aligned} \tag{2.44}$$

where $a_{11}, a_{12}, a_{21}, a_{22}$, and a_{66} are the elements of the inverse of the A matrix.

The results are compared to the analytical formula of the critical buckling load under biaxial loading (Kassapoglou, 2013), given in Equation 2.45, and a direct comparison is listed in Table 2.2:

$$N_0 = \frac{\pi^2 \left[D_{11}m^4 + 2\left(D_{12} + 2D_{66}\right) m^2 n^2 (AR)^2 + D_{22} n^4 (AR)^4\right]}{A^2 \left(m^2 + kn^2 (AR)^2\right)}, \tag{2.45}$$

where: $N_{x_{cr}} = -N_0 = -\lambda_{cr} N_{xx}^{(0)}$, m and n are the number of half waves in the x and y directions respectively, $AR = A/B$, and $k = N_{yy}^{(0)}/N_{xx}^{(0)}$. A convergence

Table 2.2: Critical buckling loads predicted by the proposed methodology, using 12 Ritz terms, compared with analytical values.

No.	Stacking Seq.	$N_{xx}^{(0)}/N_{yy}^{(0)}$	$\lambda_{cr} N_{xx}^{(0)}$ [kN/mm]	N_0 [kN/mm]
1	$[(0\ 90)_4]_s$	1/0	182.686×10^{-4}	182.680×10^{-4}
2	$[(0\ 90)_4]_s$	1/1	91.343×10^{-4}	91.340×10^{-4}
3	$[(45\ 90 - 45\ 90)_2]_s$	1/0	252.103×10^{-4}	252.095×10^{-4}
4	$[(45 - 45)_4]_s$	1/1	149.798×10^{-4}	149.795×10^{-4}

analysis is then performed to assess the number of sufficient terms that will be used. The error is defined relative to the analytical buckling load N_0 as:

$$\text{Error} = \frac{N_{\text{cr,approx}} - N_0}{N_0} \times 100, \tag{2.46}$$

where $N_{\text{cr,approx}}$ is the approximate buckling load obtained from the Ritz expansion, and N_0 is the analytical solution defined in Equation 2.45. As shown in Figure 2.3, using 12 terms always leads to an error less than 1%. In some laminates, using even 9 terms is sufficient to obtain an error less than 1%. Using 16 terms even leads to an error less than 0.5%.

2.5.2. Non-Linear Postbuckling Analysis

A model is created in Abaqus (Dassault Systèmes, 2022) for verification of the presented methodology. First, an Abaqus *Linear Perturbation, Buckle* analysis is performed to obtain the buckling eigenvalues and eigenmodes. Then a Static-Riks analysis is performed to assess the postbuckling response.

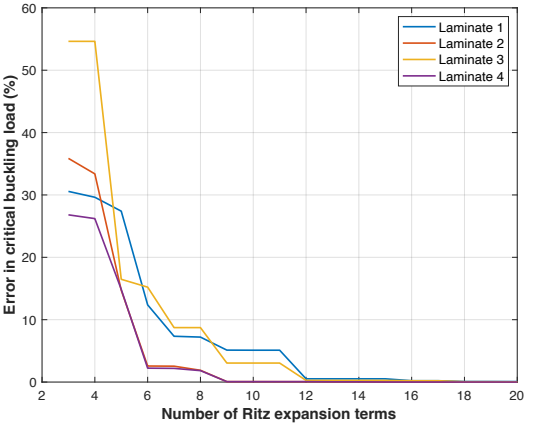

Figure 2.3: Convergence of the Ritz expansion for the linear buckling analysis: error in critical buckling load (%) versus number of terms for different laminate configurations.

PERTURBATION APPROACH

The average resultant forces will be calculated at the edges, $x = A$ and $y = B$, as follows:

$$\begin{aligned} \bar{N}_x &= \frac{1}{B}\int_0^B N_x(A,y)dy = \frac{1}{B}\int_0^B \left[A_{11}^{\mathrm{PB}}\epsilon_x^0(A,y) + A_{12}^{\mathrm{PB}}\epsilon_y^0(A,y)\right] dy \\ \bar{N}_y &= \frac{1}{A}\int_0^A N_y(x,B)dx = \frac{1}{A}\int_0^A \left[A_{21}^{\mathrm{PB}}\epsilon_x^0(x,B) + A_{22}^{\mathrm{PB}}\epsilon_y^0(x,B)\right] dx. \end{aligned} \tag{2.47}$$

A convergence analysis is then performed to determine the number of Ritz terms required for a sufficiently accurate nonlinear postbuckling response. For this purpose, the following relative difference is defined with respect to a highly converged reference value:

$$\text{Relative Change} = \frac{\bar{N}_x(N) - \bar{N}_x(N_{\max})}{\bar{N}_x(N_{\max})} \times 100, \tag{2.48}$$

where $\bar{N}_x(N)$ is the average resultant force at the loaded edge obtained using N Ritz terms, and $\bar{N}_x(N_{\max})$ is the corresponding value computed using a sufficiently large number of terms ($N_{\max} = 25$), which is taken as the converged reference.

It is noted that this highly converged value refers only to the solution within the present Ritz formulation and does not imply that the resulting postbuckling response is fully accurate, but rather represents the best approximation attainable with the proposed method. The comparison is carried out at the edge-displacement levels specified in Table 2.3. The results are compared with results from the literature and the created Abaqus model. For consistency, the table is presented in SI units, and an equivalent version in imperial units is included in Appendix 2.E for direct comparison with the literature (Seresta et al., 2008). Note in Table 2.3 that u_0/v_0

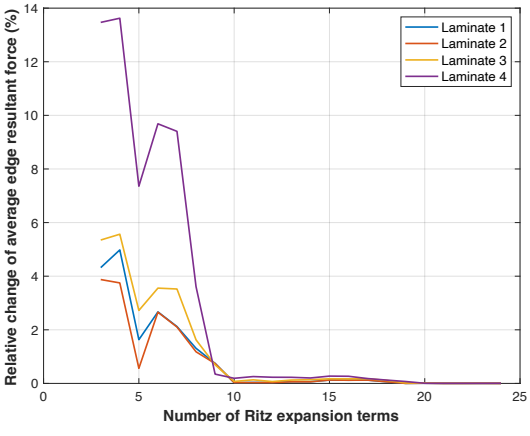

Figure 2.4: Convergence of the Ritz expansion for the nonlinear postbuckling analysis: relative change in the average resultant force at the loaded edge (%) versus the number of expansion terms for the different laminate configurations.

relates to the applied edge strains, λ_{cr} represents the critical multiplier for the applied edge displacement, and λ_f represents the full strain multiplier at which the average resultant forces are evaluated. As shown in Figure 2.4, all laminates show consistent convergence behaviour. For all layups considered, using approximately 8–10 terms reduces the relative change below 1%, and using 17 terms or more drives the difference to below 0.2%.

Table 2.3: Comparison of different approaches for multiple laminate layups.

Stacking Seq.	(u_0/v_0) $\times 10^{-3}$	λ_f	Literature (Seresta et al., 2008)		Abaqus simulation			Present approach			Present/Abaqus		
			$\bar{N}_x$	$\bar{N}_y$	λ_{cr}	$\bar{N}_x$	$\bar{N}_y$	λ_{cr}	$\bar{N}_x$	$\bar{N}_y$	$R_{\lambda_{cr}}$	$R_{\bar{N}_x}$	$R_{\bar{N}_y}$
$[(0\ 90)_4]_s$	1/0	354.58	0.1344	-0.0532	31.24	0.1177	-0.0605	30.99	0.1386	-0.0693	0.99	1.18	1.15
$[(0\ 90)_4]_s$	1/1	210.57	0.0471	0.0471	15.37	0.0413	0.0402	15.44	0.0411	0.0411	1.005	0.996	1.02
$[(0\ 90)_4]_s$	1.5/1	178.31	0.0731	0.0259	12.32	0.0650	0.0192	12.34	0.0697	0.0174	1.002	1.07	0.91
$[(0\ 90)_4]_s$	2/1	155.70	0.0928	0.0104	10.26	0.0820	0.0038	10.29	0.0913	1.4×10^{-6}	1.002	1.11	0.0003
$[(45\ 90\ -45\ 90)_2]_s$	1/0	506.22	0.0765	-0.0056	68.07	0.0631	0.0103	69.60	0.0993	-0.0635	1.02	1.58	-6.15
$[(45\ -45)_4]_s$	1/1	307.85	0.0509	0.0509	24.23	0.0331	0.0331	25.04	0.0525	0.0525	1.03	1.59	1.59

Units:
$\bar{N}_x, \bar{N}_y$: kN/mm
u_0, v_0: mm
λ_{cr}, λ_f: dimensionless load parameters (scaled by the reference displacement definition)
Ratios are dimensionless and defined as: R = Present Approach/Abaqus.

The results reported in Table 2.3 generally follow the same trends observed in Seresta et al. (2008), although the level of agreement varies across the different loading cases and laminate configurations. The first loading condition ($u_0/v_0 = 1/0$) showed the largest deviation from Abaqus results for the cross-ply laminates, whereas the cases with $u_0/v_0 = 1/1$, 1.5/1, and 2/1 exhibited noticeably smaller differences. The two angle-ply laminates also show larger deviations, a behaviour

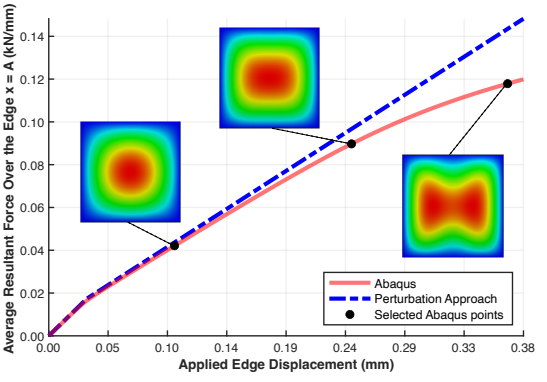

(a) $[(0/90)_4]_s$ laminate under uniaxial edge displacement $u_0/v_0 = 1/0$.

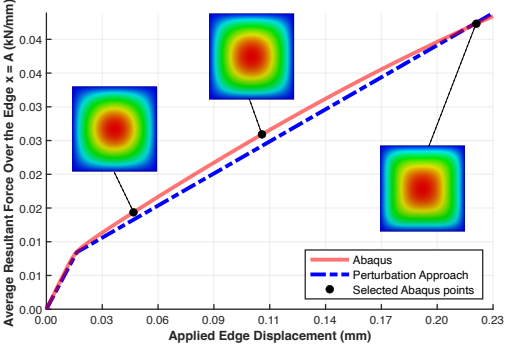

(b) $[(0/90)_4]_s$ laminate under biaxial edge displacement $u_0/v_0 = 1/1$.

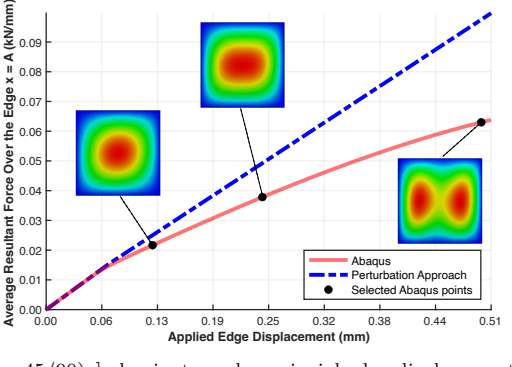

(c) $[(45/90/-45/90)_2]_s$ laminate under uniaxial edge displacement $u_0/v_0 = 1/0$.

Figure 2.5: Comparison between perturbation method and Abaqus for the relationship between applied edge displacement and average edge force for three laminate configurations, with selected Abaqus out-of-plane displacement fields shown at representative displacement levels.

consistent with previously reported challenges in predicting postbuckling response for such layups using reduced-order or perturbation-type formulations. The deviations in $\bar{N}_y$ are generally larger, particularly in the cases where u_0 is significantly larger than v_0, which is consistent with the behaviour reported by Seresta et al. (2008). In many practical aerospace applications, such as panels within wingbox structures, the main loading direction of interest is along the spanwise direction, where compressive buckling typically initiates. Nevertheless, the reduced accuracy observed in $\bar{N}_y$ under such loading cases reflects a limitation of the present methodology. Similar deviations have been noted in semi-analytical postbuckling formulations (Zhang, 2018, Zhao, 2021), where the restricted in-plane kinematics of the assumed displacement field neither provide the enriched in-plane representation required to capture the relevant in-plane deformation patterns (Zhang, 2018, Zhao, 2021) nor adequately represent in-plane compatibility (Zhang, 2018, Rehfield et al., 1992). In the present study, the observed deviations in $\bar{N}_y$ for these load cases can be attributed to modal interaction, as illustrated in Figure 2.5. Since the perturbation is performed using the first buckling mode, the validity of the perturbation method when modal interaction occurs is knowingly limited (Liang et al., 2014, Hutchinson and Koiter, 1970, Liang et al., 2013).

The differences observed between the current methodology and the literature (Seresta et al., 2008) are explained by the fact that the two formulations rely on different displacement bases and truncation levels, which naturally lead to variations when the edge resultants are compared point-wise. Several studies have noted that angle-ply laminates display a more nonlinear postbuckling response, greater stiffness degradation, and a stronger sensitivity to initial imperfections than cross-ply configurations (Ovesy and Assaee, 2007, Shen and Williams, 1997, Shen, 2000, Zou and Qiao, 2002). Consequently, the more complex nonlinear response of angle-ply laminates places additional demands on classical perturbation-based formulations, whose validity is inherently restricted to a neighbourhood of the bifurcation point (Liang et al., 2014, Hutchinson and Koiter, 1970). In contrast, geometrically nonlinear finite elements do not rely on such asymptotic assumptions and capture these effects more readily. A further contributor to these deviations can be the treatment of transverse shear deformation. The present formulation is based on classical laminate plate theory, which is shear-rigid, whereas Abaqus' shell model incorporates transverse shear flexibility. Although the plates analysed here are thin and shear effects are not expected to play a major role, Reddy and Liu (1987) noted that even for thin plates, transverse shear deformation may still influence nonlinear response, and Matsunaga (2001) reported that neglecting shear can lead to a slight over-prediction of stiffness.

The edge-displacement versus edge-resultant curves in Figure 2.5 reinforce the previous observations and provide a clearer picture of how the deviation evolves along the postbuckling path. For the cross-ply laminate under $u_0/v_0 = 1/0$, shown in Figure 2.5a, the present method matches Abaqus response closely near buckling but progressively diverges at larger edge displacements. The biaxial case $u_0/v_0 = 1/1$, shown in Figure 2.5b, maintains a very good estimate throughout the range. The angle-ply laminate in Figure 2.5c shows noticeably larger deviations over the entire

range, consistent with the increased nonlinearity typically observed in such layups. This behaviour also explains the larger discrepancies observed at some evaluation points in Table 2.3, particularly deeper in the postbuckling range, although these displacement levels were selected to match the comparison points reported by Seresta et al. (2008).

2.5.3. NORMAL FLOW ALGORITHM

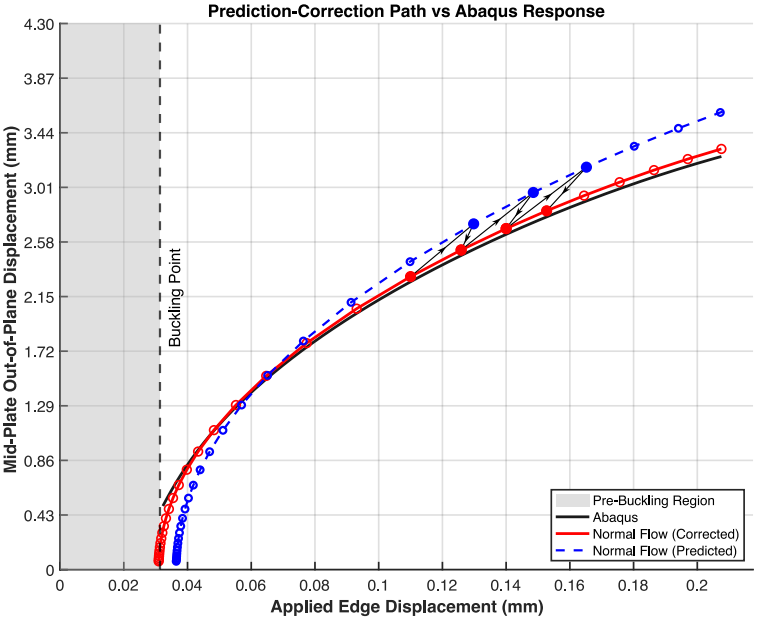

Figure 2.6: Prediction and corrected nonlinear paths for a $[(0/90)_4]_s$ laminate under uniaxial loading ($u_0/v_0 = 1/0$).

To assess the accuracy of the NFA, the results were compared against Abaqus for various laminate configurations under different loading conditions. Figure 2.6 illustrates the prediction–correction scheme in detail, showing mid-plate displacement (postbuckling deformation) against the applied edge displacement. Hollow markers indicate all sampled predicted and converged points along the postbuckling path, while selected steps are highlighted using filled markers to clarify the progression of the prediction–correction process. The postbuckling response and corresponding displacement fields are shown in Figures 2.7–2.10 for representative laminate layups and loading conditions. Each figure pairs the mid-plate response curve with the out-of-plane displacement fields from both NFA and Abaqus at the evaluation point indicated on the curve. For Figures 2.8–2.10, the field evaluation point is chosen shortly before the deviation from Abaqus becomes apparent, so that the displacement fields compare NFA against Abaqus while agreement is still close. For Figure 2.7, the evaluation point is instead chosen near the full applied edge

displacement, specifically to illustrate the displacement field at the level where the deviation is most pronounced.

Overall, the NFA response shows close agreement with Abaqus, particularly in the early and intermediate postbuckling range. Deviations become noticeable only at larger applied displacements for the uniaxial cross-ply case $u_0/v_0 = 1/0$, as shown in Figure 2.7. These deviations increase further for the angle-ply laminate under the same loading, shown in Figure 2.9, consistent with the stronger nonlinearities typically exhibited by such layups. Despite these variations at deep postbuckling levels, the NFA accurately captures both the postbuckling response and the associated displacement fields across the examined configurations.

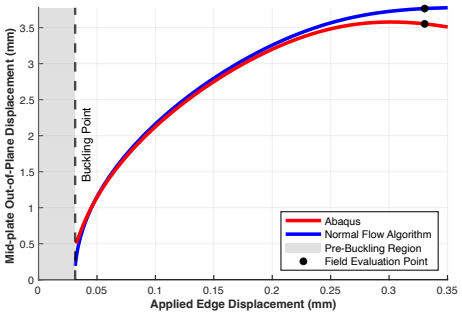

(a) Mid-plate out-of-plane displacement response under applied edge displacement.

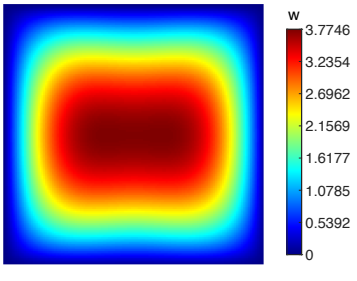

(b) Out-of-plane displacement field from the NFA.

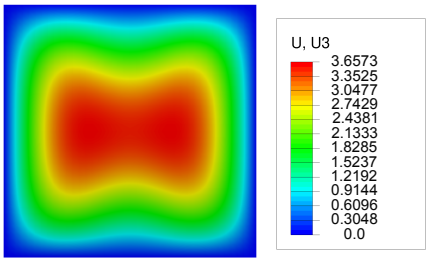

(c) Out-of-plane displacement field from Abaqus.

Figure 2.7: Postbuckling response and displacement fields: Laminate $[(0/90)_4]_s$, $u_0/v_0 = 1/0$.

2.5.4. Computational Time Comparison

The computational efficiency of the proposed approaches is assessed by comparing wall-clock times on an Intel Xeon W-2223 CPU @ 3.60 GHz with 16 GB RAM. All simulations were performed using the same panel, $[(0/90)_4]_s$, under uniaxial loading. The FEM analysis consisted of a linear buckling step followed by a nonlinear Static-Riks analysis incorporating initial imperfections.

The perturbation method involves nested for-loops used for defining Ritz polynomials, constructing tensor expressions, and evaluating integrals based on the recursive relations in Appendix 2.B. To improve computational performance, the functions used for integral evaluations were precompiled using MEX in MATLAB. Both

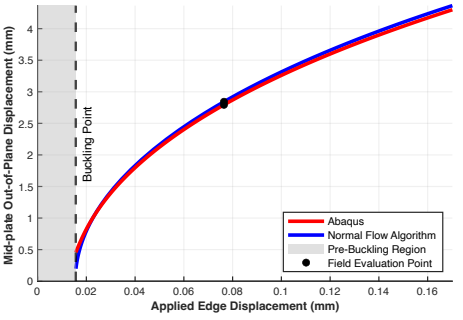

(a) Mid-plate out-of-plane displacement response under applied edge displacement.

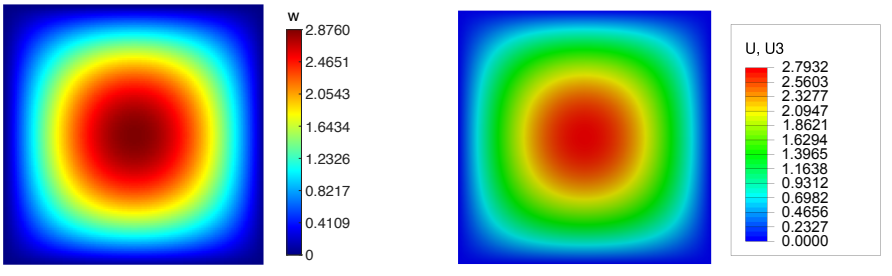

(b) Out-of-plane displacement field from the NFA. (c) Out-of-plane displacement field from Abaqus.

Figure 2.8: Postbuckling response and displacement fields: Laminate $[(0/90)_4]_s$, $u_0/v_0 = 1/1$.

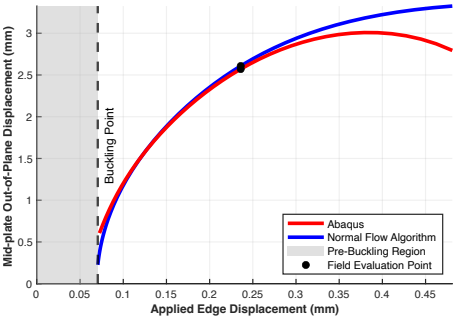

(a) Mid-plate out-of-plane displacement response under applied edge displacement.

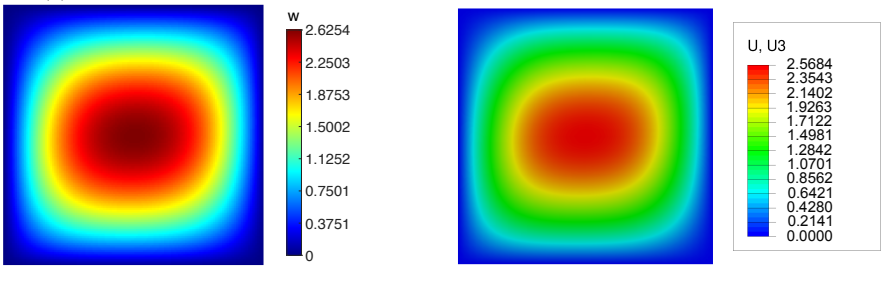

(b) Out-of-plane displacement field from the NFA. (c) Out-of-plane displacement field from Abaqus.

Figure 2.9: Postbuckling response and displacement fields: $[(45/90/-45/90)_2]_s$, $u_0/v_0 = 1/0$.

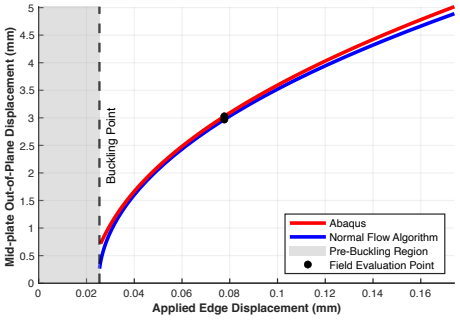

(a) Mid-plate out-of-plane displacement response under applied edge displacement.

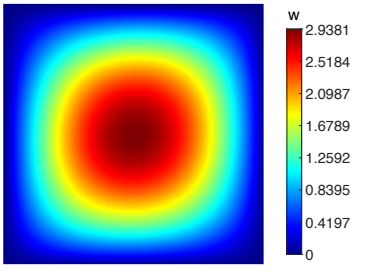

(b) Out-of-plane displacement field from the NFA.

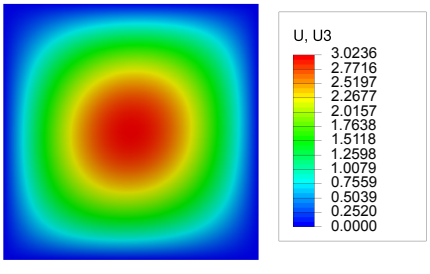

(c) Out-of-plane displacement field from Abaqus.

Figure 2.10: Postbuckling response and displacement fields: Laminate $[(45/-45)_4]_s$, $u_0/v_0 = 1/1$.

the original MATLAB implementation and the optimised version are included for comparison. The iterative method, which solves for the full nonlinear postbuckling response via the NFA, is also implemented entirely in MATLAB.

The results, summarised in Table 2.4, show a significant reduction in computational time compared to the FEM solution in Abaqus, while accurately capturing the postbuckling response. The MEX optimisation clearly reduces the evaluation time of the integral evaluation functions, primarily due to the for loops involved.

Table 2.4: Comparison of computational time: commercial FEM (Abaqus) vs. proposed methods (MATLAB implementation).

Method	**Timing step included**	**Wall-clock time (s)**
Abaqus - Linear buckling	Full linear buckling run	4.00
Abaqus - Nonlinear postbuckling (Static-Riks)	Full Riks run with imperfections	70.00
Perturbation method (MATLAB implementation)	Computation of $\mathbf{A}_{\mathrm{PB}}$	1000.00
Perturbation method (with MEX optimisation)	Computation of $\mathbf{A}_{\mathrm{PB}}$	6.97
Iterative method (with MEX optimisation)	Full iterative solution of postbuckling path	8.40

2.6. Conclusion

We presented a semi-analytical postbuckling method combining the Rayleigh-Ritz approach with hierarchical polynomials, enabling closed-form integration and efficient representation of displacement fields. Two solution strategies were employed

to solve the nonlinear equilibrium equations: a perturbation-based method that provides a fast approximation near the buckling point, and an iterative correction scheme based on the NFA that traces the response deeper into the postbuckling regime. The latter was shown to track the nonlinear response well beyond the buckling point, while maintaining close agreement with Abaqus across different laminate configurations and loading conditions. The perturbation-based solution captured the axial response in the main loading direction with good accuracy, particularly in the vicinity of the buckling load. Larger deviations were observed in the transverse response and in the angle-ply laminates under highly asymmetric loading, reflecting both the increased nonlinearity of these cases and the limitations of the current formulation. For the intended application to wingbox-type panels, where design is primarily governed by the axial postbuckling stiffness, the level of agreement remains adequate. The computational times reported in Table 2.4 confirm that the proposed methods achieve a substantial reduction in runtime relative to commercial finite element simulations in Abaqus, while maintaining accuracy. This efficiency makes the framework particularly suitable for structural design and multidisciplinary optimisation studies that require repeated evaluation of postbuckling response.

Bibliography

E. L. Allgower and K. Georg. *Numerical Continuation Methods*. Springer Berlin Heidelberg, 1990. ISBN 9783642612572. doi: 10.1007/978-3-642-61257-2.

M. S. Anderson. Design of panels having postbuckling strength. In *Collection of Technical Papers - AIAA/ASME/ASCE/AHS/ASC Structures, Structural Dynamics and Materials Conference*, volume 3, pages 2407–2413. AIAA, 1997. doi: 10.2514/6.1997-1240.

R. Ansari, R. Hassani, R. Gholami, and H. Rouhi. Thermal postbuckling analysis of fg-cntrc plates with various shapes and temperature-dependent properties using the vdq-fem technique. *Aerospace Science and Technology*, 106:106078, Nov. 2020. ISSN 1270-9638. doi: 10.1016/j.ast.2020.106078.

J. Arbocz and J. M. A. M. Hol. Koiter's stability theory in a computeraided engineering (cae) environment. *International Journal of Solids and Structures*, 26(9):945–973, 1990. ISSN 0020-7683. doi: https://doi.org/10.1016/0020-7683(90)90011-J.

J. Becque. An analytical description of the post-buckling behaviour of outstand plates in compression. *International Journal of Solids and Structures*, 254-255:111925, 2022. ISSN 0020-7683. doi: https://doi.org/10.1016/j.ijsolstr.2022.111925.

C. Bisagni and R. Vescovini. Analytical formulation for local buckling and post-buckling analysis of stiffened laminated panels. *Thin-Walled Structures*, 47(3): 318–334, 2009. ISSN 0263-8231. doi: https://doi.org/10.1016/j.tws.2008.07.006.

S. G. P. Castro and E. L. Jansen. Displacement-based formulation of koiter's method: Application to multi-modal post-buckling finite element analysis of plates. *Thin-Walled Structures*, 159:107217, 2021. ISSN 0263-8231. doi: https://doi.org/10.1016/j.tws.2020.107217.

C. Collier, P. Yarrington, and B. Van West. Composite, grid-stiffened panel design for post buckling using Hypersizer®. In *Collection of Technical Papers - AIAA/ASME/ASCE/AHS/ASC Structures, Structural Dynamics and Materials Conference*, volume 1, pages 157–172, 2002. doi: 10.2514/6.2002-1222.

C. Collier, P. Yarrington, P. Gustafson, and B. Bednarcyk. Local post buckling: An efficient analysis approach for industry use. In *50th AIAA/ASME/ASCE/AHS/ASC Structures, Structural Dynamics, and Materials Conference*. American Institute of Aeronautics and Astronautics, May 2009. doi: 10.2514/6.2009-2507.

Dassault Systèmes. *ABAQUS 2022 Documentation*. Dassault Systèmes Simulia Corp., Providence, RI, USA, 2022.

C. G. Diaconu and P. M. Weaver. Approximate solution and optimum design of compression-loaded, postbuckled laminated composite plates. *AIAA Journal*, 43 (4):906–914, 2005. doi: 10.2514/1.10827.

C. G. Diaconu and P. M. Weaver. Postbuckling of long unsymmetrically laminated composite plates under axial compression. *International Journal of Solids and Structures*, 43(22):6978–6997, 2006. ISSN 0020-7683. doi: https://doi.org/10.1016/j.ijsolstr.2006.02.017.

S. D. Dillen and C. Mittelstedt. Efficient post-buckling analysis of laminated plates with bending–twisting coupling using a novel algorithmic implementation. *Composite Structures*, 373:119646, Dec. 2025. ISSN 0263-8223. doi: 10.1016/j.compstruct.2025.119646.

J. A. Gaunt. The triplets of helium. *Philosophical Transactions of the Royal Society of London. Series A, Containing Papers of a Mathematical or Physical Character*, 228(659-669):151–196, 1929. doi: 10.1098/rsta.1929.0004.

A. Grisham. A method for including post-buckling of plate elements in the internal loads analysis of any complex structure idealized using finite element analysis methods. In *19th Structures, Structural Dynamics and Materials Conference*. American Institute of Aeronautics and Astronautics, Apr. 1978. doi: 10.2514/6.1978-515.

S. Hui-shen. Buckling and postbuckling behavior of antisymmetrically angle-ply laminated composite plates. *Applied Mathematics and Mechanics*, 11(12):1155–1165, Dec. 1990. ISSN 1573-2754. doi: 10.1007/bf02016618.

J. Hutchinson and W. Koiter. Postbuckling theory. *Appl. Mech. Rev*, 23(12):1353–1366, 1970.

C. Kassapoglou. *Design and Analysis of Composite Structures: With Applications to Aerospace Structures*. Wiley, May 2013. ISBN 9781118536933. doi: 10.1002/9781118536933.

W. T. Koiter. *On the stability of elastic equilibrium*. National Aeronautics and Space Administration, 1967.

A. Köllner. Predicting buckling-driven delamination propagation in composite laminates: An analytical modelling approach. *Composite Structures*, 266:113776, 2021. ISSN 0263-8223. doi: https://doi.org/10.1016/j.compstruct.2021.113776.

A. Köllner and N. Lüer. A path-following approach for quasi-static structural and material instability phenomena. *Computer Methods in Applied Mechanics and Engineering*, 436:117704, 2025. ISSN 0045-7825. doi: https://doi.org/10.1016/j.cma.2024.117704.

L. Lanzi and V. Giavotto. Post-buckling optimization of composite stiffened panels: Computations and experiments. *Composite Structures*, 73(2):208–220, May 2006. ISSN 0263-8223. doi: 10.1016/j.compstruct.2005.11.047.

K. Liang, M. Abdalla, and Z. Gürdal. A Koiter-Newton approach for nonlinear structural analysis. *International Journal for Numerical Methods in Engineering*, 96(12):763–786, 12 2013. ISSN 00295981. doi: 10.1002/nme.4581.

K. Liang, M. Ruess, and M. Abdalla. The koiter–newton approach using von kármán kinematics for buckling analyses of imperfection sensitive structures. *Computer Methods in Applied Mechanics and Engineering*, 279:440–468, 2014. ISSN 0045-7825. doi: https://doi.org/10.1016/j.cma.2014.07.008.

Y. Liu, J. Wang, D. Du, and G. Nie. A variational differential quadrature formulation for buckling analysis of anisogrid composite lattice conical shells. *Applied Mathematics and Mechanics*, 46(11):2155–2176, Oct. 2025. ISSN 1573-2754. doi: 10.1007/s10483-025-3310-9.

Y. Lv, J. Zhang, and L. Li. Thermal buckling and postbuckling of functionally graded multilayer gpl-reinforced composite beams on nonlinear elastic foundations. *Heliyon*, 9(9):e19549, Sept. 2023. ISSN 2405-8440. doi: 10.1016/j.heliyon.2023.e19549.

H. Matsunaga. Vibration and stability of angle-ply laminated composite plates subjected to in-plane stresses. *International Journal of Mechanical Sciences*, 43(8):1925–1944, 2001. ISSN 0020-7403. doi: https://doi.org/10.1016/S0020-7403(01)00002-9.

A. Milazzo and V. Oliveri. Buckling and postbuckling of stiffened composite panels with cracks and delaminations by ritz approach. *AIAA Journal*, 55(3):965–980, 2017. doi: 10.2514/1.J055159.

T. Möcker and H.-G. Reimerdes. Postbuckling simulation of curved stiffened composite panels by the use of strip elements. *Composite Structures*, 73(2):237–243, May 2006. ISSN 0263-8223. doi: 10.1016/j.compstruct.2005.11.061.

H. Ovesy and H. Assaee. The effects of bend–twist coupling on the post-buckling characteristics of composite laminated plates using semi-energy finite strip approach. *Thin-Walled Structures*, 45(2):209–220, 2007. ISSN 0263-8231. doi: https://doi.org/10.1016/j.tws.2007.01.016.

S. A. Ragon, Z. Gürdal, and L. T. Watson. A comparison of three algorithms for tracing nonlinear equilibrium paths of structural systems. *International Journal of Solids and Structures*, 39(3):689–698, Feb. 2002. ISSN 0020-7683. doi: 10.1016/s0020-7683(01)00195-0.

G. Raju, Z. Wu, and P. M. Weaver. Postbuckling analysis of variable angle tow plates using differential quadrature method. *Composite Structures*, 106:74–84, Dec. 2013. ISSN 0263-8223. doi: 10.1016/j.compstruct.2013.05.010.

J. N. Reddy and C. Liu. A higher-order theory for geometrically nonlinear analysis of composite laminates. Technical report, NASA, 1987.

L. W. Rehfield, S. Chang, and P. J. Zischka. Modeling and analysis methodology for aeroelastically tailored chordwise deformable wings. Technical report, 1992.

R. Rikards, H. Abramovich, K. Kalnins, and J. Auzins. Surrogate modeling in design optimization of stiffened composite shells. *Composite Structures*, 73(2): 244–251, May 2006. ISSN 0263-8223. doi: 10.1016/j.compstruct.2005.11.046.

J. C. Schilling and C. Mittelstedt. Approximate computational model for the local postbuckling of omega-stringer-stiffened composite panels. *PAMM*, 22(1), Mar. 2023. ISSN 1617-7061. doi: 10.1002/pamm.202200152.

O. Seresta. Buckling, flutter, and postbuckling optimization of composite structures. *Virginia Tech*, 2007.

O. Seresta, M. M. Abdalla, and Z. Gürdal. Approximate internal load prediction in composite structures with locally buckled panels. *Journal of Aircraft*, 45(2): 513–522, Mar. 2008. ISSN 1533-3868. doi: 10.2514/1.30465.

H.-S. Shen. Postbuckling analysis of shear-deformable composite laminated plates on two-parameter elastic foundations. *Mechanics of Composite Materials and Structures*, 7(3):249–268, 2000. doi: 10.1080/10759410050031103.

H.-S. Shen and F. Williams. Biaxial buckling and post-buckling of composite laminated plates on two-parameter elastic foundations. *Computers & Structures*, 63(6):1177–1185, 1997. ISSN 0045-7949. doi: https://doi.org/10.1016/S0045-7949(96)00398-7.

Y. Sun, K. Tian, R. Li, and B. Wang. Accelerated koiter method for post-buckling analysis of thin-walled shells under axial compression. *Thin-Walled Structures*, 155:106962, 2020. ISSN 0263-8231. doi: https://doi.org/10.1016/j.tws.2020.106962.

B. Szabó and I. Babuška. *Finite Element Analysis: Method, Verification and Validation*. John Wiley & Sons, Hoboken, NJ, 2nd edition, 2021. ISBN 978-1-119-42642-4.

F. Taheri and S. Moradi. A robust methodology for the simulation of postbuckling response of composite plates. *Computational Mechanics*, 26(3):295–301, Sept. 2000. ISSN 1432-0924. doi: 10.1007/s004660000173.

S. White, G. Raju, and P. Weaver. Initial post-buckling of variable-stiffness curved panels. *Journal of the Mechanics and Physics of Solids*, 71:132–155, Nov. 2014. ISSN 0022-5096. doi: 10.1016/j.jmps.2014.07.003.

F. W. Williams, D. Kennedy, R. Butler, and M. S. Anderson. Viconopt - program for exact vibration and buckling analysis or design of prismatic plate assemblies. *AIAA Journal*, 29(11):1927–1928, Nov. 1991. ISSN 1533-385X. doi: 10.2514/3.10820.

C. Zhang. *Postbuckling analysis of isotropic and anisotropic plate assemblies under combined loading*. PhD thesis, Cardiff University, 2018.

K. Zhao. *CWPAN: coupled wavelength postbuckling analysis*. PhD thesis, Cardiff University, 2021.

G. Zou and P. Qiao. Higher-order finite strip method for postbuckling analysis of imperfect composite plates. *Journal of Engineering Mechanics*, 128(9):1008–1015, 2002. doi: 10.1061/(ASCE)0733-9399(2002)128:9(1008).

Appendix

2.A. Tensor Definitions

Tensors in Equation 2.26 are expanded as follows:

$$K_{il}^{g} = \bar{K}_{il}^{g} - \begin{bmatrix} K_{lip}^{wba} & K_{lip}^{wca} \end{bmatrix} (K^{a})_{ps}^{-1} \begin{Bmatrix} g_{s}^{u} \\ g_{s}^{v} \end{Bmatrix}$$

$$K_{lkji}^{\mathrm{NL}} = K_{lkji}^{waaa} - \begin{bmatrix} K_{lkp}^{wba} K_{lkp}^{wca} \end{bmatrix} (K^{a})_{ps}^{-1} K_{sji}^{uvaa},$$

where:

$$[\boldsymbol{K}^{a}] = \begin{bmatrix} [\boldsymbol{K}^{ub}] & [\boldsymbol{K}^{uc}] \\ [\boldsymbol{K}^{vb}] & [\boldsymbol{K}^{vc}] \end{bmatrix}.$$

The full tensor definitions are defined here. Starting with first-order tensors:

$$g_{l}^{ux} = \int_{0}^{A} \int_{0}^{B} A_{11} \phi_{l,x}^{u} \, dy dx$$

$$g_{l}^{uy} = \int_{0}^{A} \int_{0}^{B} A_{12} \phi_{l,x}^{u} \, dy dx$$

$$g_{l}^{uxy} = \int_{0}^{A} \int_{0}^{B} A_{66} \phi_{l,y}^{u} \, dy dx$$

$$g_{l}^{vx} = \int_{0}^{A} \int_{0}^{B} A_{12} \phi_{l,y}^{v} \, dy dx$$

$$g_{l}^{vy} = \int_{0}^{A} \int_{0}^{B} A_{22} \phi_{l,y}^{v} \, dy dx$$

$$g_{l}^{vxy} = \int_{0}^{A} \int_{0}^{B} A_{66} \phi_{l,x}^{v} \, dy dx.$$

Second-order tensors:

$$K_{il}^{ub} = \int_{0}^{A} \int_{0}^{B} \left[A_{11} \phi_{i,x}^{u} \phi_{l,x}^{u} + A_{66} \phi_{i,y}^{u} \phi_{l,y}^{u} \right] dy \, dx$$

$$K_{il}^{uc} = \int_{0}^{A} \int_{0}^{B} \left[A_{12} \phi_{i,y}^{v} \phi_{l,x}^{u} + A_{66} \phi_{i,x}^{v} \phi_{l,y}^{u} \right] dy \, dx$$

$$K_{il}^{vb} = \int_{0}^{A} \int_{0}^{B} \left[A_{12} \phi_{i,x}^{u} \phi_{l,y}^{v} + A_{66} \phi_{i,y}^{u} \phi_{l,x}^{v} \right] dy \, dx$$

$$K_{il}^{vc} = \int_{0}^{A} \int_{0}^{B} \left[A_{22} \phi_{i,y}^{v} \phi_{l,y}^{v} + A_{66} \phi_{i,x}^{v} \phi_{l,x}^{v} \right] dy \, dx$$

$$\begin{aligned} K_{il} = \int_{0}^{A} \int_{0}^{B} \Big[& D_{11} \phi_{i,xx}^{w} \phi_{l,xx}^{w} + D_{12} \phi_{i,yy}^{w} \phi_{l,xx}^{w} + D_{12} \phi_{i,xx}^{w} \phi_{l,yy}^{w} \\ & + 2D_{16} \phi_{i,xx}^{w} \phi_{l,xy}^{w} + 2D_{16} \phi_{i,xy}^{w} \phi_{l,xx}^{w} + 2D_{26} \phi_{i,xy}^{w} \phi_{l,yy}^{w} \\ & + 2D_{26} \phi_{i,yy}^{w} \phi_{l,xy}^{w} + D_{22} \phi_{i,yy}^{w} \phi_{l,yy}^{w} + 4D_{66} \phi_{i,xy}^{w} \phi_{l,xy}^{w} \Big] dy \, dx \end{aligned}$$

$$\bar{K}_{il}^{gx} = \int_0^A \int_0^B \left[A_{11}\phi_{i,x}^w \phi_{l,x}^w + A_{12}\phi_{i,y}^w \phi_{l,y}^w\right] dy\, dx$$
$$\bar{K}_{il}^{gy} = \int_0^A \int_0^B \left[A_{12}\phi_{i,x}^w \phi_{l,x}^w + A_{22}\phi_{i,y}^w \phi_{l,y}^w\right] dy\, dx$$
$$\bar{K}_{il}^{gxy} = \int_0^A \int_0^B \left[A_{66}\phi_{i,y}^w \phi_{l,x}^w + A_{66}\phi_{i,x}^w \phi_{l,y}^w\right] dy\, dx.$$

Third-order tensors:

$$K_{ijl}^{uaa} = \frac{1}{2}\int_0^A \int_0^B \Big[A_{11}\phi_{i,x}^w \phi_{j,x}^w \phi_{l,x}^u + A_{12}\phi_{i,y}^w \phi_{j,y}^w \phi_{l,x}^u + A_{66}\phi_{i,x}^w \phi_{j,y}^w \phi_{l,y}^u + A_{66}\phi_{i,y}^w \phi_{j,x}^w \phi_{l,y}^u\Big] dy\, dx$$

$$K_{ijl}^{vaa} = \frac{1}{2}\int_0^A \int_0^B \Big[A_{12}\phi_{i,x}^w \phi_{j,x}^w \phi_{l,y}^v + A_{22}\phi_{i,y}^w \phi_{j,y}^w \phi_{l,y}^v + A_{66}\phi_{i,x}^w \phi_{j,y}^w \phi_{l,x}^v + A_{66}\phi_{i,y}^w \phi_{j,x}^w \phi_{l,x}^v\Big] dy\, dx$$

$$K_{ikl}^{wba} = \int_0^A \int_0^B \Big[A_{11}\phi_{i,x}^u \phi_{k,x}^w \phi_{l,x}^w + A_{12}\phi_{i,x}^u \phi_{k,y}^w \phi_{l,y}^w + A_{66}\phi_{i,y}^u \phi_{k,y}^w \phi_{l,x}^w + A_{66}\phi_{i,y}^u \phi_{k,x}^w \phi_{l,y}^w\Big] dy\, dx$$

$$K_{ikl}^{wca} = \int_0^A \int_0^B \Big[A_{12}\phi_{i,y}^v \phi_{k,x}^w \phi_{l,x}^w + A_{22}\phi_{i,y}^v \phi_{k,y}^w \phi_{l,y}^w + A_{66}\phi_{i,x}^v \phi_{k,y}^w \phi_{l,x}^w + A_{66}\phi_{i,x}^v \phi_{k,x}^w \phi_{l,y}^w\Big] dy\, dx.$$

Fourth-order tensor:

$$\begin{aligned}\bar{K}_{ijkl}^{waaa} = \frac{1}{2}\int_0^A \int_0^B \Big[&A_{11}\phi_{i,x}^w \phi_{j,x}^w \phi_{k,x}^w \phi_{l,x}^w + A_{12}\phi_{i,y}^w \phi_{j,y}^w \phi_{k,x}^w \phi_{l,x}^w \\ &+ A_{12}\phi_{i,x}^w \phi_{j,x}^w \phi_{k,y}^w \phi_{l,y}^w + A_{22}\phi_{i,y}^w \phi_{j,y}^w \phi_{k,y}^w \phi_{l,y}^w \\ &+ A_{66}\phi_{i,x}^w \phi_{j,y}^w \phi_{k,y}^w \phi_{l,x}^w + A_{66}\phi_{i,x}^w \phi_{j,y}^w \phi_{k,x}^w \phi_{l,y}^w \\ &+ A_{66}\phi_{i,y}^w \phi_{j,x}^w \phi_{k,y}^w \phi_{l,x}^w + A_{66}\phi_{i,y}^w \phi_{j,x}^w \phi_{k,x}^w \phi_{l,y}^w\Big] dy\, dx.\end{aligned}$$

2.B. Integral Derivations

In this appendix, some examples of deriving a closed-form solution for integrals are provided.

1. Definition of the PP integral

$$I^{PP}_{(i,j)} = \int_{-1}^{1} P_i(\xi)P_j(\xi)\,d\xi = \begin{cases} 0 & \text{if } i \neq j \\ \int_{-1}^{1} P_i^2(\xi)\,d\xi = \dfrac{2}{2i+1} & \text{if } i = j \end{cases}$$

2. Definition of the PL integral

$$I^{PL}_{(i,j)} = \int_{-1}^{1} P_i(\xi)L_j(\xi)\,d\xi$$

Case 1: For $j < 2$: The expressions for L_j are:

$$L_0 = \tfrac{1}{2}P_0 + \tfrac{1}{2}P_1, \quad L_1 = \tfrac{1}{2}P_0 - \tfrac{1}{2}P_1.$$

For example:

$$j = 0: \quad \Rightarrow \quad P_iL_0 = \tfrac{1}{2}P_iP_0 + \tfrac{1}{2}P_iP_1, \quad \Rightarrow \quad I^{PL}_{(i,0)} = \tfrac{1}{2}I^{PP}_{(i,0)} + \tfrac{1}{2}I^{PP}_{(i,1)}.$$

$$j = 1: \quad P_iL_1 = \tfrac{1}{2}P_iP_0 - \tfrac{1}{2}P_iP_1, \quad \Rightarrow \quad I^{PL}_{(i,1)} = \tfrac{1}{2}I^{PP}_{(i,0)} - \tfrac{1}{2}I^{PP}_{(i,1)}.$$

Case 2: For $j \geq 2$: Use the recurrence relation:

$$(2j-1)L_j = P_j - P_{j-2} \quad \Rightarrow \quad L_j = \frac{1}{2j-1}(P_j - P_{j-2}).$$

$$\Rightarrow I^{PL}_{(i,j)} = \frac{1}{2j-1}\left(I^{PP}_{(i,j)} - I^{PP}_{(i,j-2)}\right).$$

3. Definition of the PH" integral

$$I^{PH''}_{(i,j)} = \int_{-1}^{1} P_i(\xi)H''_j(\xi)\,d\xi$$

Case 1: For $j < 4$: The expressions for H''_j are:

$$H''_0 = \tfrac{3}{2}P_1, \quad H''_1 = -\tfrac{3}{2}P_1, \quad H''_2 = \tfrac{-1}{2}P_0 + \tfrac{3}{2}P_1, \quad H''_3 = \tfrac{1}{2}P_0 + \tfrac{3}{2}P_1. \tag{2.49}$$

For example:

$$j = 0: \quad \Rightarrow \quad P_iH''_0 = \tfrac{3}{2}P_iP_1, \quad \Rightarrow I^{PH''}_{(i,0)} = \tfrac{3}{2}I^{PP}_{(i,1)}.$$

Case 2: For $j \geq 4$:

$$H''_j = P_{j-2} \quad \Rightarrow \quad I^{PH''}_{(i,j)} = \int_{-1}^{1} P_iP_{j-2}\,d\xi = I^{PP}_{(i,j-2)}.$$

4. DEFINITION OF THE PH INTEGRAL

$$I^{PH}_{(i,j)} = \int_{-1}^{1} P_i(\xi) H_j(\xi)\, d\xi$$

Case 1: For $j < 4$: The expressions for H_j are:

$$\begin{aligned} H_0 &= \tfrac{1}{2}P_0 - \tfrac{12}{20}P_1 + \tfrac{1}{10}P_3, & H_1 &= \tfrac{1}{2}P_0 + \tfrac{12}{20}P_1 - \tfrac{1}{10}P_3, \\ H_2 &= \tfrac{1}{6}P_0 - \tfrac{1}{10}P_1 - \tfrac{1}{6}P_2 + \tfrac{1}{10}P_3, & H_3 &= -\tfrac{1}{6}P_0 - \tfrac{1}{10}P_1 + \tfrac{1}{6}P_2 + \tfrac{1}{10}P_3. \end{aligned} \tag{2.50}$$

For example:

$$j = 0: \quad I^{PH}_{(i,0)} = \tfrac{1}{2} I^{PP}_{(i,0)} - \tfrac{12}{20} I^{PP}_{(i,1)} + \tfrac{1}{10} I^{PP}_{(i,3)}.$$

Case 2: For $j \geq 4$: Use the recurrence relation:

$$H_j = \frac{1}{2j-3}\left[\frac{1}{2j-1}(P_j - P_{j-2}) - \frac{1}{2j-5}(P_{j-2} - P_{j-4})\right] \tag{2.51}$$

$$\Rightarrow I^{PH}_{(i,j)} = \frac{I^{PP}_{(i,j)} - I^{PP}_{(i,j-2)}}{(2j-3)(2j-1)} - \frac{I^{PP}_{(i,j-2)} - I^{PP}_{(i,j-4)}}{(2j-5)(2j-3)}.$$

5. DEFINITION OF THE PPP INTEGRAL

The triple Legendre polynomial integral is defined as:

$$I^{PPP}_{(i,j,k)} = \int_{-1}^{1} P_i(\xi)\, P_j(\xi)\, P_k(\xi)\, d\xi$$

This integral evaluates to zero unless the following conditions are satisfied:

- $i + j + k$ is even,
- $j + k \geq i$,
- $i \geq |j - k|$.

If these conditions hold, the integral can be evaluated using Gaunt's formula (Gaunt, 1929):

$$I^{PPP}_{(i,j,k)} = 2(-1)^{s-j} \frac{s! \cdot (2s-2k)! \cdot j! \cdot k!}{(s-i)!(s-j)!(s-k)!(2s+1)!} \times \sum_{t=p}^{q} (-1)^t \frac{(i+t)!(j+k-t)!}{t!(i-t)!(j-k+t)!(k-t)!}$$

where:

$$s = \frac{i+j+k}{2}, \quad p = \max(0, k-j), \quad q = \min(j+k, i, k).$$

6. Definition of the PHH integral

$$I^{PHH}_{(i,j,k)} = \int_{-1}^{1} P_i(\xi) H_j(\xi) H_k(\xi)\, d\xi$$

We assume throughout that $j \leq k$ to avoid redundant expressions.

Case 1: For $k < 4$: Use the expressions for H_j and H_k given in Equation 2.50. *For example:*

$$\begin{aligned} I^{PHH}_{(i,0,2)} = {} & \tfrac{1}{12} I^{PPP}_{(i,0,0)} - \tfrac{3}{20} I^{PPP}_{(i,0,1)} + \tfrac{3}{50} I^{PPP}_{(i,1,1)} - \tfrac{1}{12} I^{PPP}_{(i,0,2)} \\ & + \tfrac{1}{10} I^{PPP}_{(i,1,2)} + \tfrac{1}{15} I^{PPP}_{(i,0,3)} - \tfrac{7}{100} I^{PPP}_{(i,1,3)} - \tfrac{1}{60} I^{PPP}_{(i,2,3)} + \tfrac{1}{100} I^{PPP}_{(i,3,3)}. \end{aligned}$$

Case 2: For $j < 4$, $k \geq 4$: Use Equation 2.50 for H_j and the recurrence relation for H_k from Equation 2.51.
For example:

$$\begin{aligned} I^{PHH}_{(i,0,k)} = {} & \frac{I^{PPP}_{(i,0,k)} - I^{PPP}_{(i,0,k-2)}}{2(2k-3)(2k-1)} - \frac{I^{PPP}_{(i,0,k-2)} - I^{PPP}_{(i,0,k-4)}}{2(2k-5)(2k-3)} \\ & - \frac{3}{5}\left[\frac{I^{PPP}_{(i,1,k)} - I^{PPP}_{(i,1,k-2)}}{(2k-3)(2k-1)} - \frac{I^{PPP}_{(i,1,k-2)} - I^{PPP}_{(i,1,k-4)}}{(2k-5)(2k-3)} \right] \\ & + \frac{1}{10}\left[\frac{I^{PPP}_{(i,3,k)} - I^{PPP}_{(i,3,k-2)}}{(2k-3)(2k-1)} - \frac{I^{PPP}_{(i,3,k-2)} - I^{PPP}_{(i,3,k-4)}}{(2k-5)(2k-3)} \right]. \end{aligned}$$

Case 3: For $j \geq 4$: Use the recurrence relation Equation 2.51 for both H_j and H_k.

$$\begin{aligned} I^{PHH}_{(i,j,k)} = {} & \frac{1}{(2j-5)(2j-3)(2j-1)(2k-5)(2k-3)(2k-1)} \\ & \times \Big[(2j-5)(2k-5) I^{PPP}_{(i,j,k)} - (2j-5)(4k-6) I^{PPP}_{(i,j,k-2)} + (2j-5)(2k-1) I^{PPP}_{(i,j,k-4)} \\ & - (4j-6)(2k-5) I^{PPP}_{(i,j-2,k)} + (4j-6)(4k-6) I^{PPP}_{(i,j-2,k-2)} - (4j-6)(2k-1) I^{PPP}_{(i,j-2,k-4)} \\ & + (2j-1)(2k-5) I^{PPP}_{(i,j-4,k)} - (2j-1)(4k-6) I^{PPP}_{(i,j-4,k-2)} + (2j-1)(2k-1) I^{PPP}_{(i,j-4,k-4)} \Big] \end{aligned}$$

7. Definition of the PHH' integral

$$I^{PHH'}_{(i,j,k)} = \int_{-1}^{1} P_i(\xi)\, H_j(\xi)\, H'_k(\xi)\, d\xi$$

Case 1: For $j < 4$, $k < 4$:

Use the expressions for H_j from Equation 2.50 and the following for H'_k:

$$H'_0 = \tfrac{1}{2}(-P_0 + P_2), \quad H'_1 = \tfrac{1}{2}(P_0 - P_2), \quad H'_2 = \tfrac{1}{2}(-P_1 + P_2), \quad H'_3 = \tfrac{1}{2}(P_1 + P_2) \tag{2.52}$$

For example:

$$I^{PHH'}_{(i,0,2)} = -\tfrac{1}{4}I^{PPP}_{(i,0,0)} + \tfrac{3}{10}I^{PPP}_{(i,0,1)} + \tfrac{1}{4}I^{PPP}_{(i,0,2)} - \tfrac{3}{10}I^{PPP}_{(i,1,2)} - \tfrac{1}{20}I^{PPP}_{(i,0,3)} + \tfrac{1}{20}I^{PPP}_{(i,2,3)}$$

Case 2: For $j < 4$, $k \geq 4$:

Use the expressions for H_j from Equation 2.50 and the recurrence for H'_k:

$$H'_k = L_{k-1} = \frac{1}{2k-3}\left(P_{k-1} - P_{k-3}\right) \tag{2.53}$$

For example:

$$I^{PHH'}_{(i,0,k)} = \frac{1}{20k-30}\Big[5\left(I^{PPP}_{(i,0,k-1)} - I^{PPP}_{(i,0,k-3)}\right) - 6\left(I^{PPP}_{(i,1,k-1)} - I^{PPP}_{(i,1,k-3)}\right) + \left(I^{PPP}_{(i,3,k-1)} - I^{PPP}_{(i,3,k-3)}\right)\Big]$$

Case 3: For $j \geq 4$, $k < 4$:

Use the recurrence form for H_j from Equation 2.51, and the explicit expressions in Equation 2.52 for H'_k.

$$I^{PHH'}_{(i,j,k)} = \frac{1}{(2j-5)(2j-3)(2j-1)} \times \Big[(2j-5)\left(I^{PPP}_{(i,j,k-1)} - I^{PPP}_{(i,j,k-3)}\right) - (4j-6)\left(I^{PPP}_{(i,j-2,k-1)} - I^{PPP}_{(i,j-2,k-3)}\right) + (2j-1)\left(I^{PPP}_{(i,j-4,k-1)} - I^{PPP}_{(i,j-4,k-3)}\right)\Big]$$

Case 4: For $j \geq 4$, $k \geq 4$:

Use recurrence expressions for both H_j and H'_k.

$$I^{PHH'}_{(i,j,k)} = \frac{1}{(2j-5)(2j-3)(2j-1)(2k-3)} \times \Big[(2j-5)\left(I^{PPP}_{(i,j,k-1)} - I^{PPP}_{(i,j,k-3)}\right) - (4j-6)\left(I^{PPP}_{(i,j-2,k-1)} - I^{PPP}_{(i,j-2,k-3)}\right) + (2j-1)\left(I^{PPP}_{(i,j-4,k-1)} - I^{PPP}_{(i,j-4,k-3)}\right)\Big]$$

The previously provided integrals serve as an example to show how the derivation is done. The rest of the integrals can be derived in the same manner.

2.C. Application of Integral Expressions

This appendix provides examples demonstrating how the closed-form integral expressions derived in Appendix 2.B can be directly applied to evaluate tensor quantities defined in Appendix 2.A.

Example: Evaluation of g_l^{ux}

Given the tensor definition:

$$g_l^{ux} = \int_0^A \int_0^B A_{11}\, \phi_{l,x}^u \, dy \, dx$$

A coordinate transformation from the physical domain (x, y), where $x \in [0, A]$ and $y \in [0, B]$, to a normalized domain (ζ, η), where $\zeta \in [-1, 1]$ and $\eta \in [-1, 1]$, is done:

$$g_l^{ux} = \frac{AB}{4} \int_{-1}^1 \int_{-1}^1 A_{11}\, \phi_{l,x}^u \, d\eta \, d\zeta$$

Since the scalar factor $\frac{AB}{4}$ is common to all tensors, it can be dropped safely because the final governing equations involve tensor expressions set to zero.

$$g_l^{ux} = \int_{-1}^1 \int_{-1}^1 A_{11}\, \phi_{l,x}^u \, d\eta \, d\zeta$$

Due to the transformation from x to ζ, the derivative transforms as:

$$\phi_{l,x}^u = \frac{2}{A} \frac{\partial \phi_l^u}{\partial \zeta}$$

Using the previously defined form of the shape function:

$$\phi_l^u(\zeta, \eta) = L_m(\zeta)\, L_n(\eta),$$

we obtain the following expression for its partial derivative:

$$\phi_{l,x}^u = \frac{2}{A} \frac{\partial \phi_l^u}{\partial \zeta} = \frac{2}{A} L'_m(\zeta)\, L_n(\eta)$$

Substituting into the integral:

$$g_l^{ux} = \frac{2}{A} \int_{-1}^1 \int_{-1}^1 A_{11}\, L'_m(\zeta)\, L_n(\eta)\, d\eta \, d\zeta$$

Assuming A_{11} is constant:

$$g_l^{ux} = \frac{2A_{11}}{A} \left(\int_{-1}^1 L'_m(\zeta)\, d\zeta \right) \left(\int_{-1}^1 L_n(\eta)\, d\eta \right)$$

The resulting expression reduces to two separable one-dimensional integrals, for which closed-form solutions can be obtained as demonstrated in Appendix 2.B.

EXAMPLE: EVALUATION OF THE K_{ikl}^{wba} TENSOR

The tensor K_{ikl}^{wba}, as defined in Appendix 2.A, is given by:

$$K_{ikl}^{wba} = \int_0^A \int_0^B \Big[A_{11}\, \phi_{i,x}^{u}\, \phi_{k,x}^{w}\, \phi_{l,x}^{w} + A_{12}\, \phi_{i,x}^{u}\, \phi_{k,y}^{w}\, \phi_{l,y}^{w} + A_{66}\, \phi_{i,y}^{u}\, \phi_{k,y}^{w}\, \phi_{l,x}^{w} + A_{66}\, \phi_{i,y}^{u}\, \phi_{k,x}^{w}\, \phi_{l,y}^{w} \Big]\, dy\, dx$$

After expressing the shape functions in terms of their ζ and η mappings and omitting the constant geometric scaling factor $\frac{AB}{4}$, the integrand becomes:

$$\begin{aligned} K_{ikl}^{wba} = \int_{-1}^{1} \int_{-1}^{1} \Big[& \frac{8A_{11}}{A^3}\, L'_{m_i}(\zeta)\, L_{n_i}(\eta)\, H'_{m_k}(\zeta)\, H_{n_k}(\eta)\, H'_{m_l}(\zeta)\, H_{n_l}(\eta) \\ & + \frac{8A_{12}}{AB^2}\, L'_{m_i}(\zeta)\, L_{n_i}(\eta)\, H_{m_k}(\zeta)\, H'_{n_k}(\eta)\, H_{m_l}(\zeta)\, H'_{n_l}(\eta) \\ & + \frac{8A_{66}}{AB^2}\, L_{m_i}(\zeta)\, L'_{n_i}(\eta)\, H'_{m_k}(\zeta)\, H_{n_k}(\eta)\, H_{m_l}(\zeta)\, H'_{n_l}(\eta) \\ & + \frac{8A_{66}}{AB^2}\, L_{m_i}(\zeta)\, L'_{n_i}(\eta)\, H_{m_k}(\zeta)\, H'_{n_k}(\eta)\, H'_{m_l}(\zeta)\, H_{n_l}(\eta) \Big]\, d\eta\, d\zeta \end{aligned}$$

The expression above can now be separated into products of one-dimensional integrals:

$$\begin{aligned} K_{ikl}^{wba} = & \frac{8A_{11}}{A^3} \left(\int_{-1}^{1} L'_{m_i}(\zeta) H'_{m_k}(\zeta) H'_{m_l}(\zeta)\, d\zeta \right) \left(\int_{-1}^{1} L_{n_i}(\eta) H_{n_k}(\eta) H_{n_l}(\eta)\, d\eta \right) \\ & + \frac{8A_{12}}{AB^2} \left(\int_{-1}^{1} L'_{m_i}(\zeta) H_{m_k}(\zeta) H_{m_l}(\zeta)\, d\zeta \right) \left(\int_{-1}^{1} L_{n_i}(\eta) H'_{n_k}(\eta) H'_{n_l}(\eta)\, d\eta \right) \\ & + \frac{8A_{66}}{AB^2} \left(\int_{-1}^{1} L_{m_i}(\zeta) H'_{m_k}(\zeta) H_{m_l}(\zeta)\, d\zeta \right) \left(\int_{-1}^{1} L'_{n_i}(\eta) H_{n_k}(\eta) H'_{n_l}(\eta)\, d\eta \right) \\ & + \frac{8A_{66}}{AB^2} \left(\int_{-1}^{1} L_{m_i}(\zeta) H_{m_k}(\zeta) H'_{m_l}(\zeta)\, d\zeta \right) \left(\int_{-1}^{1} L'_{n_i}(\eta) H'_{n_k}(\eta) H_{n_l}(\eta)\, d\eta \right) \end{aligned}$$

As in the previous example, the final expression consists of two separable one-dimensional integrals, each of which can be evaluated in closed form using the formulations demonstrated in Appendix 2.B.

2.D. Derivation of the Iterative Scheme (Normal Flow Algorithm)

This appendix summarises the derivation of the iterative scheme based on the Normal Flow Algorithm (NFA), as used in Section 2.4.2. The algorithm is applied within a prediction–correction framework to trace the nonlinear equilibrium path. The non-linear equilibrium Equation 2.26 can be rewritten as:

$$\boldsymbol{f}\left(\boldsymbol{a}, \lambda\right) = \boldsymbol{0} \tag{2.54}$$

Starting from a known solution on the equilibrium path, here chosen as the linear buckling solution:

$$\boldsymbol{z_n^*} = \left(\boldsymbol{a_n^*}, \lambda_n^*\right)^T, \tag{2.55}$$

A series of prediction–correction steps follows. The prediction step estimates the next point on the equilibrium path:

$$\boldsymbol{z_{n+1}^0} = \left(\boldsymbol{a_{n+1}^0}, \lambda_{n+1}^0\right)^T. \tag{2.56}$$

The correction step is carried out through the NFA by employing Newton—Raphson iterations. Convergence is achieved along a direction normal to the Davidenko flow (Ragon et al., 2002, Allgower and Georg, 1990). This direction represents paths parallel to the equilibrium curve:

$$\boldsymbol{f}\left(\boldsymbol{a}, \lambda\right) = \boldsymbol{\delta}, \tag{2.57}$$

where δ is a perturbation parameter controlling the offset from the equilibrium path.

Expanding in a Taylor series and neglecting higher–order terms gives:

$$\underbrace{\begin{bmatrix} \dfrac{\partial \boldsymbol{f}}{\partial \boldsymbol{a}} & \dfrac{\partial \boldsymbol{f}}{\partial \lambda} \end{bmatrix}}_{\boldsymbol{J_f}} \Delta \boldsymbol{z} = -\boldsymbol{f}(\boldsymbol{a_n}, \lambda_n). \tag{2.58}$$

Since this system is underdetermined, Seresta (2007) suggested augmenting it with an additional condition to obtain the minimum–norm solution:

$$\boldsymbol{p} \cdot \Delta \boldsymbol{z} = 0, \tag{2.59}$$

where $\boldsymbol{p}$ lies in the null space of $\boldsymbol{J_f}$.

This derivation follows established treatments (Ragon et al., 2002, Seresta, 2007, Allgower and Georg, 1990) and is included here for completeness.

2.E. Results Presented in Imperial Units

Table 2.5: Comparison of different approaches for multiple laminate layups.

Stacking Seq.	(u_0/v_0) $\times 10^{-3}$	λ_f	Literature (Seresta et al., 2008)		Abaqus simulation			Present approach			Present/Abaqus		
			$\bar{N}_x$	$\bar{N}_y$	λ_{cr}	$\bar{N}_x$	$\bar{N}_y$	λ_{cr}	$\bar{N}_x$	$\bar{N}_y$	$R_{\lambda_{cr}}$	$R_{\bar{N}_x}$	$R_{\bar{N}_y}$
$[(0\ 90)_4]_s$	1/0	13.96	767.6	-303.61	1.23	672.2	-345.4	1.22	791.39	-395.69	0.99	1.18	1.15
$[(0\ 90)_4]_s$	1/1	8.29	268.96	268.96	0.605	235.9	229.5	0.608	234.97	234.97	1.005	0.996	1.02
$[(0\ 90)_4]_s$	1.5/1	7.02	417.3	147.9	0.485	371.12	109.35	0.486	397.96	99.49	1.002	1.07	0.91
$[(0\ 90)_4]_s$	2/1	6.13	529.68	59.31	0.404	468.45	21.74	0.405	521.26	0.008	1.002	1.11	0.0003
$[(45\ 90\ -45\ 90)_2]_s$	1/0	19.93	436.97	-31.83	2.68	360.13	59.00	2.74	567.22	-362.71	1.02	1.58	-6.15
$[(45\ -45)_4]_s$	1/1	12.12	290.81	290.81	0.954	189.10	189.10	0.986	300.04	300.04	1.03	1.59	1.59

Units:
$\bar{N}_x, \bar{N}_y$: lbf/in
u_0, v_0: in
λ_{cr}, λ_f: dimensionless

Ratios are dimensionless and defined as: R = Present Approach/Abaqus.

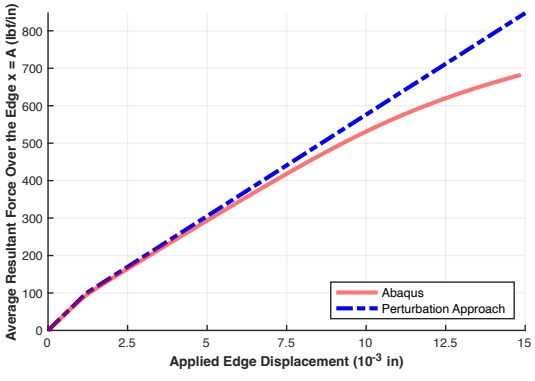

(a) $[(0/90)_4]_s$ laminate under uniaxial edge displacement $u_0/v_0 = 1/0$.

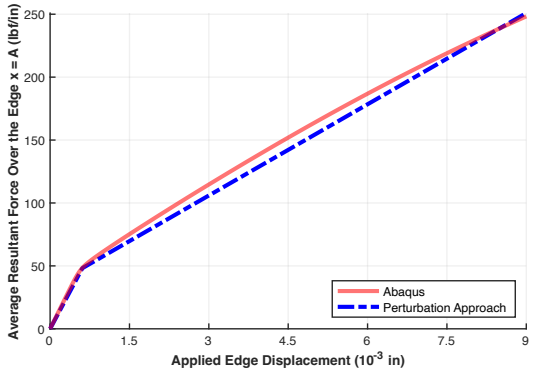

(b) $[(0/90)_4]_s$ laminate under biaxial edge displacement $u_0/v_0 = 1/1$.

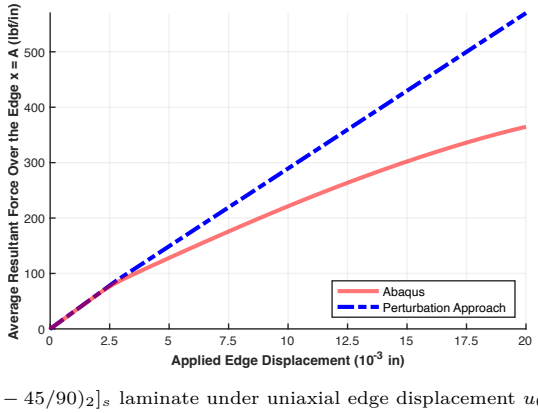

(c) $[(45/90/-45/90)_2]_s$ laminate under uniaxial edge displacement $u_0/v_0 = 1/0$.

Figure 2.11: Comparison between perturbation method and Abaqus predictions for the relationship between the imposed edge displacement and the averaged edge force resultant for three laminate configurations.

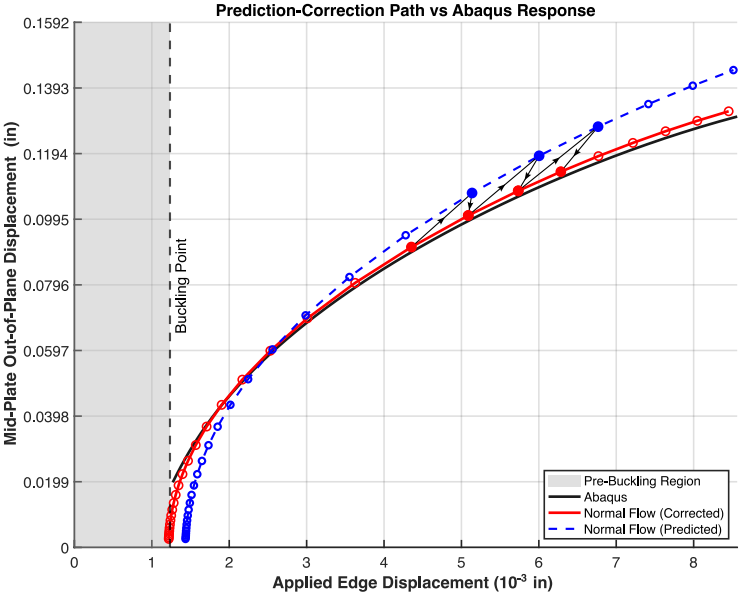

Figure 2.12: Prediction and corrected nonlinear paths for a $[(0/90)_4]_s$ laminate under uniaxial loading ($u_0/v_0 = 1/0$).

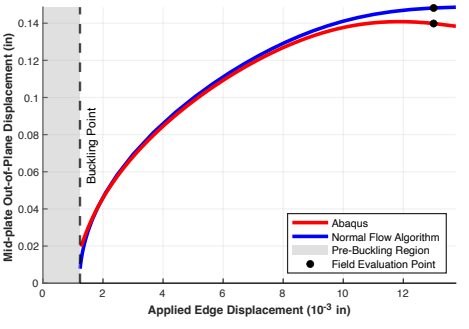

(a) Mid-plate out-of-plane displacement response under applied edge displacement.

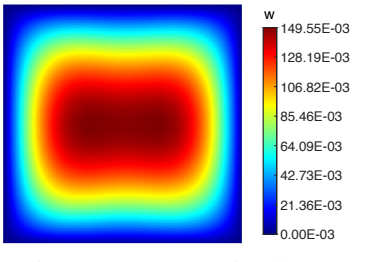

(b) Out-of-plane displacement field from the NFA.

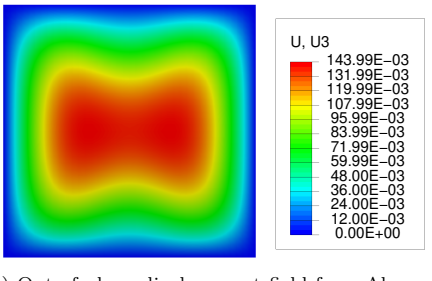

(c) Out-of-plane displacement field from Abaqus.

Figure 2.13: Postbuckling response and displacement fields: Laminate $[(0/90)_4]_s$, $u_0/v_0 = 1/0$.

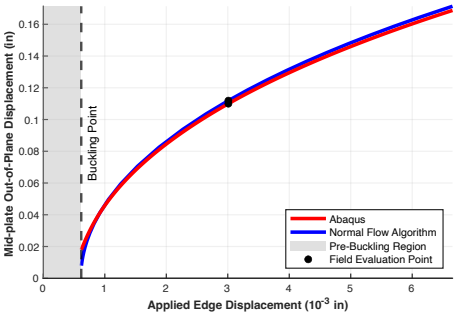

(a) Mid-plate out-of-plane displacement response under applied edge displacement.

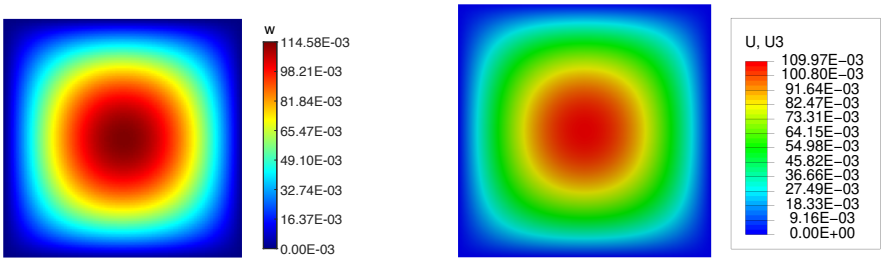

(b) Out-of-plane displacement field from the NFA. (c) Out-of-plane displacement field from Abaqus.

Figure 2.14: Postbuckling response and displacement fields: Laminate $[(0/90)_4]_s$, $u_0/v_0 = 1/1$.

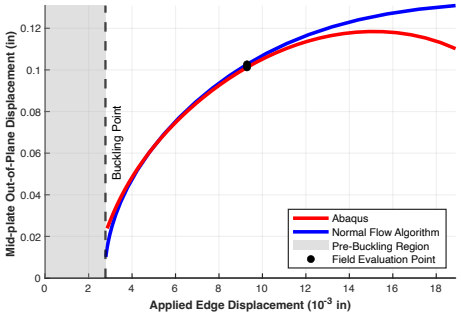

(a) Mid-plate out-of-plane displacement response under applied edge displacement.

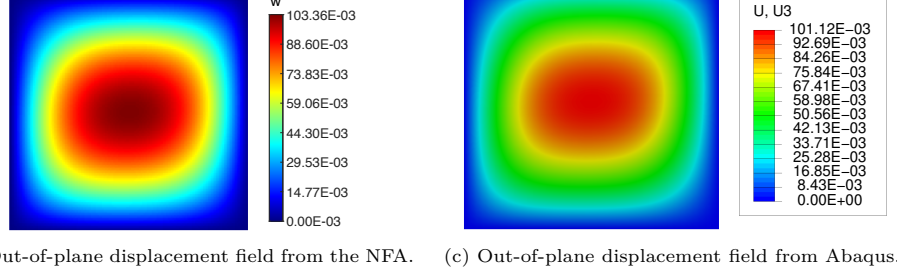

(b) Out-of-plane displacement field from the NFA. (c) Out-of-plane displacement field from Abaqus.

Figure 2.15: Postbuckling response and displacement fields: $[(45/90/-45/90)_2]_s$, $u_0/v_0 = 1/0$.

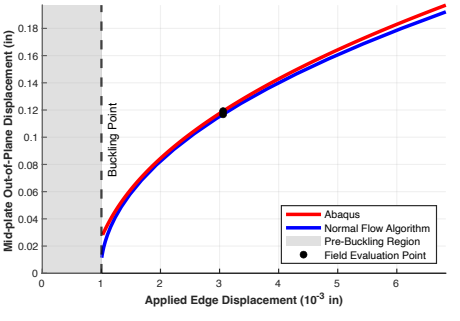

(a) Mid-plate out-of-plane displacement response under applied edge displacement.

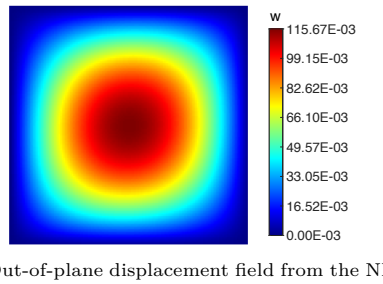

(b) Out-of-plane displacement field from the NFA.

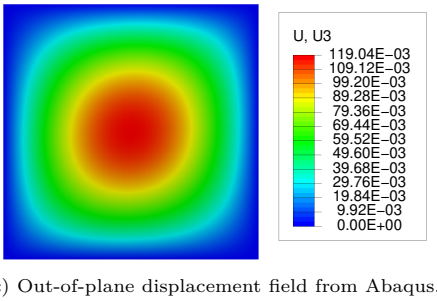

(c) Out-of-plane displacement field from Abaqus.

Figure 2.16: Postbuckling response and displacement fields: Laminate $[(45/-45)_4]_s$, $u_0/v_0 = 1/1$.

3

Beam-like models for the post-buckling behaviour of wingbox structures

Design and optimisation of wing structures are often constrained by buckling, even though thin-walled components, particularly stiffened panels, retain significant load-carrying capacity beyond their initial buckling point. Enabling the design for a safe use of this post-buckling regime requires a computationally efficient methodology that can be integrated into design and optimisation processes. This work provides a representation of one or more post-buckled wingbox regions through the stiffness matrix of a one-dimensional beam model. The approach is motivated by the observation that high-aspect-ratio wings exhibit global deformation patterns that closely resemble beam modes. The three-dimensional wingbox is mapped onto a one-dimensional representation using a cross-section modeller, while the reduction in stiffness induced by panel buckling is estimated using a semi-analytical post-buckling method and incorporated into the cross-sectional stiffness. This leads to a computationally efficient formulation suitable for repeated evaluations within design and optimisation loops. Results for several wingbox configurations show that the predicted buckling loads and post-buckling trends are in good agreement with Abaqus simulations in the early post-buckling regime. The Abaqus response becomes more compliant once local sagging and area reduction occur, which are not yet captured by the current model. Nevertheless, the proposed methodology accurately predicts the overall post-buckling behaviour within the range relevant for design, where wings are not expected to operate deeply into the post-buckling regime.

This chapter has been published as: M. H. Elalfy, R. De Breuker, and S. G. P. Castro, "Beam-like models for the post-buckling behaviour of wingbox structures," *engrXiv* preprint, 2026. doi:10.31224/8199

3.1. INTRODUCTION

Aerospace structures are typically thin-walled and lightweight, making it critical to strike a balance between structural weight and failure limits. In many designs, buckling is treated as a failure limit, as it can coincide with final failure, such as in single load-path critical structures. However, significant load-carrying capacity may still exist after buckling and before final failure, particularly for plate-like components (Kassapoglou, 2010, NASA, 1971). Experimental and theoretical studies further demonstrate that thin plates can follow a stable post-buckling deformation path and sustain increasing loads well beyond the buckling point before ultimate failure occurs (Muc et al., 2018, Roman and Pocheau, 2002). Stiffened plates, in particular, are known to sustain increasing loads in the post-buckling regime, with numerous experimental studies showing that local skin buckling occurs well before collapse and that the ultimate failure load can significantly exceed the initial buckling load (Falzon et al., 2000, Zimmermann et al., 2006, Murphy et al., 2005, Zhang et al., 2024). Recognising this behaviour has motivated a shift in aerospace structural design philosophy, in which the post-buckling regime is intentionally exploited to improve structural efficiency, allowing controlled post-buckling under ultimate load conditions rather than treating buckling as a strict failure limit (Rohwer and Degenhardt, 2007, Degenhardt et al., 2014).

The literature shows that buckling often emerges as the first active constraint in wing design and optimisation. The buckling response was used as a constraint for sizing a flexible aircraft in a nonlinear aeroelastic framework developed by Cesnik and Su (2005). Oliveri et al. (2018) designed a wingbox demonstrator with variable angle tow, in which buckling of the skin was only considered at the maximum design load. Kenway et al. (2014) used the NASA Common Research Model (CRM) in an optimisation study where buckling was a limiting constraint for the upper skin. Stodieck et al. (2017) used buckling as an optimisation constraint in their work. A multilevel aeroelastic tailoring framework developed by Othman et al. (2019), aimed to minimise the weight of a wing box by imposing buckling as one of the constraints. Sodja et al. (2018) aimed to minimise structural mass while considering multiple constraints including cruise shape, control effectiveness, maximum strain, and buckling. They compared a tailored composite wing design to a reference design, and for both designs, buckling was an active constraint.

Operating beyond initial buckling can enable further use of the unexploited load-carrying capacity of structural components, potentially leading to lighter-weight structural designs. To achieve this in practice, it is essential to incorporate post-buckling behaviour through a computationally efficient approach that is suitable for use within design and optimisation frameworks. Even the inclusion of buckling constraints alone can significantly increase the computational cost of structural optimisation, limiting scalability in practical design studies (Engelstad et al., 2025). When nonlinear post-buckling analysis is coupled directly with optimisation schemes, the need for repeated nonlinear equilibrium and stability evaluations leads to prohibitive computational cost, making such approaches impractical for use within design and optimisation frameworks (Bisagni and Lanzi, 2002, Mitrotta et al., 2025, Hu et al., 2025). Accordingly, existing optimisation approaches typically rely on reduced-

order initial post-buckling formulations, such as asymptotic Koiter-based methods, or surrogate models to alleviate the computational cost of full nonlinear analyses (Henrichsen et al., 2016, Bisagni and Lanzi, 2002).

The limitations of high-fidelity nonlinear post-buckling analyses and the reliance on reduced-order approximations motivate the need for alternative modelling strategies that are computationally efficient while remaining suitable for wing-level structural analysis. For slender wing structures, such strategies naturally involve reduced-order structural representations capable of capturing the dominant global response while accounting for local effects in an averaged sense. Beam-based models therefore provide a natural framework for incorporating post-buckling effects at the wingbox level within a computationally efficient formulation. Beam formulations have been developed in the literature as reduced-order representations for slender structural components such as wings, forming a hierarchy of models with increasing kinematic richness. Classical Euler–Bernoulli and Timoshenko beam theories constitute lower-order members of this hierarchy, while refined beam formulations introduce enriched cross-sectional kinematics to capture shear deformation, warping, and other local effects (Carrera and Giunta, 2010, Carrera et al., 2015). Within this hierarchical setting, the Carrera Unified Formulation (CUF) provides a general framework for generating beam theories of arbitrary order, with classical models recovered as special cases and higher-order expansions enabling an increasingly detailed representation of three-dimensional structural behaviour (Carrera and Giunta, 2010, Carrera et al., 2017). The enhanced fidelity offered by such higher-order beam models has been shown to improve the prediction of cross-sectional deformation and stress distributions in thin-walled and non-classical geometries, albeit at the cost of a rapidly increasing number of degrees of freedom as the kinematic order is enriched (Carrera et al., 2014, 2017). In contrast, lower-order beam descriptions, particularly Timoshenko-type formulations, retain the dominant global bending, shear, and torsional response without explicitly enriching the kinematic field, and therefore remain attractive within the broader hierarchy of beam models (Carrera et al., 2015, Yu et al., 2012). An alternative means of incorporating complex cross-sectional behaviour within such reduced-order beam models is provided by cross-sectional pre-integration techniques, in which detailed two-dimensional analyses are used to compute generalised stiffness matrices employed in one-dimensional beam formulations (Yu et al., 2012, Feil et al., 2020). These beam-based approaches inherently rely on beam-like kinematic assumptions and typically assume constant or slowly varying cross-sections along the span, which delineates their range of applicability (Carrera et al., 2017, Feil et al., 2020).

The main contribution of the present study is a methodology to obtain the stiffness matrix of one-dimensional Timoshenko beam elements with locally post-buckled regions. It is herein observed that the proposed methodology correlates well with the detailed shell-based model into the post-buckling regime, until cross-sectional sagging develops. Four isotropic rectangular wingbox cases are used in this investigation, consisting of a lower and higher aspect ratio, respectively 10 and 20, each having a thinner or thicker spar. The proposed nonlinear algorithm evaluates the local reduction in stiffness occurring upon buckling using a perturbation-based

semi-analytical approach (Elalfy et al., 2026) and is integrated into the process, leading to an efficient approach that suits design and optimisation purposes.

The chapter is organised as follows: Section 3.2 outlines the proposed methodology, including the one-dimensional representation of a three-dimensional wingbox, the semi-analytical post-buckling formulation, and the interaction between different components. A verification case is also presented. Section 3.3 presents and discusses the results, including the limitations of the proposed approach. Finally, Section 3.4 summarises the main conclusions.

3.2. METHODOLOGY

The three-dimensional response is reduced to a one-dimensional Timoshenko beam description through cross-sectional stiffness properties, as illustrated in Figure 3.1. Local post-buckling effects of wing panels are incorporated in an averaged sense by modifying the effective cross-sectional stiffness following buckling, rather than resolving local nonlinear deformation fields explicitly. The semi-analytical post-buckling formulation proposed by Elalfy et al. (2026) estimates the stiffness reduction associated with local panel buckling and integrates this effect into the beam-level representation, enabling efficient analysis suitable for design and optimisation applications.

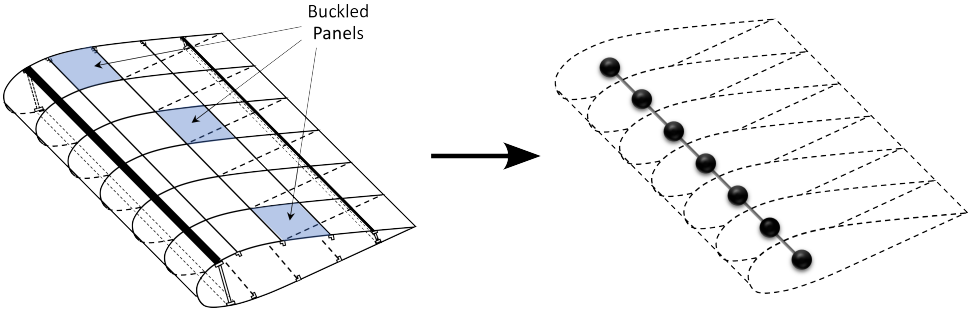

Figure 3.1: One-dimensional representation of three-dimensional buckled wingbox.

3.2.1. CROSS-SECTIONAL STIFFNESS MATRIX FORMULATION

As proposed by Ferede and Abdalla (2014), the stiffness properties of composite beam-like structures can be reduced to a 6×6 stiffness matrix, compatible with first-order shear deformable Timoshenko beam elements. In the present work, a mathematically consistent formulation of the cross-sectional stiffness matrix is developed, starting from a mixed displacement-stress representation and yielding a closed-form 6×6 Timoshenko stiffness matrix $\mathbf{K}_{\text{cs}}$. Starting from the cross-sectional kinematic description, the strain field $\boldsymbol{\varepsilon}$ is expressed in compact form in terms of the displacement vector $\boldsymbol{q}$ and its derivative with respect to the beam coordinate $\boldsymbol{q'}$:

$$\boldsymbol{\varepsilon} = \mathbf{B_0}\, \boldsymbol{q} + \mathbf{B_1}\, \boldsymbol{q'}, \tag{3.1}$$

where $\mathbf{B_0}$ and $\mathbf{B_1}$ are kinematic operators. This leads to the following expression for the strain energy per unit depth:

$$U = \frac{1}{2} \int_A \left(\mathbf{B_0}\boldsymbol{q} + \mathbf{B_1}\boldsymbol{q'}\right)^\top \mathbf{C} \left(\mathbf{B_0}\boldsymbol{q} + \mathbf{B_1}\boldsymbol{q'}\right) \, dA, \tag{3.2}$$

where $\mathbf{C}$ is the constitutive matrix and A is the cross-sectional area.

By applying a variational principle to the strain energy functional and defining the Lagrangian functional accordingly, the Euler-Lagrange equations introduce the generalised momenta $\boldsymbol{p}$, leading to a first-order system written as:

$$\boldsymbol{x'} = \mathcal{A}\,\boldsymbol{x}, \qquad \boldsymbol{x} = \begin{bmatrix} \boldsymbol{q} \\ \boldsymbol{p} \end{bmatrix}, \tag{3.3}$$

where $\mathcal{A}$ is the system matrix and the generalised momenta $\boldsymbol{p}$ correspond to the tractions acting over the cross-section.

According to Saint–Venant's principle, only stress states that persist away from the load-introduction region are physically admissible. In the present formulation, these persistent solutions are obtained by considering the invariant subspace associated with the zero eigenvalue:

$$\mathcal{A}\,\boldsymbol{\phi} = \mathbf{0}, \tag{3.4}$$

where $\boldsymbol{\phi}$ is a vector in the null space of $\mathcal{A}$.

Since the system matrix $\mathcal{A}$ is non-normal, the eigenvectors associated with the zero eigenvalue do not, in general, span the full invariant subspace. As a result, the Saint–Venant solution space is complemented by generalised eigenvectors $\boldsymbol{\psi}$, which are defined recursively through:

$$\mathcal{A}\,\boldsymbol{\psi} = \boldsymbol{\phi}. \tag{3.5}$$

A solution of the first-order system associated with the zero eigenvalue can be expressed as a linear combination of the corresponding eigenvectors and generalised eigenvectors. Accordingly, the state vector $\boldsymbol{x}$ is expressed as a linear combination of the persistent Saint–Venant modes, with $\boldsymbol{c}$ as the corresponding coefficients. Using this representation, the generalised momenta $\boldsymbol{p}$ can be expressed in terms of the same coefficients, as derived in Appendix 3.A. As a result, the force and moment resultants over the cross-section can be written as:

$$\boldsymbol{f} = \mathbf{\Phi_1}\,\boldsymbol{c}. \tag{3.6}$$

An energy-consistent definition of the cross-sectional stiffness then follows as:

$$\mathbf{K}_{\text{cs}} = \mathbf{\Phi_1}\mathbf{\Phi_3^{-1}}\mathbf{\Phi_1^\top}, \tag{3.7}$$

where $\mathbf{\Phi_1}$ and $\mathbf{\Phi_3}$ are matrices constructed from the Saint–Venant modes and the constitutive matrix, as defined in Appendix 3.A. The complete derivation of the cross-sectional stiffness matrix is provided in Appendix 3.A, where a self-contained and fully traceable formulation is developed. Appendix 3.B summarises the rigid-body relations repeatedly used to simplify the derivation.

3.2.2. SEMI-ANALYTICAL PERTURBATION-BASED LOCAL POST-BUCKLING

A perturbation-based analysis (Elalfy et al., 2026) is used to estimate the post-buckling stiffness of buckled panels over the cross-section, such as those illustrated in Figure 3.1. The methodology is developed using a semi-analytical approach based on the Rayleigh–Ritz method and the perturbation formulation originally proposed by Seresta et al. (2008). Hierarchical polynomials are employed to approximate the displacement field, improving computational efficiency by eliminating the need for numerical integration (Elalfy et al., 2026). Furthermore, they offer enhanced flexibility for modelling different boundary conditions, unlike trigonometric functions, which are inherently limited to representing simply supported cases.

The plate displacements within this framework are approximated using a Rayleigh–Ritz expansion of the form

$$\begin{aligned} w(x,y) &= \sum_{i=2}^{N} a_i\, \phi_i^w \\ u(x,y) &= -\lambda e_{x0}\, x - \lambda \frac{g_{xy0}}{2}\, y + \sum_{i=2}^{N} b_i\, \phi_i^u \\ v(x,y) &= -\lambda e_{y0}\, y - \lambda \frac{g_{xy0}}{2}\, x + \sum_{i=2}^{N} c_i\, \phi_i^v, \end{aligned} \tag{3.8}$$

where $w(x,y)$ denotes the out-of-plane displacement, $u(x,y)$ and $v(x,y)$ are the in-plane displacements. The coefficients a_i, b_i, and c_i are Ritz parameters, with ϕ_i^w, ϕ_i^u, and ϕ_i^v being the corresponding shape functions. The quantities e_{x0}, e_{y0}, and g_{xy0} are the prescribed uniform in-plane edge strains in the x- and y-directions and the in-plane shear strain, respectively, while λ is a load parameter scaling these applied strains.

Based on the assumed displacement field, the governing equations are obtained by formulating the total potential energy as follows:

$$\begin{aligned} \Pi(u,v,w) = \frac{1}{2}\int_0^A \int_0^B \Big[& A_{11}\left(\epsilon_x^0\right)^2 + 2A_{12}\epsilon_x^0\epsilon_y^0 + A_{22}\left(\epsilon_y^0\right)^2 + A_{66}\left(\gamma_{xy}^0\right)^2 \\ & + D_{11}\kappa_x^2 + 2D_{12}\kappa_x\kappa_y + 2D_{16}\kappa_x\kappa_{xy} + 2D_{26}\kappa_y\kappa_{xy} + D_{22}\kappa_y^2 + D_{66}\kappa_{xy}^2 \Big]\, dydx, \end{aligned} \tag{3.9}$$

where ϵ_x^0, ϵ_y^0, and γ_{xy}^0 denote the mid-plane membrane strains, κ_x, κ_y, and κ_{xy} are the corresponding plate curvatures, and A_{ij} and D_{ij} represent the in-plane and bending stiffness coefficients, respectively.

Minimisation of the total potential energy with respect to the Ritz coefficients yields a set of nonlinear equilibrium equations. Following the perturbation approach adopted in (Seresta et al., 2008, Elalfy et al., 2026), the applied edge strains and the transverse Ritz coefficients are expanded about the buckling point as

$$\begin{aligned} e_{x0} &= e_{x_0}^{(0)} + \epsilon^2 e_{x_0}^{(2)} + \cdots & e_{y0} &= e_{y_0}^{(0)} + \epsilon^2 e_{y_0}^{(2)} + \cdots \\ g_{xy0} &= g_{xy_0}^{(0)} + \epsilon^2 g_{xy_0}^{(2)} + \cdots & a_i &= \epsilon a_i^{(1)} + \epsilon^2 a_i^{(2)} + \cdots . \end{aligned} \tag{3.10}$$

Here, (0) and (2) denote the prebuckling and second-order postbuckling contributions, while $a_i^{(1)}$ represents the linear buckling eigenvector. The post-buckled in-plane stiffnesses: A_{11}^{PB}, A_{12}^{PB}, A_{21}^{PB}, A_{22}^{PB} and A_{66}^{PB}; are then obtained by relating the second-order perturbed membrane resultants: $\bar{N}_x^{(2)}$, $\bar{N}_y^{(2)}$ and $\bar{N}_{xy}^{(2)}$; to the corresponding second-order edge strains $\epsilon_{x0}^{(2)}$, $\epsilon_{y0}^{(2)}$ and $g_{xy0}^{(2)}$, as shown in Equation 3.11. The definitions of these second-order parameters are detailed in Elalfy et al. (2026).

$$A_{11}^{\mathrm{PB}} = \frac{\bar{N}_x^{(2)}}{e_{x0}^{(2)}}, \quad A_{12}^{\mathrm{PB}} = \frac{\bar{N}_x^{(2)}}{e_{y0}^{(2)}}, \quad A_{21}^{\mathrm{PB}} = \frac{\bar{N}_y^{(2)}}{e_{x0}^{(2)}}, \quad A_{22}^{\mathrm{PB}} = \frac{\bar{N}_y^{(2)}}{e_{y0}^{(2)}}, \quad A_{66}^{\mathrm{PB}} = \frac{\bar{N}_{xy}^{(2)}}{g_{xy0}^{(2)}}. \tag{3.11}$$

The boundary conditions of stiffened panels within a wingbox structure cannot be accurately modelled using ideal boundary conditions. In practice, panel edges are neither perfectly simply supported nor clamped and have been modelled in the literature using intermediate boundary conditions to better represent the actual structural constraints (Houston et al., 2017, Zhang and Bisagni, 2021). Differences in stiffness between the skin, ribs, stiffeners, and spars affect the degree of allowed rotation along the panel edges. For example, a very stiff spar may significantly restrict rotation, causing the panel to behave nearly as if it were clamped, although not fully clamped. To account for this, the present study investigates two limiting cases: simply supported edges, giving a lower and therefore conservative bound on the buckling load, and clamped edges, giving an upper bound. The use of hierarchical polynomials allows this boundary condition variation to be implemented efficiently within the same modelling framework (Elalfy et al., 2026).

In the context of the present work, a key output of the post-buckling formulation is the post-buckled in-plane stiffness matrix, denoted $\mathbf{A}_{\mathrm{PB}}$. This matrix captures the stiffness reduction of the plate after buckling, and its elements are the post-buckled in-plane stiffnesses of Equation 3.11. It will later play a central role in modifying the cross-sectional constitutive matrix, $\mathbf{C}$ of Equation 3.2 as shown in the next section.

3.2.3. Algorithm for Post-buckling Representation in Beam Models

As schematically shown in Figure 3.2, the three main components involved in the proposed algorithm are: cross-section modeller, perturbation-based post-buckling analysis, and co-rotational nonlinear beam solver. The proposed methodology starts by feeding the geometry and material properties into the cross-section modeller to calculate the 6×6 Timoshenko stiffness matrices $\mathbf{K}_{\mathrm{cs}}$ at all node locations. These stiffness matrices are the inputs for the co-rotational nonlinear beam solver, which calculates forces and displacements at each node. Normally, when no local post-buckling is accounted for, the nonlinear beam solver keeps iterating step-by-step until the full applied load is attained.

To include post-buckling, the proposed workflow requires that all panels must be checked for buckling, at each converged step of the Newton–Raphson scheme. The converged forces and displacements are fed back into the cross-section modeller, which in turn retrieves the stress and strain distribution throughout all defined

cross-sections. The retrieved stress distribution is then used by the semi-analytical perturbation-based post-buckling analysis to check if buckling occurs. When no panel buckles, the Newton–Raphson proceeds with the next load increment. However, when buckling occurs at any region over the defined cross-sections, the nonlinear beam solver steps back to a load level and corresponding displacement state associated with the lowest buckling eigenvalue, considering all panel pockets in all defined cross-sections over the wingbox. In fact, this load level corresponds to the first local buckling load of the wing. At this point, the cross-section modeller reevaluates the stress distribution at the critical load point. Given the stresses at the critical load point and the critical panel dimensions, the perturbation-based post-buckling analysis calculates the post-buckled stiffness of the buckled regions ($\mathbf{A}_{\mathrm{PB}}$ of Equation 3.11). The updated stiffness of the buckled panel is then accounted for in the cross-section modeller, with a new point on the load-displacement curve obtained by the nonlinear beam solver. This procedure is repeated iteratively, identifying subsequent buckled panels, updating their stiffness, and reflecting these changes in the cross-section modeller accordingly.

The present nonlinear finite element solver uses a co-rotational approach in which small elastic deformations are superimposed on beam rigid rotations (De Breuker, 2011). De Breuker (2011) implemented the beam solver using the Newton–Raphson root-finding algorithm, in which the load-displacement curve is obtained in a stepwise manner.

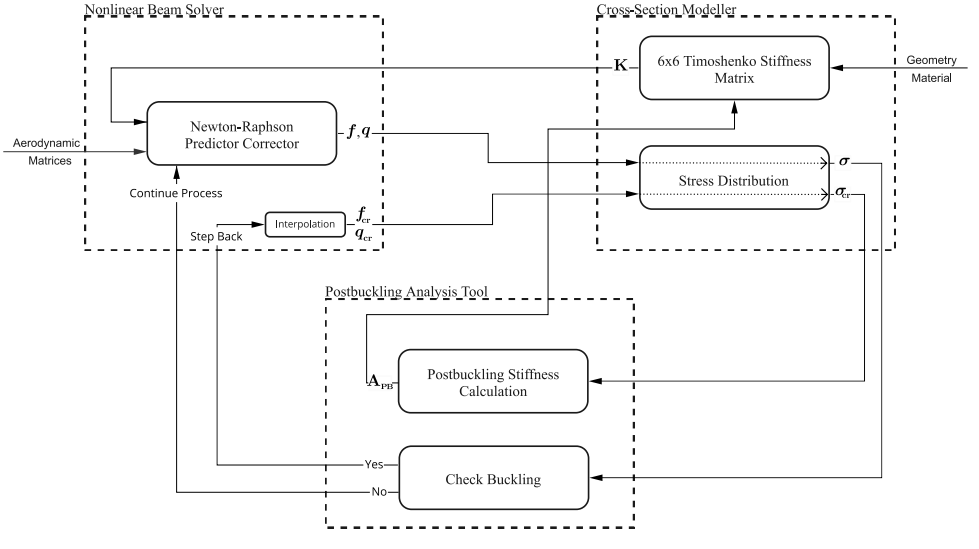

Figure 3.2: Workflow of representing post-buckling using low-fidelity model.

3.2.4. HIGH-FIDELITY SHELL ELEMENT REFERENCE MODEL

A higher-fidelity finite element model based on shell elements is implemented in Abaqus (Dassault Systèmes, 2022) to verify both the onset of local buckling, and the

global structural response of the wingbox following the post-buckling of individual panels. This model serves as a reference for assessing the accuracy and limitations of the proposed approach, particularly for capturing the stiffness degradation due to subsequent local buckling events, and the overall load-displacement behaviour of the wing.

The wingbox geometry is created using Engineering Sketch Pad (ESP) (MIT Aerospace Computational Design Laboratory, 2023, Rahman et al., 2023), enabling easy parametric modifications. As shown in Figure 3.3, the wingbox is a non-tapered rectangular box, with its dimensions and rib distribution inspired by the work of Francois et al. (2015). The geometry is exported to a STEP file using the pyCAPS Python library (Kennedy and Martins, 2020) and subsequently imported into Abaqus for meshing and analysis. The following variables define the wing geometry: chord W, height H, half-span L, thickness for the skin t_{skin}, and spar t_{spar}.

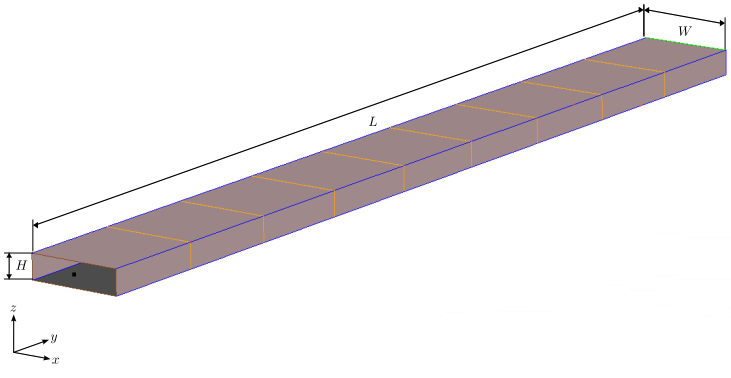

Figure 3.3: Wingbox CAD in Engineering Sketch Pad.

Each case is defined by a rectangular, untapered wingbox geometry with a fixed cross-sectional shape. The span is divided into nine bays using evenly spaced ribs, as shown in Figure 3.3. Table 3.1 summarises the key properties for the cases presented in this section, where two high-aspect-ratio ("high-AR") and two low-aspect-ratio ("low-AR") cases are investigated. Two spar thicknesses are investigated, $t_{spar} = 1$ mm and $t_{spar} = 5$ mm, referred to hereafter as the "t1" and "t5" cases. All structural panels are modelled using homogeneous shell sections and meshed with square S4R elements (4-node, reduced integration). A linear elastic, homogeneous material with isotropic in-plane properties is assumed, with the corresponding parameters summarised in Table 3.2. For each case, the mesh resolution is selected to ensure sufficient element density for capturing all relevant local buckling modes and post-buckling deformations.

The wingbox is clamped at the root, and a concentrated vertical force is applied at the tip to induce buckling and drive the nonlinear response. First, a linear buckling analysis is performed to identify critical loads and mode shapes. A subsequent static Riks analysis is then carried out around the buckling point to capture the

post-buckling behaviour of the structure. The proposed framework is implemented in the in-house wingbox analysis and optimisation tool Proteus (De Breuker, 2011). The same verification cases are also analysed using this framework.

Table 3.1: Geometric parameters for each wingbox case.

Case	W [mm]	L [mm]	H [mm]	# Ribs	t_{skin} [mm]	t_{spar} [mm]
High-AR-t5	50.5	1010.0	12.12	8	1.0	5.0
High-AR-t1	50.5	1010.0	12.12	8	1.0	1.0
Low-AR-t5	50.5	502.0	12.12	8	1.0	5.0
Low-AR-t1	50.5	502.0	12.12	8	1.0	1.0

Table 3.2: Isotropic material properties (Rahman et al., 2023).

E [GPa]	G [GPa]	ν	ρ [kg/m^3]
73.00	27.44	0.33	2.795×10^3

3.3. Results and Discussion

The proposed methodology is assessed against Abaqus reference results across a set of wingbox configurations. First, the predicted linear buckling eigenvalues are compared against Abaqus results. The nonlinear post-buckling load-displacement response is then assessed against Abaqus Riks analyses. Finally, the validity of the beam-level representation is examined in the context of cross-sectional deformation.

3.3.1. Buckling Eigenvalue Verification

A linear buckling analysis is performed for each case using Abaqus as the first verification step. The results show that the first few buckling modes are all dominated by local buckling behaviour, with deformation concentrated in individual skin panels between ribs. No global bending or torsional modes are observed among the lowest modes, directly supporting the core assumption underlying the semi-analytical approach proposed in Elalfy et al. (2026), which also forms the basis of the current work.

Two boundary condition variants for the local panel model are considered in the comparison: one assuming simply supported (SS) panels and the other assuming fully clamped (C) panels. Both are evaluated against Abaqus linear buckling eigenvalue results, as summarised in Table 3.3. For all cases, the predictions from Abaqus lie between simply supported and clamped. For the Low-AR-t5 and High-AR-t5 cases, the clamped results are significantly more accurate. This behaviour is consistent with the structural configuration, because the "-t5" cases have the spar thickness high compared to the skin, increasing the rotational restraint at the panel edges and effectively shifting the response toward the clamped boundary condition. However, for cases Low-AR-t1 and High-AR-t1, with the spars having the same

thickness as the skin, Abaqus results are further away from the clamped conditions, indicating that the skin is less clamped by the spar, nevertheless far from being simply supported.

Table 3.3: Comparison of first eigenvalues from Abaqus and proposed local buckling model with different boundary conditions.

Case	Abaqus [N]	Present model (SS) [N]	Present model (C) [N]
High-AR-t5	173.11	92.17	178.74
High-AR-t1	118.81	71.20	138.00
Low-AR-t5	442.17	182.82	454.61
Low-AR-t1	294.48	142.02	353.65

3.3.2. Nonlinear Post-buckling Load-Displacement Response

A nonlinear Riks analysis is conducted in Abaqus to capture the global nonlinear load-displacement response of the wingbox beyond buckling. These results serve as a reference for assessing the predictions from the proposed beam model, which iteratively updates the stiffness of buckled panels based on the local response. For each wingbox of Table 3.1, two loading scenarios are considered: one without and one with a follower tip force.

To support the interpretation of the nonlinear results that follow, a set of spanwise monitoring cross-sections was defined, as shown in Figure 3.4. The node sets labelled (CS 1–CS 9) are placed at the mid-bay between ribs, while (CS 10–CS 18) and (CS 20–CS 28) correspond to the first- and third-quarter positions within each bay, respectively. These cross-sections provide a consistent way to examine how the geometry evolves during post-buckling, particularly in regions where the skin is most susceptible to local deformation. The tracked quantities include the deformation shape of each section and its resulting enclosed area, which will later be used to assess cross-sectional changes along the span.

Figures 3.5–3.12 present the nonlinear response for each case, showing the Abaqus Riks results together with the predictions from the proposed model under simply supported and clamped boundary conditions. The linear buckling eigenvalues from Abaqus are shown as markers on the load-displacement curves for the cases without a follower force. Deformed wings are shown at different tip-load levels, with contours of the minimum in-plane strain field highlighting regions of compressive and tensile strain during the nonlinear response, thereby making the onset and progression of buckling clearly visible. Additionally, the evolution of the cross-sectional area at selected locations is shown, along with the deformed cross-section shapes directly extracted from the finite element models. The representative cross-sections plotted for each case are selected based on the number of half-waves forming within each bay. This number depends on the skin panel aspect ratio and the skin and spar thicknesses and indicates where the largest local deformations occur. Together, these components allow the geometric changes along the span to be tracked, pro-

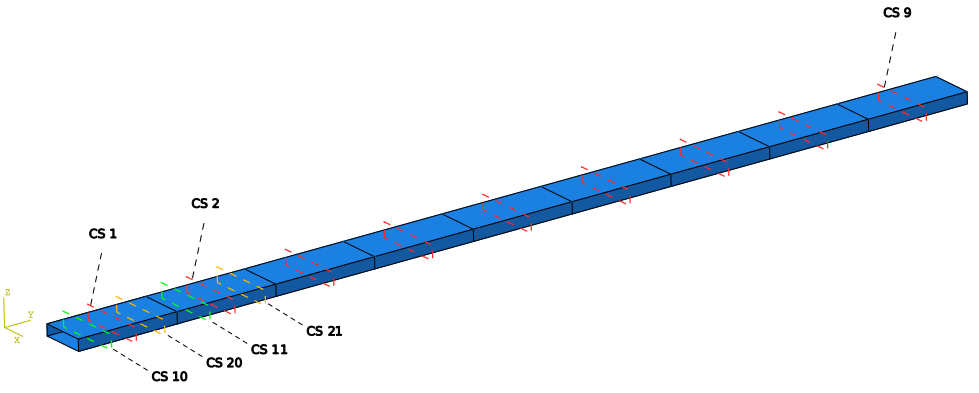

Figure 3.4: Spanwise cross-sectional locations along the wingbox.

viding a consistent basis for comparing the proposed beam models against Abaqus results.

For the high-aspect-ratio wings, Figures 3.5–3.8 show that post-buckling develops with two half-waves, such that the skin is more prominently sagging at the cross-section at one-quarter CS 10 and three-quarter CS 20 positions. For the low-aspect-ratio wings, sagging happens in the middle of the bay CS 1, meaning skins with only one half-wave post-buckling. The nonlinear load–displacement curves exhibit a similar trend from the initial loading stage through the early post-buckling regime, with the Abaqus response lying between the simply supported and clamped cases. Deviations emerging at higher load levels are discussed in the following section.

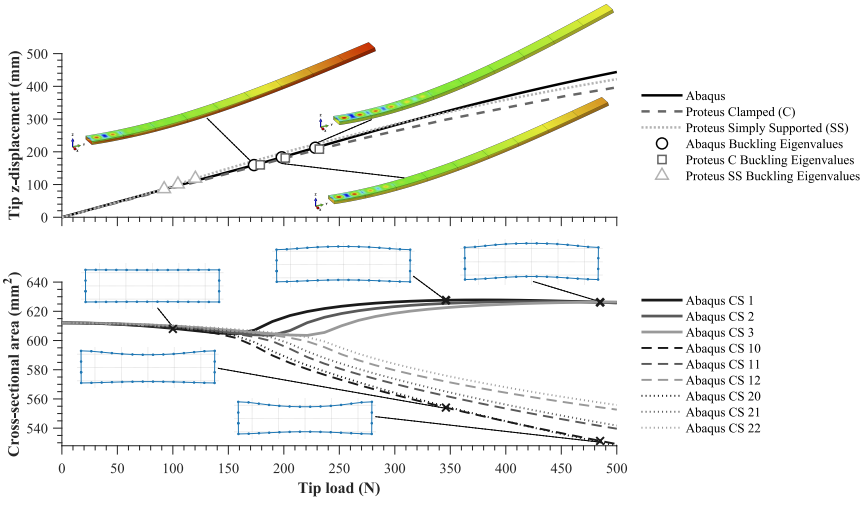

Figure 3.5: High-AR-t5 without follower force.

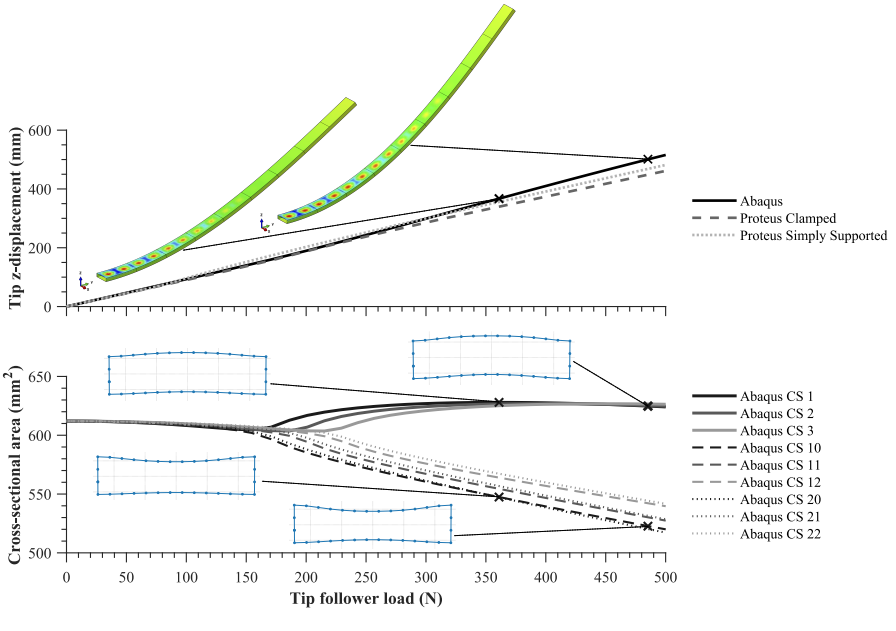

Figure 3.6: High-AR-t5 with follower force.

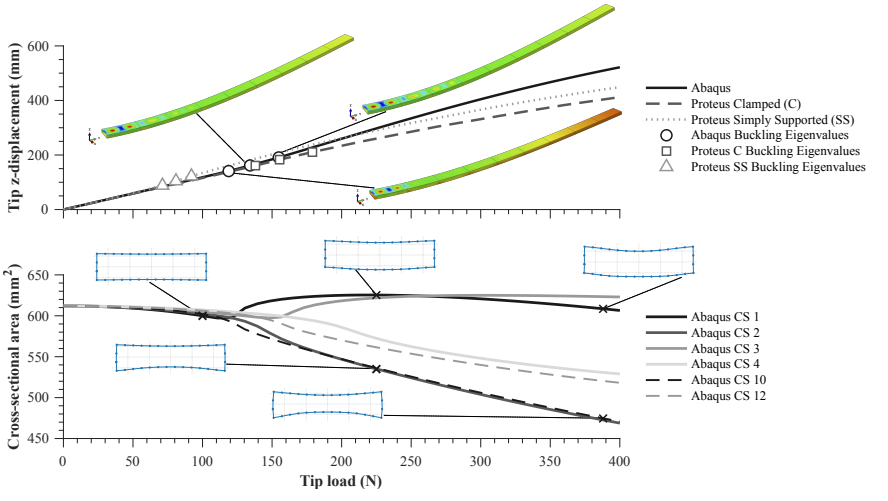

Figure 3.7: High-AR-t1 without follower force.

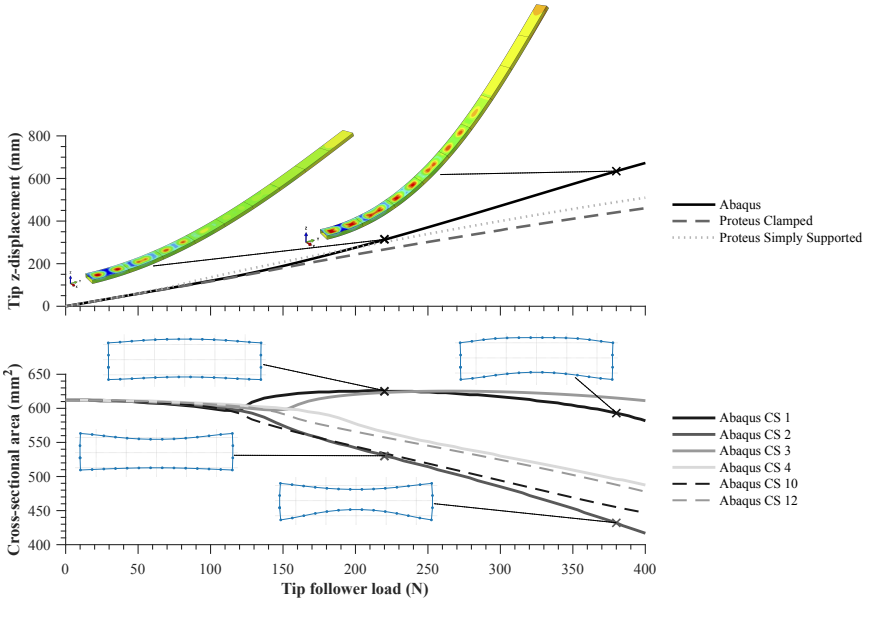

Figure 3.8: High-AR-t1 with follower force.

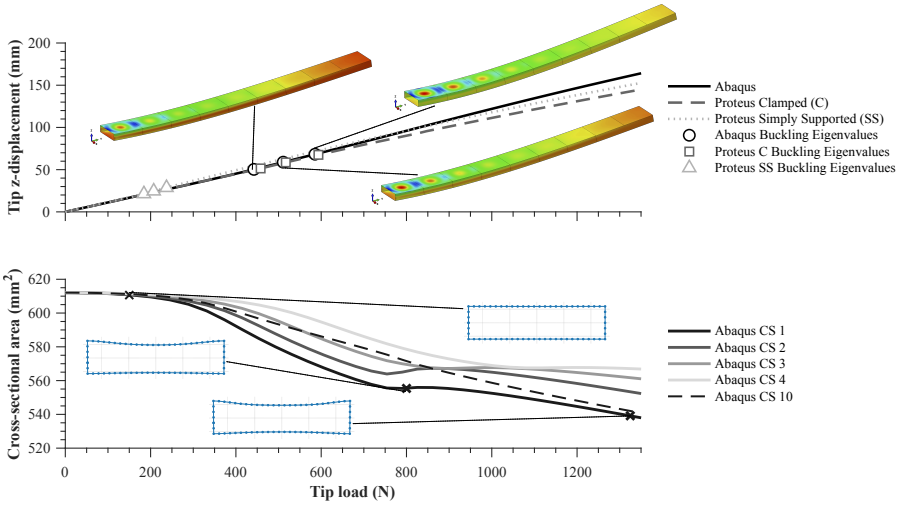

Figure 3.9: Low-AR-t5 without follower force.

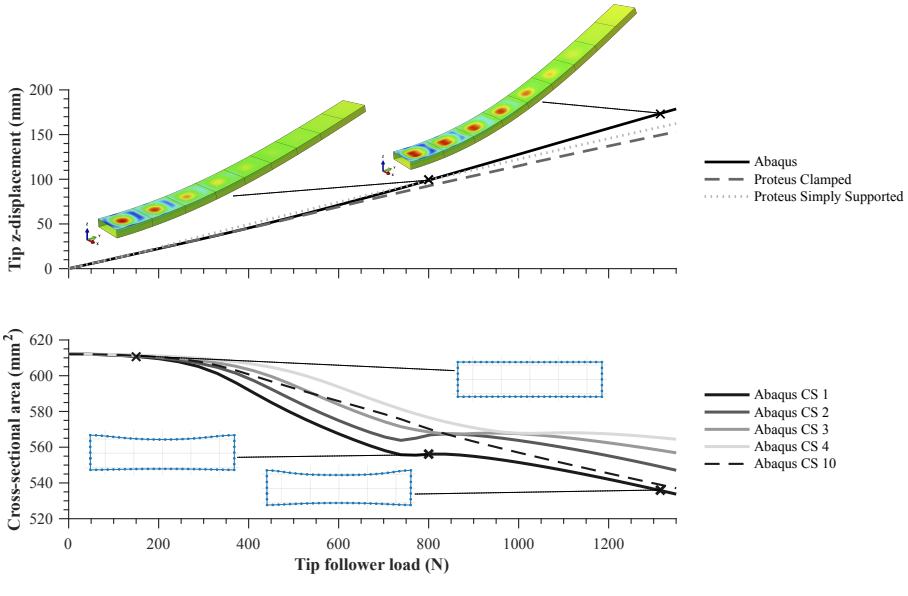

Figure 3.10: Low-AR-t5 with follower force.

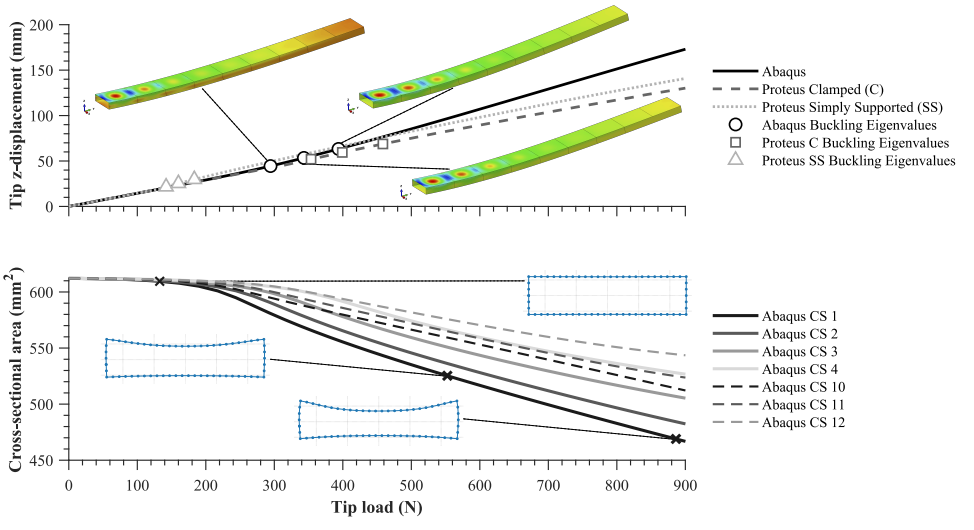

Figure 3.11: Low-AR-t1 without follower force.

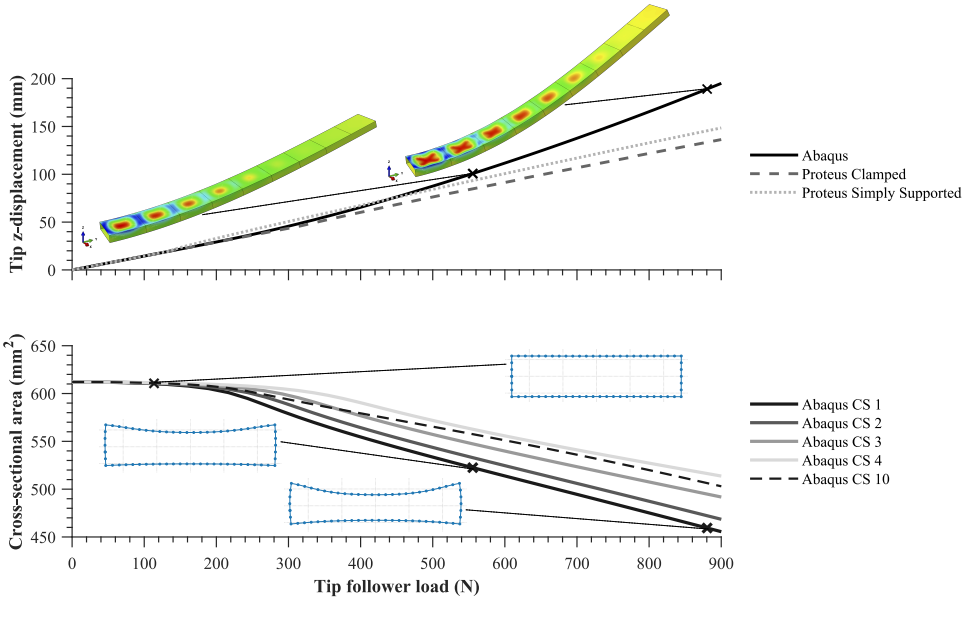

Figure 3.12: Low-AR-t1 with follower force.

3.3.3. Validity of Timoshenko's beam models and Brazier deformation

For all wingboxes, as shown in Figures 3.5–3.12, the post-buckling prediction capability of the proposed beam models begins to deviate from Abaqus when the cross-sectional area starts to change, indicating that the prediction capability is driven by changes in cross-section shape that are not accounted for in the present formulation. Medeiros et al. (2021) also observed that beam models become inaccurate when changes in cross-section are sufficiently high to produce changes in the overall bending stiffness of the beam.

In the high-aspect ratio results with a thicker spar, shown in Figures 3.5 and 3.6, the deformation patterns between ribs show that buckling occurs with two half-waves within each bay. As a result, the first- (CS 10–CS 12) and third-quarter (CS 20–CS 22) cross-sections exhibit a reduction in enclosed area and a clear development of a sagging-type of deformation, where the skin panels deflect inward. In contrast, the mid-bay section (CS 1–CS 3) shows no noticeable sagging, and its enclosed area increases slightly.

The local reduction in enclosed area reflects inward deflection of the skins, which reduces the effective bending height of the section. This reduction produces a Brazier-type softening that is not captured by the current modelling approach. Consequently, Abaqus response becomes more compliant at higher load levels, leading to larger deflections in the finite element solution.

This behaviour is consistent with the findings of Jiang and Yu (2024), who showed that rectangular thin-walled sections subjected to bending do not ovalize in the classical circular-tube sense but instead develop sagging deformation, which they identify as a manifestation of the generalised Brazier effect. Cecchini and Weaver (2005) showed that thin-walled airfoil and box sections undergo inward crushing of their walls under bending, which reduces the effective second moment of area and produces a Brazier-type loss of stiffness (Brazier, 1927).

Across the remaining cases, similar trends are observed with variations that reflect the changes in spar thickness, rib spacing, and panel aspect ratio. Reducing the spar thickness shifts the Abaqus buckling eigenvalues toward the simply supported prediction, although they generally remain closer to the clamped case as shown in Figures 3.7, 3.11. The onset and magnitude of area reduction strongly influence the post-buckling deviation. Cases with larger area loss and clearer sagging deformation begin to diverge from the model earlier and show a greater mismatch. This effect is amplified under follower forces, where the increased bending moment accelerates the geometric changes and causes the Abaqus response to diverge sooner as shown in Figures 3.8, 3.12. In addition, increasing the rib spacing makes the skin panels more susceptible to local deformation, which in turn increases the area reduction observed in the cross-sections and amplifies the discrepancy with the simplified model. Beyond the onset of significant area reduction, the simply supported and clamped predictions no longer bracket the response. The Abaqus tip displacement exceeds even the simply supported case, so a design relying on these predictions would underestimate deflection. The simply supported and clamped predictions remain reliable for the linear buckling load across all cases considered, as shown in Table 3.3, so the

onset of area reduction, rather than the boundary condition assumption, sets the effective limit of validity.

3.4. Conclusion

This work presented a computationally efficient approach for representing post-buckled regions within a one-dimensional beam model of a wingbox. By embedding the stiffness reduction of locally buckled panels into the cross-sectional stiffness matrix, the method provides a practical way to incorporate post-buckling effects within design and optimisation studies. The formulation combines a semi-analytical post-buckling model for individual panels with a cross-section modeller that maps the three-dimensional wingbox onto a one-dimensional beam representation.

Verification against Abaqus analyses showed that the methodology captures the onset and progression of buckling accurately, under both simply supported and clamped boundary conditions. The model reproduces the stiffness drop associated with panel buckling and follows the global post-buckling trend well. Deviations appear mainly when significant cross-sectional sagging develops – an effect not included in the present formulation – but the overall behaviour remains consistent with expectations for thin-walled wing structures. Within the preliminary design range, the method captures the essential post-buckling behaviour while remaining computationally efficient.

Future work will focus on applying the enhanced method within aeroelastic optimisation studies to enable a deeper exploration of structural efficiency beyond current design limits.

Bibliography

C. Bisagni and L. Lanzi. Post-buckling optimisation of composite stiffened panels using neural networks. *Composite Structures*, 58(2):237–247, 2002. ISSN 0263-8223. doi: https://doi.org/10.1016/S0263-8223(02)00053-3.

L. G. Brazier. On the flexure of thin cylindrical shells and other "thin" sections. *Proceedings of the Royal Society of London. Series A, Containing Papers of a Mathematical and Physical Character*, 116(773):104–114, 1927. ISSN 09501207. URL `http://www.jstor.org/stable/94717`.

E. Carrera and G. Giunta. Refined beam theories based on a unified formulation. *International Journal of Applied Mechanics*, 02(01):117–143, 2010. doi: 10.1142/S1758825110000500.

E. Carrera, A. Pagani, and F. Zangallo. Thin-walled beams subjected to load factors and non-structural masses. *International Journal of Mechanical Sciences*, 81:109–119, 2014. ISSN 0020-7403. doi: https://doi.org/10.1016/j.ijmecsci.2014.02.015.

E. Carrera, A. Pagani, M. Petrolo, and E. Zappino. Recent developments on refined theories for beams with applications. *Mechanical Engineering Reviews*, 2(2):14–00298–14–00298, 2015. doi: 10.1299/mer.14-00298.

E. Carrera, A. de Miguel, and A. Pagani. Hierarchical theories of structures based on legendre polynomial expansions with finite element applications. *International Journal of Mechanical Sciences*, 120:286–300, 2017. ISSN 0020-7403. doi: https://doi.org/10.1016/j.ijmecsci.2016.10.009.

L. S. Cecchini and P. M. Weaver. Brazier effect in multibay airfoil sections. *AIAA Journal*, 43(10):2252–2258, 2005. doi: 10.2514/1.11736.

C. E. Cesnik and W. Su. Nonlinear aeroelastic modeling and analysis of fully flexible aircraft. In *Collection of Technical Papers - AIAA/ASME/ASCE/AHS/ASC Structures, Structural Dynamics and Materials Conference*, volume 7, pages 4472–4498. American Institute of Aeronautics and Astronautics Inc., 2005. doi: 10.2514/6.2005-2169.

Dassault Systèmes. *ABAQUS 2022 Documentation*. Dassault Systèmes Simulia Corp., Providence, RI, USA, 2022.

R. De Breuker. *Energy-based Aeroelastic Analysis and Optimisation of Morphing Wings*. PhD thesis, Delft University of Technology, 2011.

R. Degenhardt, S. G. Castro, M. A. Arbelo, R. Zimmerman, R. Khakimova, and A. Kling. Future structural stability design for composite space and airframe structures. *Thin-Walled Structures*, 81:29–38, 2014. ISSN 0263-8231. doi: https://doi.org/10.1016/j.tws.2014.02.020.

M. H. Elalfy, R. De Breuker, and S. G. Castro. An efficient semi-analytical approach for postbuckling analysis of laminated composite plates with straight edges. *Thin-Walled Structures*, 222:114394, 2026. ISSN 0263-8231. doi: https://doi.org/10.1016/j.tws.2025.114394.

S. P. Engelstad, B. J. Burke, and G. J. Kennedy. Machine learning to improve buckling predictions for structural optimization of stiffened structures. *AIAA Journal*, page 1–16, Nov. 2025. ISSN 1533-385X. doi: 10.2514/1.j065925.

B. Falzon, K. Stevens, and G. Davies. Postbuckling behaviour of a blade-stiffened composite panel loaded in uniaxial compression. *Composites Part A: Applied Science and Manufacturing*, 31(5):459–468, 2000. ISSN 1359-835X. doi: https://doi.org/10.1016/S1359-835X(99)00085-8.

R. Feil, T. Pflumm, P. Bortolotti, and M. Morandini. A cross-sectional aeroelastic analysis and structural optimization tool for slender composite structures. *Composite Structures*, 253:112755, 2020. ISSN 0263-8223. doi: https://doi.org/10.1016/j.compstruct.2020.112755.

E. A. Ferede and M. M. Abdalla. Cross-sectional modelling of thin-walled composite beams. In *55th AIAA/ASMe/ASCE/AHS/SC Structures, Structural Dynamics, and Materials Conference*, 2014. doi: 10.2514/6.2014-0163.

G. Francois, J. E. Cooper, and P. M. Weaver. Aeroelastic tailoring using rib/spar orientations: Experimental investigation. In *56th AIAA/ASCE/AHS/ASC Structures, Structural Dynamics, and Materials Conference*. American Institute of Aeronautics and Astronautics Inc., 2015. ISBN 9781624103421. doi: 10.2514/6.2015-0439.

S. R. Henrichsen, P. M. Weaver, E. Lindgaard, and E. Lund. Post-buckling optimization of composite structures using koiter's method. *International Journal for Numerical Methods in Engineering*, 108(8):902–940, 2016. doi: https://doi.org/10.1002/nme.5239.

C. O. Horgan. Recent developments concerning saint-venant's principle: A second update. *Applied Mechanics Reviews*, 49(10S):S101–S111, Oct. 1996. ISSN 2379-0407. doi: 10.1115/1.3101961.

G. Houston, D. Quinn, A. Murphy, and F. Bron. Design rules for stiffened panel buckling containment features. *Thin-Walled Structures*, 116:69–81, 7 2017. ISSN 02638231. doi: 10.1016/j.tws.2017.03.006.

Y. Hu, Z. Huang, K. Fan, X. Li, J. Luo, and Q. Liu. A high-fidelity surrogate model for nonlinear analysis in the post-buckling optimization of laminated shells with dual-attention mechanism. *Thin-Walled Structures*, 214:113388, 2025. ISSN 0263-8231. doi: https://doi.org/10.1016/j.tws.2025.113388.

F. Jiang and W. Yu. Prediction of sectional collapse of thin-walled structure under pure bending by nonlinear composite beam theory. *Thin-Walled Structures*, 205:112414, Dec. 2024. ISSN 0263-8231. doi: 10.1016/j.tws.2024.112414.

C. Kassapoglou. *Design and Analysis of Composite Structures: With Applications to Aerospace Structures*. Wiley, Sept. 2010. ISBN 9780470972700. doi: 10.1002/9780470972700.

G. J. Kennedy and J. R. R. A. Martins. pyCAPS: Python interface to the CAPS geometry and analysis platform. `https://github.com/gtci/pyCAPS`, 2020. Available at `https://github.com/gtci/pyCAPS`.

G. K. Kenway, J. R. Martins, and G. J. Kennedy. Aerostructural optimization of the common research model configuration. In *AIAA AVIATION 2014 -15th AIAA/ISSMO Multidisciplinary Analysis and Optimization Conference*. American Institute of Aeronautics and Astronautics Inc., 2014. ISBN 9781624102837. doi: 10.2514/6.2014-3274.

R. Medeiros, C. Cesnik, O. Stodieck, D. Calderon, J. Cooper, and E. Coetzee. Comparison of structural model reduction methods applied to a large-deformation wing box. *The Aeronautical Journal*, 125(1292):1687–1709, Sept. 2021. ISSN 2059-6464. doi: 10.1017/aer.2021.73.

MIT Aerospace Computational Design Laboratory. *Engineering Sketch Pad (ESP)*. Massachusetts Institute of Technology, Cambridge, MA, USA, 2023. `https://acdl.mit.edu/ESP/`.

F. Mitrotta, A. Pirrera, T. Macquart, J. Cooper, A. Pereira do Prado, and P. Higino Cabral. Proof of concept of a nonlinear structural stability constraint for aeroelastic optimisation. *The Aeronautical Journal*, 129(1335):1237–1264, 2025. doi: 10.1017/aer.2024.151.

A. Muc, M. Chwał, and M. Barski. Remarks on experimental and theoretical investigations of buckling loads for laminated plated and shell structures. *Composite Structures*, 203:861–874, 2018. ISSN 0263-8223. doi: https://doi.org/10.1016/j.compstruct.2018.07.094.

A. Murphy, M. Price, C. Lynch, and A. Gibson. The computational post-buckling analysis of fuselage stiffened panels loaded in shear. *Thin-Walled Structures*, 43 (9):1455–1474, 2005. ISSN 0263-8231. doi: https://doi.org/10.1016/j.tws.2005.03.010.

NASA. Buckling strength of structural plates. Technical Report NASA SP-8068, National Aeronautics and Space Administration, June 1971.

V. Oliveri, D. Peeters, G. J. Clancy, D. Jones, R. O'Higgins, and P. M. Weaver. Design, optimization and manufacturing of a unitized carbon fiber/thermoplastic wingbox structure. In *AIAA/ASCE/AHS/ASC Structures, Structural Dynamics, and Materials Conference, 2018*, volume 0. American Institute of Aeronautics and Astronautics Inc, AIAA, 2018. ISBN 9781624105326. doi: 10.2514/6.2018-0476.

M. F. Othman, G. H. Silva, P. H. Cabral, A. P. Prado, A. Pirrera, and J. E. Cooper. A robust and reliability-based aeroelastic tailoring framework for composite aircraft wings. *Composite Structures*, 208:101–113, 1 2019. ISSN 02638223. doi: 10.1016/j.compstruct.2018.09.086.

H. Rahman, R. De Breuker, and S. G. Castro. Simultaneous layout, sizing and topology optimization of stiffened panels using cad-based parameterization. In *AIAA SCITECH 2023 Forum*. American Institute of Aeronautics and Astronautics, Jan. 2023. doi: 10.2514/6.2023-1090.

K. Rohwer and R. Degenhardt. Simulating postbuckling behaviour and collapse of stiffened CFRP panels. In *Proceedings of the NAFEMS World Congress 2007*, Vancouver, Canada, May 2007.

B. Roman and A. Pocheau. Postbuckling of bilaterally constrained rectangular thin plates. *Journal of the Mechanics and Physics of Solids*, 50(11):2379–2401, 2002. ISSN 0022-5096. doi: https://doi.org/10.1016/S0022-5096(02)00028-5.

O. Seresta, M. M. Abdalla, and Z. Gürdal. Approximate internal load prediction in composite structures with locally buckled panels. *Journal of Aircraft*, 45:513–522, 2008. ISSN 15333868. doi: 10.2514/1.30465.

J. Sodja, N. P. Werter, and R. De Breuker. Design of a flying demonstrator wing for manoeuvre load alleviation with cruise shape constraint. In *AIAA/ASCE/AHS/ASC Structures, Structural Dynamics, and Materials Conference, 2018*, number 210049. American Institute of Aeronautics and Astronautics Inc, AIAA, 2018. ISBN 9781624105326. doi: 10.2514/6.2018-2153.

O. Stodieck, J. E. Cooper, P. M. Weaver, and P. Kealy. Aeroelastic tailoring of a representative wing box using tow-steered composites. *AIAA Journal*, 55(4): 1425–1439, 2017. ISSN 00011452. doi: 10.2514/1.J055364.

W. Yu, D. H. Hodges, and J. C. Ho. Variational asymptotic beam sectional analysis – an updated version. *International Journal of Engineering Science*, 59:40–64, 2012. ISSN 0020-7225. doi: https://doi.org/10.1016/j.ijengsci.2012.03.006. The Special Issue in honor of Victor L. Berdichevsky.

G. Zhang, Y. Hu, B. Yan, M. Tong, and F. Wang. Buckling and post-buckling analysis of composite stiffened panels: A ten-year review (2014–2023). *Thin-Walled Structures*, 205:112525, 2024. ISSN 0263-8231. doi: https://doi.org/10.1016/j.tws.2024.112525.

J. Zhang and C. Bisagni. Buckling-driven mechanisms for twisting control in adaptive composite wings. *Aerospace Science and Technology*, 118:107006, 11 2021. ISSN 1270-9638. doi: 10.1016/J.AST.2021.107006.

R. Zimmermann, H. Klein, and A. Kling. Buckling and postbuckling of stringer stiffened fibre composite curved panels - tests and computations. *Composite Structures*, 73:150–161, 5 2006. ISSN 02638223. doi: 10.1016/j.compstruct.2005.11.050.

Appendix

3.A. Cross-section Modeller Formulation

An introduction to Saint–Venant's principle is necessary for understanding the formulation of the cross-section modeller. A fundamental implication of this principle is that two statically equivalent load distributions produce the same stress state at points sufficiently far from the region where the loads are applied. This behaviour arises from the fact that the linear elastostatic problem is an elliptic boundary-value problem (Horgan, 1996). The elliptic nature of the equations implies the absence of characteristic curves; therefore, discontinuities cannot propagate through the domain. Any localised irregularity or discontinuity at the boundary is smoothed out, resulting in a continuous stress field throughout the interior. This means that only the local disturbances associated with how the load is applied decay with distance, whereas the global effect of the load persists throughout the structure. This spatial smoothing is analogous to dropping a small droplet of ink into still water: the concentration is initially high near the droplet but gradually spreads until a uniform, lower concentration is reached elsewhere.

Consider the prismatic beam shown in Figure 3.13, which has cross-sectional properties constant along the z-direction. According to Saint–Venant's principle, stresses resulting from statically equivalent loads become identical at cross-sections sufficiently far from the load-introduction region. The equilibrium equations of

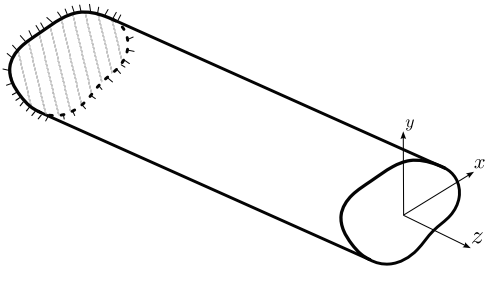

Figure 3.13: Prismatic beam with cross-sectional properties constant along the z-direction.

elasticity, in the absence of body forces, can be written in general tensor form as:

$$\sigma_{ij,j} = 0. \tag{3.12}$$

The general solution of the equilibrium equations can be expressed as a superposition of exponential modes of the form:

$$\boldsymbol{\sigma}(z) = \boldsymbol{c}_i \, e^{\lambda_i z}, \tag{3.13}$$

where $\boldsymbol{\sigma}$ is a vector containing relevant stress components, while $\boldsymbol{c}_i$ is a vector of constants and λ_i is, in general, a complex number given by:

$$\lambda_i = R_i + j\,\omega_i. \tag{3.14}$$

The real part R_i governs the exponential growth or decay of each mode along z, whereas the imaginary part ω_i represents possible oscillatory behaviour as illustrated in Figure 3.14.

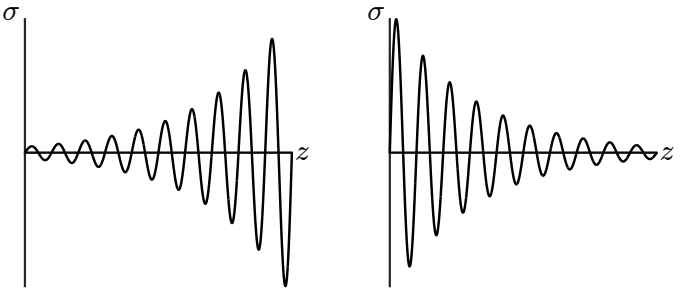

(a) $R_i > 0$ (b) $R_i < 0$

Figure 3.14: Different solution representations of Equation 3.13.

According to Saint–Venant's principle, the growing modes ($R_i > 0$) are not physically admissible, as they would lead to an unbounded stress field away from the load introduction region. The decaying modes ($R_i < 0$) correspond to localised stress disturbances that die out with distance from the load-introduction zone. Of primary interest in the present analysis are the persistent modes, which neither grow nor decay exponentially and therefore correspond to $\lambda_i = 0$. These represent the six classical Saint–Venant stress states: one axial, two bending, one torsional, and two shear modes.

To derive the governing equations, the strain definitions are first introduced using the infinitesimal strain assumption as follows:

$$\begin{aligned} \varepsilon_x &= u_{,x} \\ \varepsilon_y &= v_{,y} \\ \varepsilon_z &= w_{,z} \\ \gamma_{yz} &= v_{,z} + w_{,y} \\ \gamma_{xz} &= u_{,z} + w_{,x} \\ \gamma_{xy} &= u_{,y} + v_{,x}. \end{aligned} \tag{3.15}$$

The strain–displacement relations can be organised in matrix form as:

$$\begin{bmatrix} \varepsilon_x \\ \varepsilon_y \\ \varepsilon_z \\ \gamma_{yz} \\ \gamma_{xz} \\ \gamma_{xy} \end{bmatrix} = \begin{bmatrix} \frac{\partial}{\partial x} & 0 & 0 \\ 0 & \frac{\partial}{\partial y} & 0 \\ 0 & 0 & 0 \\ 0 & 0 & \frac{\partial}{\partial y} \\ 0 & 0 & \frac{\partial}{\partial x} \\ \frac{\partial}{\partial y} & \frac{\partial}{\partial x} & 0 \end{bmatrix} \begin{bmatrix} u \\ v \\ w \end{bmatrix} + \begin{bmatrix} 0 & 0 & 0 \\ 0 & 0 & 0 \\ 0 & 0 & 1 \\ 0 & 1 & 0 \\ 1 & 0 & 0 \\ 0 & 0 & 0 \end{bmatrix} \begin{bmatrix} u' \\ v' \\ w' \end{bmatrix} \tag{3.16}$$

which can be written in a compact form as:

$$\boldsymbol{\varepsilon} = \mathbf{B_0}\,\boldsymbol{q} + \mathbf{B_1}\,\boldsymbol{q'} \tag{3.17}$$

where the prime denotes differentiation with respect to z.

The total strain energy is then defined as:

$$U = \int_V \frac{1}{2}\boldsymbol{\varepsilon}^\top \mathbf{C}\,\boldsymbol{\varepsilon}\,dV, \tag{3.18}$$

where V represents the volume and $\mathbf{C}$ is the constitutive matrix. Per unit depth in the z direction, the integration becomes:

$$U = \int_A \frac{1}{2}\boldsymbol{\varepsilon}^\top \mathbf{C}\boldsymbol{\varepsilon}\,dA, \tag{3.19}$$

where A represents the area.

Substituting Equation 3.17 into Equation 3.19 yields:

$$U = \frac{1}{2}\int_A \left(\boldsymbol{q}^\top \mathbf{B_0}^\top \mathbf{C}\mathbf{B_0}\boldsymbol{q} + 2\boldsymbol{q}^\top \mathbf{B_0}^\top \mathbf{C}\mathbf{B_1}\boldsymbol{q'} + \boldsymbol{q'}^\top \mathbf{B_1}^\top \mathbf{C}\mathbf{B_1}\boldsymbol{q'}\right) dA \tag{3.20}$$

which could be expressed more compactly as:

$$U = \frac{1}{2}\int_A \left(\boldsymbol{q}^\top \mathbf{K_{00}}\boldsymbol{q} + 2\boldsymbol{q}^\top \mathbf{K_{01}}\boldsymbol{q'} + \boldsymbol{q'}^\top \mathbf{K_{11}}\boldsymbol{q'}\right)\, dA, \tag{3.21}$$

where

$$\mathbf{K_{00}} = \mathbf{B_0}^\top \mathbf{C}\mathbf{B_0}, \quad \mathbf{K_{01}} = \mathbf{B_0}^\top \mathbf{C}\mathbf{B_1}, \quad \mathbf{K_{11}} = \mathbf{B_1}^\top \mathbf{C}\mathbf{B_1} \tag{3.22}$$

The Lagrangian functional is generally defined as follows:

$$L = U - W - T, \tag{3.23}$$

where W is the work done by external forces and T is the kinetic energy.

For the present static and unloaded cross-sectional formulation, neither the kinetic nor the external potential terms are considered. Consequently, the Lagrangian density is defined to be:

$$\mathcal{L} = \frac{1}{2}\left(\boldsymbol{q}^\top \mathbf{K_{00}}\boldsymbol{q} + 2\boldsymbol{q}^\top \mathbf{K_{01}}\boldsymbol{q'} + \boldsymbol{q'}^\top \mathbf{K_{11}}\boldsymbol{q'}\right). \tag{3.24}$$

To set up the Euler-Lagrange equations, the generalised momenta are defined as follows:

$$\boldsymbol{p} = \frac{\partial \mathcal{L}}{\partial \boldsymbol{q'}} = \mathbf{K_{10}}\boldsymbol{q} + \mathbf{K_{11}}\boldsymbol{q'}, \tag{3.25}$$

where $\mathbf{K_{10}} = \mathbf{K_{01}}^\top$.

The Euler-Lagrange equation states that:

$$\frac{d\boldsymbol{p}}{dz} = \frac{\partial \mathcal{L}}{\partial \boldsymbol{q}} \tag{3.26}$$

leading to:

$$\boldsymbol{p'} = \mathbf{K_{00}}\boldsymbol{q} + \mathbf{K_{01}}\boldsymbol{q'}. \tag{3.27}$$

To obtain $\boldsymbol{q'}$ in terms of $\boldsymbol{q}$ and $\boldsymbol{p}$, Equation 3.25 is rearranged:

$$\boldsymbol{q'} = -\mathbf{K_{11}^{-1}}\mathbf{K_{10}}\boldsymbol{q} + \mathbf{K_{11}^{-1}}\boldsymbol{p} \tag{3.28}$$

Equations 3.28, 3.27 can be expressed in matrix form as follows:

$$\begin{bmatrix}\boldsymbol{q'}\\ \boldsymbol{p'}\end{bmatrix} = \begin{bmatrix}-\mathbf{K_{11}^{-1}}\mathbf{K_{10}} & \mathbf{K_{11}^{-1}}\\ \mathbf{K_{00}} - \mathbf{K_{01}}\mathbf{K_{11}^{-1}}\mathbf{K_{10}} & \mathbf{K_{01}}\mathbf{K_{11}^{-1}}\end{bmatrix}\begin{bmatrix}\boldsymbol{q}\\ \boldsymbol{p}\end{bmatrix} \tag{3.29}$$

This system can be represented as:

$$\boldsymbol{x'} = \mathcal{A}\boldsymbol{x}. \tag{3.30}$$

Before proceeding, the reader is referred to Appendix 3.B, where the algebraic relations associated with rigid-body motion – such as the null-space properties of $\mathbf{K_{00}}$ and the coupling relations among $\mathbf{K_{00}}, \mathbf{K_{01}}, \mathbf{K_{10}}$, and $\mathbf{K_{11}}$ – are derived. These relations are not needed conceptually at this point, but they will be used extensively to simplify the expressions that follow.

Persistent solutions come from eigenvectors corresponding to zero eigenvalues. Looking for solutions in the null space of $\mathcal{A}$, the following relation is considered:

$$\begin{bmatrix}-\mathbf{K_{11}^{-1}}\mathbf{K_{10}} & \mathbf{K_{11}^{-1}}\\ \mathbf{K_{00}} - \mathbf{K_{01}}\mathbf{K_{11}^{-1}}\mathbf{K_{10}} & \mathbf{K_{01}}\mathbf{K_{11}^{-1}}\end{bmatrix}\begin{bmatrix}\boldsymbol{r}\\ \boldsymbol{s}\end{bmatrix} = \begin{bmatrix}\mathbf{0}\\ \mathbf{0}\end{bmatrix}, \tag{3.31}$$

where $\boldsymbol{r}$ and $\boldsymbol{s}$ are the unknown vectors to solve for. The previous system can be rewritten as follows:

$$\mathcal{A}\,\boldsymbol{\phi_i^0} = \mathbf{0}, \tag{3.32}$$

where $i = 1, 2, \ldots$

From the results obtained in Appendix 3.B, it is clear that $\boldsymbol{r}$ lies in the null space of $\mathbf{K_{00}}$ and $\mathbf{K_{10}}$ when it is equal to any of the following vectors: $\{\boldsymbol{t_1}, \boldsymbol{t_2}, \boldsymbol{t_3}, \boldsymbol{r_3}\}$. For the four cases, solving for $\boldsymbol{s}$ gives the following eigenvectors $\boldsymbol{\phi_i^0}$:

$$\begin{bmatrix}\boldsymbol{t_1}\\ \mathbf{0}\end{bmatrix}, \begin{bmatrix}\boldsymbol{t_2}\\ \mathbf{0}\end{bmatrix}, \begin{bmatrix}\boldsymbol{t_3}\\ \mathbf{0}\end{bmatrix}, \begin{bmatrix}\boldsymbol{r_3}\\ \mathbf{0}\end{bmatrix}. \tag{3.33}$$

These four eigenvectors correspond to uniform cross-sectional displacements accompanied by zero stress resultants. The eigenvalue problem of Equation 3.32 therefore yields four eigenvectors associated with the zero eigenvalue, although the algebraic multiplicity of this eigenvalue is known to be higher. This discrepancy shows that the eigenvalue is defective: the four eigenvectors do not span the full invariant subspace associated with $\lambda = 0$. This is consistent with the fact that the system matrix $\mathcal{A}$ is non-normal, meaning that $\mathcal{A}\mathcal{A}^\top \neq \mathcal{A}^\top\mathcal{A}$, and non-normal matrices may not admit a full basis of linearly independent eigenvectors for repeated eigenvalues. As a result, the eigenvectors obtained from Equation 3.32 must be supplemented by

generalised eigenvectors in order to span the minimal invariant subspace associated with the zero eigenvalue.

In the present formulation, the state vector $\boldsymbol{x} = [\boldsymbol{q}; \boldsymbol{p}]$ contains both displacement components and stress resultants, as later shown in Equation 3.80. The eigenvectors obtained above represent the lowest-order persistent modes, characterised by uniform displacements and zero stress resultants. The generalised eigenvectors introduce higher-order persistent patterns: the first set exhibits linear variations in the displacement field accompanied by uniform stress resultants, while the next set introduces quadratic displacement patterns coupled with linearly varying stress resultants. Taken together, the eigenvectors and their generalised counterparts span the complete invariant subspace associated with the persistent Saint–Venant solutions in the displacement–stress formulation. The first set of generalised eigenvectors is obtained from the relation:

$$\mathcal{A}\boldsymbol{m_i} = \boldsymbol{\phi_i^0}, \tag{3.34}$$

where $\boldsymbol{m_i}$ are the vectors in the first set of generalised eigenvectors, and $\boldsymbol{\phi_i^0}$ are the obtained eigenvectors in the null space of $\mathcal{A}$.

To obtain the first vector, consider that:

$$\boldsymbol{m_1} = \begin{bmatrix} \boldsymbol{r} \\ \boldsymbol{s} \end{bmatrix}, \quad \boldsymbol{\phi_1^0} = \begin{bmatrix} \boldsymbol{t_1} \\ \boldsymbol{0} \end{bmatrix}. \tag{3.35}$$

The first equation of this system of equations is:

$$-\mathbf{K_{11}^{-1}}\mathbf{K_{10}}\boldsymbol{r} + \mathbf{K_{11}^{-1}}\boldsymbol{s} = \boldsymbol{t_1} \tag{3.36}$$

Solving for $\boldsymbol{s}$ gives:

$$\boldsymbol{s} = \mathbf{K_{10}}\boldsymbol{r} + \mathbf{K_{11}}\boldsymbol{t_1} \tag{3.37}$$

Substituting in the second equation of the system leads to:

$$\left(\mathbf{K_{00}} - \mathbf{K_{01}}\mathbf{K_{11}^{-1}}\mathbf{K_{10}}\right)\boldsymbol{r} + \mathbf{K_{01}}\mathbf{K_{11}^{-1}}\left(\mathbf{K_{10}}\boldsymbol{r} + \mathbf{K_{11}}\boldsymbol{t_1}\right) = \boldsymbol{0} \tag{3.38}$$

After simplification and using the relations of Equation 3.108, the following relation is obtained:

$$\mathbf{K_{00}}\boldsymbol{r} = \mathbf{K_{00}}\boldsymbol{r_2}. \tag{3.39}$$

The solvability of this system is checked by left-multiplying both sides by the transpose of the vectors in the null space of $\mathbf{K_{00}}$. It is very clear in that case that all relations obtain zero, given the symmetry of $\mathbf{K_{00}}$, for example:

$$\boldsymbol{t_1}^\top\mathbf{K_{00}}\boldsymbol{r} = \boldsymbol{t_1}^\top\mathbf{K_{00}}\boldsymbol{r_2} \;\rightarrow\; \left(\mathbf{K_{00}}\boldsymbol{t_1}\right)^\top\boldsymbol{r} = \left(\mathbf{K_{00}}\boldsymbol{t_1}\right)^\top\boldsymbol{r_2} = \boldsymbol{0}. \tag{3.40}$$

That means the system is solvable and the current relation is obtained:

$$\boldsymbol{r} = \boldsymbol{r_2} \tag{3.41}$$

Substituting Equation 3.41 into Equation 3.37, gives:

$$\boldsymbol{s} = \mathbf{K_{10}}\boldsymbol{r_2} + \mathbf{K_{11}}\boldsymbol{t_1} \tag{3.42}$$

By investigating Equation 3.109, the equations simplify to:

$$\boldsymbol{s} = \mathbf{0} \;\rightarrow\; \boldsymbol{m_1} = \begin{bmatrix} \boldsymbol{r_2} \\ \mathbf{0} \end{bmatrix}. \tag{3.43}$$

Following the same procedure, but using the rest of the vectors ($\boldsymbol{\phi_i^0}$) in the null space of $\mathcal{A}$. The following generalised eigenvectors are obtained:

$$\boldsymbol{m_2} = \begin{bmatrix} -\boldsymbol{r_1} \\ \mathbf{0} \end{bmatrix}, \quad \boldsymbol{m_3} = \begin{bmatrix} \boldsymbol{w_1} \\ \mathbf{K_{10}}\boldsymbol{w_1} + \mathbf{K_{11}}\boldsymbol{t_3} \end{bmatrix}, \quad \boldsymbol{m_4} = \begin{bmatrix} \boldsymbol{w_2} \\ \mathbf{K_{10}}\boldsymbol{w_2} + \mathbf{K_{11}}\boldsymbol{r_3} \end{bmatrix}, \tag{3.44}$$

where $\boldsymbol{w_1}$ and $\boldsymbol{w_2}$ are the solutions of the systems of equations:

$$\mathbf{K_{00}}\boldsymbol{w_1} = -\mathbf{K_{01}}\boldsymbol{t_3}, \quad \mathbf{K_{00}}\boldsymbol{w_2} = -\mathbf{K_{01}}\boldsymbol{r_3}. \tag{3.45}$$

The next set of generalised eigenvectors is obtained by solving the following equation:

$$\mathcal{A}\boldsymbol{d_i} = \boldsymbol{m_i} \tag{3.46}$$

To obtain the first vector in this set:

$$\boldsymbol{d_1} = \begin{bmatrix} \boldsymbol{r} \\ \boldsymbol{s} \end{bmatrix}, \quad \boldsymbol{m_1} = \begin{bmatrix} \boldsymbol{r_2} \\ \mathbf{0} \end{bmatrix} \tag{3.47}$$

The first equation of the system will be:

$$-\mathbf{K_{11}^{-1}}\mathbf{K_{10}}\boldsymbol{r} + \mathbf{K_{11}^{-1}}\boldsymbol{s} = \boldsymbol{r_2} \tag{3.48}$$

Solving for $\boldsymbol{s}$ gives:

$$\boldsymbol{s} = \mathbf{K_{10}}\boldsymbol{r} + \mathbf{K_{11}}\boldsymbol{r_2} \tag{3.49}$$

Substituting s into the second equation of the system yields:

$$(\mathbf{K_{00}} - \mathbf{K_{01}}\mathbf{K_{11}^{-1}}\mathbf{K_{10}})\boldsymbol{r} + \mathbf{K_{01}}\mathbf{K_{11}^{-1}}(\mathbf{K_{10}}\boldsymbol{r} + \mathbf{K_{11}}\boldsymbol{r_2}) = 0 \tag{3.50}$$

which simplifies to:

$$\mathbf{K_{00}}\boldsymbol{r} = -\mathbf{K_{01}}\boldsymbol{r_2}. \tag{3.51}$$

The solvability condition is checked in the same procedure as done in Equation 3.40. It is clear that the solvability condition is achieved for all the vectors in the null space of $\mathbf{K_{00}}$, with the solution of the system assumed to be:

$$\boldsymbol{r} = \boldsymbol{w_3} \tag{3.52}$$

leading to:

$$\boldsymbol{d_1} = \begin{bmatrix} \boldsymbol{w_3} \\ \mathbf{K_{10}}\boldsymbol{w_3} + \mathbf{K_{11}}\boldsymbol{r_2} \end{bmatrix}. \tag{3.53}$$

Following the same procedure, the second generalised eigenvector in this set is obtained:

$$\boldsymbol{d_2} = \begin{bmatrix} \boldsymbol{w_4} \\ \mathbf{K_{10}}\boldsymbol{w_4} - \mathbf{K_{11}}\boldsymbol{r_1} \end{bmatrix}, \tag{3.54}$$

where $\boldsymbol{w_4}$ is the solution of the system:

$$\mathbf{K_{00}}\boldsymbol{r} = \mathbf{K_{01}}\boldsymbol{r_1}. \tag{3.55}$$

For the rest of the vectors, the solvability conditions are not met for the following systems of equations:

$$\begin{gathered}\mathbf{K_{00}}\boldsymbol{r} + \mathbf{K_{01}}\boldsymbol{w_1} = \mathbf{K_{10}}\boldsymbol{w_1} + \mathbf{K_{11}}\boldsymbol{t_3}, \\ (\mathbf{K_{00}} - \mathbf{K_{01}}\mathbf{K_{11}^{-1}}\mathbf{K_{10}})\boldsymbol{r} + \mathbf{K_{01}}\mathbf{K_{11}^{-1}}(\mathbf{K_{10}}\boldsymbol{r} + \mathbf{K_{11}}\boldsymbol{w_1}) = \mathbf{K_{10}}\boldsymbol{w_2} + \mathbf{K_{11}}\boldsymbol{r_3}.\end{gathered} \tag{3.56}$$

Theoretically, if there exists another set of generalised eigenvectors, it will follow the relation:

$$\mathcal{A}\boldsymbol{h_i} = \boldsymbol{d_i} \tag{3.57}$$

But again, solvability conditions are not achieved, which means no more generalised eigenvectors can be obtained for the system. Although no additional generalised eigenvectors can be obtained from the system, the subspace associated with the zero eigenvalue is not restricted to the specific vectors already derived. A linear combination of the existing eigenvectors and generalised eigenvectors still lies in the same invariant subspace and therefore represents an admissible persistent solution. For this reason, additional generalised eigenvectors are constructed as suitable linear combinations of the previously obtained vectors. Rewriting the generalised eigenvectors from Equations 3.44, 3.53 and 3.54 in this form:

$$\boldsymbol{m_3} = \begin{bmatrix}\boldsymbol{w_1} \\ \boldsymbol{\chi_1}\end{bmatrix}, \quad \boldsymbol{m_4} = \begin{bmatrix}\boldsymbol{w_2} \\ \boldsymbol{\chi_2}\end{bmatrix}, \quad \boldsymbol{d_1} = \begin{bmatrix}\boldsymbol{w_3} \\ \boldsymbol{\chi_3}\end{bmatrix}, \quad \boldsymbol{d_2} = \begin{bmatrix}\boldsymbol{w_4} \\ \boldsymbol{\chi_4}\end{bmatrix}. \tag{3.58}$$

A new set of generalised eigenvectors could be obtained by using linear combinations of previously obtained generalised eigenvectors as follows:

$$\begin{bmatrix}-\mathbf{K_{11}^{-1}}\mathbf{K_{10}} & \mathbf{K_{11}^{-1}} \\ \mathbf{K_{00}} - \mathbf{K_{01}}\mathbf{K_{11}^{-1}}\mathbf{K_{10}} & \mathbf{K_{01}}\mathbf{K_{11}^{-1}}\end{bmatrix}\begin{bmatrix}\boldsymbol{r} \\ \boldsymbol{s}\end{bmatrix} = \begin{bmatrix}\boldsymbol{w_3} + \alpha_1\boldsymbol{w_1} + \alpha_2\boldsymbol{w_2} \\ \boldsymbol{\chi_3} + \alpha_1\boldsymbol{\chi_1} + \alpha_2\boldsymbol{\chi_2}\end{bmatrix} \tag{3.59}$$

The system of equations is simplified to the following form:

$$\mathbf{K_{00}}\boldsymbol{r} = \mathbf{K_{01}}\left(\boldsymbol{w_3} + \alpha_1\boldsymbol{w_1} + \alpha_2\boldsymbol{w_2}\right) + \left(\boldsymbol{\chi_3} + \alpha_1\boldsymbol{\chi_1} + \alpha_2\boldsymbol{\chi_2}\right) \tag{3.60}$$

To check the solvability of Equation 3.60, the equation is left-multiplied by $\boldsymbol{t_1}^\top$, $\boldsymbol{t_2}^\top$, $\boldsymbol{t_3}^\top$, and $\boldsymbol{r_3}^\top$. The first condition to check is:

$$\cancelto{0}{\boldsymbol{t_1}^\top\mathbf{K_{00}}\boldsymbol{r}} = \cancelto{0}{\boldsymbol{t_1}^\top\mathbf{K_{01}}}\left(\boldsymbol{w_3} + \alpha_1\boldsymbol{w_1} + \alpha_2\boldsymbol{w_2}\right) + \boldsymbol{t_1}^\top\left(\boldsymbol{\chi_3} + \alpha_1\boldsymbol{\chi_1} + \alpha_2\boldsymbol{\chi_2}\right) \tag{3.61}$$

The term $\boldsymbol{t_1}^\top\boldsymbol{\chi_1}$, is simplified as follows:

$$\boldsymbol{t_1}^\top\boldsymbol{\chi_1} = \left(\mathbf{K_{01}}\boldsymbol{t_1}\right)^\top\boldsymbol{w_1} + \left(\mathbf{K_{11}}\boldsymbol{t_1}\right)^\top\boldsymbol{t_3} \tag{3.62}$$

From Equation 3.108, the expression could be further simplified:

$$\boldsymbol{t_1}^\top\boldsymbol{\chi_1} = \left(-\mathbf{K_{00}}\boldsymbol{r_2}\right)^\top\boldsymbol{w_1} + \left(\mathbf{K_{11}}\boldsymbol{t_1}\right)^\top\boldsymbol{t_3} = -\boldsymbol{r_2}^\top\mathbf{K_{00}}\boldsymbol{w_1} + \left(\mathbf{K_{11}}\boldsymbol{t_1}\right)^\top\boldsymbol{t_3} \tag{3.63}$$

Using Equation 3.45, further tailoring is possible:

$$\boldsymbol{t_1}^\top \boldsymbol{\chi_1} = \boldsymbol{r_2}^\top \mathbf{K_{01}} \boldsymbol{t_3} + \left(\mathbf{K_{11}} \boldsymbol{t_1}\right)^\top \boldsymbol{t_3} = \left(\mathbf{K_{10}} \boldsymbol{r_2}\right)^\top \boldsymbol{t_3} + \left(\mathbf{K_{11}} \boldsymbol{t_1}\right)^\top \boldsymbol{t_3} \tag{3.64}$$

Finally, using Equation 3.109:

$$\boldsymbol{t_1}^\top \boldsymbol{\chi_1} = \left(-\mathbf{K_{11}} \boldsymbol{t_1}\right)^\top \boldsymbol{t_3} + \left(\mathbf{K_{11}} \boldsymbol{t_1}\right)^\top \boldsymbol{t_3} = 0. \tag{3.65}$$

The same procedure can be followed to prove the rest of the relations:

$$\boldsymbol{t_1}^\top \boldsymbol{\chi_1} = \boldsymbol{t_1}^\top \boldsymbol{\chi_2} = \boldsymbol{t_1}^\top \boldsymbol{\chi_3} = \boldsymbol{t_1}^\top \boldsymbol{\chi_4} = 0 \tag{3.66}$$

Also, it could be proven that:

$$\boldsymbol{t_2}^\top \boldsymbol{\chi_1} = \boldsymbol{t_2}^\top \boldsymbol{\chi_2} = \boldsymbol{t_2}^\top \boldsymbol{\chi_3} = \boldsymbol{t_2}^\top \boldsymbol{\chi_4} = 0 \tag{3.67}$$

But for the other vectors:

$$\begin{gathered} \boldsymbol{t_3}^\top \boldsymbol{\chi_1} \neq 0,\ \boldsymbol{t_3}^\top \boldsymbol{\chi_2} \neq 0,\ \boldsymbol{t_3}^\top \boldsymbol{\chi_3} \neq 0,\ \boldsymbol{t_3}^\top \boldsymbol{\chi_4} \neq 0 \\ \boldsymbol{r_3}^\top \boldsymbol{\chi_1} \neq 0,\ \boldsymbol{r_3}^\top \boldsymbol{\chi_2} \neq 0,\ \boldsymbol{r_3}^\top \boldsymbol{\chi_3} \neq 0,\ \boldsymbol{r_3}^\top \boldsymbol{\chi_4} \neq 0 \end{gathered} \tag{3.68}$$

The previous results show that Equation 3.61 equals zero. Similarly, left multiplying Equation 3.60 by $\boldsymbol{t_2}^\top$ leads to zero. The other two solvability conditions are then:

$$\begin{aligned} \boldsymbol{t_3}^\top \boldsymbol{\chi_3} + \alpha_1 \boldsymbol{t_3}^\top \boldsymbol{\chi_1} + \alpha_2 \boldsymbol{t_3}^\top \boldsymbol{\chi_2} = 0 \\ \boldsymbol{r_3}^\top \boldsymbol{\chi_3} + \alpha_1 \boldsymbol{r_3}^\top \boldsymbol{\chi_1} + \alpha_2 \boldsymbol{r_3}^\top \boldsymbol{\chi_2} = 0 \end{aligned} \tag{3.69}$$

which could be represented in matrix form as:

$$\begin{bmatrix} \boldsymbol{t_3}^\top \boldsymbol{\chi_1} & \boldsymbol{t_3}^\top \boldsymbol{\chi_2} \\ \boldsymbol{r_3}^\top \boldsymbol{\chi_1} & \boldsymbol{r_3}^\top \boldsymbol{\chi_2} \end{bmatrix} \begin{bmatrix} \alpha_1 \\ \alpha_2 \end{bmatrix} = \begin{bmatrix} -\boldsymbol{t_3}^\top \boldsymbol{\chi_3} \\ -\boldsymbol{r_3}^\top \boldsymbol{\chi_3} \end{bmatrix} \tag{3.70}$$

Given that condition, a solution to the system of Equation 3.59 is:

$$\boldsymbol{h_1} = \begin{bmatrix} \boldsymbol{w_5} \\ \mathbf{K_{10}} \boldsymbol{w_5} + \mathbf{K_{11}} \left(\boldsymbol{w_3} + \alpha_1 \boldsymbol{w_1} + \alpha_2 \boldsymbol{w_2}\right) \end{bmatrix} = \begin{bmatrix} \boldsymbol{w_5} \\ \boldsymbol{\chi_5} \end{bmatrix}, \tag{3.71}$$

where $\boldsymbol{w_5}$ is the solution to the system of Equation 3.60

The second generalised eigenvector is obtained by solving the system:

$$\begin{bmatrix} -\mathbf{K_{11}^{-1}} \mathbf{K_{10}} & \mathbf{K_{11}^{-1}} \\ \mathbf{K_{00}} - \mathbf{K_{01}} \mathbf{K_{11}^{-1}} \mathbf{K_{10}} & \mathbf{K_{01}} \mathbf{K_{11}^{-1}} \end{bmatrix} \begin{bmatrix} \boldsymbol{r} \\ \boldsymbol{s} \end{bmatrix} = \begin{bmatrix} \boldsymbol{w_4} + \alpha_3 \boldsymbol{w_1} + \alpha_4 \boldsymbol{w_2} \\ \boldsymbol{\chi_4} + \alpha_3 \boldsymbol{\chi_1} + \alpha_4 \boldsymbol{\chi_2} \end{bmatrix} \tag{3.72}$$

The system of equations is simplified to the following form:

$$\mathbf{K_{00}} \boldsymbol{r} = \mathbf{K_{01}} \left(\boldsymbol{w_4} + \alpha_3 \boldsymbol{w_1} + \alpha_4 \boldsymbol{w_2}\right) + \left(\boldsymbol{\chi_4} + \alpha_3 \boldsymbol{\chi_1} + \alpha_4 \boldsymbol{\chi_2}\right). \tag{3.73}$$

Following the same procedure as before, the solvability conditions require that:

$$\begin{bmatrix} \boldsymbol{t_3}^\top \boldsymbol{\chi_1} & \boldsymbol{t_3}^\top \boldsymbol{\chi_2} \\ \boldsymbol{r_3}^\top \boldsymbol{\chi_1} & \boldsymbol{r_3}^\top \boldsymbol{\chi_2} \end{bmatrix} \begin{bmatrix} \alpha_3 \\ \alpha_4 \end{bmatrix} = \begin{bmatrix} -\boldsymbol{t_3}^\top \boldsymbol{\chi_4} \\ -\boldsymbol{r_3}^\top \boldsymbol{\chi_4} \end{bmatrix}, \tag{3.74}$$

and the solution to the system of Equation 3.72 is:

$$\boldsymbol{h_2} = \begin{bmatrix} \boldsymbol{w_6} \\ \mathbf{K_{10}}\boldsymbol{w_6} + \mathbf{K_{11}}\left(\boldsymbol{w_4} + \alpha_3\boldsymbol{w_1} + \alpha_4\boldsymbol{w_2}\right) \end{bmatrix} = \begin{bmatrix} \boldsymbol{w_6} \\ \boldsymbol{\chi_6} \end{bmatrix}, \tag{3.75}$$

where $\boldsymbol{w_6}$ is the solution to the system of Equation 3.73.

All eigenvectors and generalised eigenvectors required for the present formulation have now been derived. To describe persistent solutions, x is defined as a linear combination of predefined eigenvectors and generalised eigenvectors as follows:

$$\begin{gathered} \boldsymbol{x} = c_1\boldsymbol{\phi_1^0} + c_2\boldsymbol{\phi_2^0} + c_3\boldsymbol{\phi_3^0} + c_4\boldsymbol{\phi_4^0} + c_5\boldsymbol{m_1} + c_6\boldsymbol{m_2} + \\ c_7\boldsymbol{m_3} + c_8\boldsymbol{m_4} + c_9\boldsymbol{d_1} + c_{10}\boldsymbol{d_2} + c_{11}\boldsymbol{h_1} + c_{12}\boldsymbol{h_2} \end{gathered} \tag{3.76}$$

Substituting Equation 3.76 into Equation 3.30:

$$\begin{gathered} c_1'\boldsymbol{\phi_1^0} + c_2'\boldsymbol{\phi_2^0} + c_3'\boldsymbol{\phi_3^0} + c_4'\boldsymbol{\phi_4^0} + c_5'\boldsymbol{m_1} + c_6'\boldsymbol{m_2} + \\ c_7'\boldsymbol{m_3} + c_8'\boldsymbol{m_4} + c_9'\boldsymbol{d_1} + c_{10}'\boldsymbol{d_2} + c_{11}'\boldsymbol{h_1} + c_{12}'\boldsymbol{h_2} \\ = \mathcal{A}\big(c_1\boldsymbol{\phi_1^0} + c_2\boldsymbol{\phi_2^0} + c_3\boldsymbol{\phi_3^0} + c_4\boldsymbol{\phi_4^0} + c_5\boldsymbol{m_1} + c_6\boldsymbol{m_2} + \\ c_7\boldsymbol{m_3} + c_8\boldsymbol{m_4} + c_9\boldsymbol{d_1} + c_{10}\boldsymbol{d_2} + c_{11}\boldsymbol{h_1} + c_{12}\boldsymbol{h_2}\big) \end{gathered} \tag{3.77}$$

Substituting Equations 3.32, 3.34, 3.46, 3.59, and 3.72 into Equation 3.77:

$$\begin{gathered} c_1'\boldsymbol{\phi_1^0} + c_2'\boldsymbol{\phi_2^0} + c_3'\boldsymbol{\phi_3^0} + c_4'\boldsymbol{\phi_4^0} + c_5'\boldsymbol{m_1} + c_6'\boldsymbol{m_2} + \\ c_7'\boldsymbol{m_3} + c_8'\boldsymbol{m_4} + c_9'\boldsymbol{d_1} + c_{10}'\boldsymbol{d_2} + c_{11}'\boldsymbol{h_1} + c_{12}'\boldsymbol{h_2} \\ = c_6\boldsymbol{\phi_2^0} + c_7\boldsymbol{\phi_3^0} + c_8\boldsymbol{\phi_4^0} + c_9\boldsymbol{m_1} + c_{10}\boldsymbol{m_2} + \\ c_{11}\left(\boldsymbol{d_1} + \alpha_1\boldsymbol{m_3} + \alpha_2\boldsymbol{m_4}\right) + c_{12}\left(\boldsymbol{d_2} + \alpha_3\boldsymbol{m_3} + \alpha_4\boldsymbol{m_4}\right) \end{gathered} \tag{3.78}$$

From the previous equation, it could be easily proven:

$$\begin{gathered} c_1' = c_5,\ c_2' = c_6,\ c_3' = c_7,\ c_4' = c_8,\ c_5' = c_9, \\ c_6' = c_{10},\ c_7' = \alpha_1 c_{11} + \alpha_3 c_{12},\ c_8' = \alpha_2 c_{11} + \alpha_4 c_{12}, \\ c_9' = c_{11},\ c_{10}' = c_{12},\ c_{11}' = 0,\ c_{12}' = 0. \end{gathered} \tag{3.79}$$

The tractions over the cross-section are now defined to derive the cross-sectional stiffness. The generalised momenta expression could be expanded by substituting Equation 3.22 into Equation 3.25:

$$\boldsymbol{p} = \mathbf{B_1^\top C}\left(\mathbf{B_0}\boldsymbol{q} + \mathbf{B_1}\boldsymbol{q'}\right) = \mathbf{B_1^\top}\boldsymbol{\sigma} = \begin{bmatrix} \tau_{zx} \\ \tau_{zy} \\ \sigma_z \end{bmatrix} \tag{3.80}$$

which gives the tractions over the cross-section. For simplicity, the forces and moments over the cross-section will be named f_1, f_2, f_3, M_1, M_2, and M_3 and are defined as follows:

$$\begin{gathered} f_1 = \boldsymbol{t_1}^\top\boldsymbol{p},\ \ f_2 = \boldsymbol{t_2}^\top\boldsymbol{p},\ \ f_3 = \boldsymbol{t_3}^\top\boldsymbol{p}, \\ M_1 = \boldsymbol{r_1}^\top\boldsymbol{p},\ \ M_2 = \boldsymbol{r_2}^\top\boldsymbol{p},\ \ M_3 = \boldsymbol{r_3}^\top\boldsymbol{p}, \end{gathered} \tag{3.81}$$

Given Equation 3.76, the previous equations can be represented in matrix form as follows:

$$\begin{bmatrix} f_1 \\ f_2 \\ f_3 \\ M_1 \\ M_2 \\ M_3 \end{bmatrix} = \begin{bmatrix} \boldsymbol{t_1}^\top \boldsymbol{\chi_1} & \boldsymbol{t_1}^\top \boldsymbol{\chi_2} & \boldsymbol{t_1}^\top \boldsymbol{\chi_3} & \boldsymbol{t_1}^\top \boldsymbol{\chi_4} & \boldsymbol{t_1}^\top \boldsymbol{\chi_5} & \boldsymbol{t_1}^\top \boldsymbol{\chi_6} \\ \boldsymbol{t_2}^\top \boldsymbol{\chi_1} & \boldsymbol{t_2}^\top \boldsymbol{\chi_2} & \boldsymbol{t_2}^\top \boldsymbol{\chi_3} & \boldsymbol{t_2}^\top \boldsymbol{\chi_4} & \boldsymbol{t_2}^\top \boldsymbol{\chi_5} & \boldsymbol{t_2}^\top \boldsymbol{\chi_6} \\ \boldsymbol{t_3}^\top \boldsymbol{\chi_1} & \boldsymbol{t_3}^\top \boldsymbol{\chi_2} & \boldsymbol{t_3}^\top \boldsymbol{\chi_3} & \boldsymbol{t_3}^\top \boldsymbol{\chi_4} & \boldsymbol{t_3}^\top \boldsymbol{\chi_5} & \boldsymbol{t_3}^\top \boldsymbol{\chi_6} \\ \boldsymbol{r_1}^\top \boldsymbol{\chi_1} & \boldsymbol{r_1}^\top \boldsymbol{\chi_2} & \boldsymbol{r_1}^\top \boldsymbol{\chi_3} & \boldsymbol{r_1}^\top \boldsymbol{\chi_4} & \boldsymbol{r_1}^\top \boldsymbol{\chi_5} & \boldsymbol{r_1}^\top \boldsymbol{\chi_6} \\ \boldsymbol{r_2}^\top \boldsymbol{\chi_1} & \boldsymbol{r_2}^\top \boldsymbol{\chi_2} & \boldsymbol{r_2}^\top \boldsymbol{\chi_3} & \boldsymbol{r_2}^\top \boldsymbol{\chi_4} & \boldsymbol{r_2}^\top \boldsymbol{\chi_5} & \boldsymbol{r_2}^\top \boldsymbol{\chi_6} \\ \boldsymbol{r_3}^\top \boldsymbol{\chi_1} & \boldsymbol{r_3}^\top \boldsymbol{\chi_2} & \boldsymbol{r_3}^\top \boldsymbol{\chi_3} & \boldsymbol{r_3}^\top \boldsymbol{\chi_4} & \boldsymbol{r_3}^\top \boldsymbol{\chi_5} & \boldsymbol{r_3}^\top \boldsymbol{\chi_6} \end{bmatrix} \begin{bmatrix} c_7 \\ c_8 \\ c_9 \\ c_{10} \\ c_{11} \\ c_{12} \end{bmatrix} \tag{3.82}$$

which can be represented in a compact form as follows:

$$\boldsymbol{f} = \boldsymbol{\Phi_1 c}. \tag{3.83}$$

Strain is defined in Equation 3.17 in terms of $\boldsymbol{q}$ and $\boldsymbol{q'}$. From Equation 3.76, $\boldsymbol{q}$ can be expanded as follows:

$$\begin{aligned} \boldsymbol{q} =& c_1\boldsymbol{t_1} + c_2\boldsymbol{t_2} + c_3\boldsymbol{t_3} + c_4\boldsymbol{r_3} + c_5\boldsymbol{r_1} + c_6\boldsymbol{r_2} + c_7\boldsymbol{w_1} + c_8\boldsymbol{w_2} + \\ & c_9\boldsymbol{w_3} + c_{10}\boldsymbol{w_4} + c_{11}\boldsymbol{w_5} + c_{12}\boldsymbol{w_6} \end{aligned} \tag{3.84}$$

Similarly, $\boldsymbol{q'}$ is expanded and using Equation 3.79, strain is expressed as follows:

$$\begin{aligned} \boldsymbol{\varepsilon} =& c_7\left(\mathbf{B_0}\boldsymbol{w_1} + \mathbf{B_1}\boldsymbol{t_3}\right) + c_8\left(\mathbf{B_0}\boldsymbol{w_2} + \mathbf{B_1}\boldsymbol{r_3}\right) + c_9\left(\mathbf{B_0}\boldsymbol{w_3} + \mathbf{B_1}\boldsymbol{r_2}\right) + \\ & c_{10}\left(\mathbf{B_0}\boldsymbol{w_4} - \mathbf{B_1}\boldsymbol{r_1}\right) + c_{11}\left(\mathbf{B_0}\boldsymbol{w_5} + \mathbf{B_1}\left(\boldsymbol{w_3} + \alpha_1\boldsymbol{w_1} + \alpha_2\boldsymbol{w_2}\right)\right) + \\ & c_{12}\left(\mathbf{B_0}\boldsymbol{w_6} + \mathbf{B_1}\left(\boldsymbol{w_4} + \alpha_3\boldsymbol{w_1} + \alpha_4\boldsymbol{w_2}\right)\right) \end{aligned} \tag{3.85}$$

which can be represented in a more compact form as:

$$\boldsymbol{\varepsilon} = c_7\boldsymbol{\psi_1} + c_8\boldsymbol{\psi_2} + c_9\boldsymbol{\psi_3} + c_{10}\boldsymbol{\psi_4} + c_{11}\boldsymbol{\psi_5} + c_{12}\boldsymbol{\psi_6} = \boldsymbol{\Phi_2 c} \tag{3.86}$$

Substituting Equation 3.86 into Equation 3.19:

$$U = \frac{1}{2}\int_A \boldsymbol{c}^\top \boldsymbol{\Phi_2}^\top \mathbf{C}\boldsymbol{\Phi_2 c}\, dA = \frac{1}{2}\int_A \boldsymbol{f}^\top \left(\boldsymbol{\Phi_1^{-1}}\right)^\top \boldsymbol{\Phi_2}^\top \mathbf{C}\boldsymbol{\Phi_2}\boldsymbol{\Phi_1^{-1}}\boldsymbol{f}\, dA \tag{3.87}$$

Further simplifications can be made by assuming:

$$\boldsymbol{\Phi_3} = \boldsymbol{\Phi_2}^\top \mathbf{C}\boldsymbol{\Phi_2} \tag{3.88}$$

The elements of the matrix can be simplified. For example, the first term reads:

$$\begin{aligned} \boldsymbol{\psi_1}^\top \mathbf{C}\boldsymbol{\psi_1} =& (\boldsymbol{w_1}^\top \mathbf{B_0}^\top + \boldsymbol{t_3}^\top \mathbf{B_1}^\top)\mathbf{C}(\mathbf{B_0}\boldsymbol{w_1} + \mathbf{B_1}\boldsymbol{t_3}) \\ =& \boldsymbol{w_1}^\top \mathbf{B_0}^\top \mathbf{C}\mathbf{B_0}\boldsymbol{w_1} + \boldsymbol{w_1}^\top \mathbf{B_0}^\top \mathbf{C}\mathbf{B_1}\boldsymbol{t_3} + \boldsymbol{t_3}^\top \mathbf{B_1}^\top \mathbf{C}\mathbf{B_0}\boldsymbol{w_1} + \boldsymbol{t_3}^\top \mathbf{B_1}^\top \mathbf{C}\mathbf{B_1}\boldsymbol{t_3} \\ =& \boldsymbol{w_1}^\top \mathbf{K_{00}}\boldsymbol{w_1} + \boldsymbol{w_1}^\top \mathbf{K_{01}}\boldsymbol{t_3} + \boldsymbol{t_3}^\top \mathbf{K_{10}}\boldsymbol{w_1} + \boldsymbol{t_3}^\top \mathbf{K_{11}}\boldsymbol{t_3} \\ =& \boldsymbol{w_1}^\top \mathbf{K_{00}}\boldsymbol{w_1} + 2\boldsymbol{w_1}^\top \mathbf{K_{01}}\boldsymbol{t_3} + \boldsymbol{t_3}^\top \mathbf{K_{11}}\boldsymbol{t_3} \end{aligned} \tag{3.89}$$

Substituting Equation 3.45 into Equation 3.89:

$$\begin{aligned}\boldsymbol{\psi_1}^\top \mathbf{C} \boldsymbol{\psi_1} = \boldsymbol{t_3}^\top \mathbf{K_{01}} \boldsymbol{w_1} + \boldsymbol{t_3}^\top \mathbf{K_{11}} \boldsymbol{t_3} = \boldsymbol{t_3}^\top (\mathbf{K_{01}} \boldsymbol{w_1} + \mathbf{K_{11}} \boldsymbol{t_3}) \\ = \boldsymbol{t_3}^\top \boldsymbol{\chi_1}.\end{aligned} \tag{3.90}$$

Similarly, the other terms of the matrix can be simplified, leading to the following:

$$\boldsymbol{\Phi_3} = \begin{bmatrix} \boldsymbol{t_3}^\top \boldsymbol{\chi_1} & \boldsymbol{t_3}^\top \boldsymbol{\chi_2} & \boldsymbol{t_3}^\top \boldsymbol{\chi_3} & \boldsymbol{t_3}^\top \boldsymbol{\chi_4} & \boldsymbol{t_3}^\top \boldsymbol{\chi_5} + \boldsymbol{w_1}^\top \boldsymbol{\eta_1} & \boldsymbol{t_3}^\top \boldsymbol{\chi_6} + \boldsymbol{w_1}^\top \boldsymbol{\eta_2} \\ \boldsymbol{r_3}^\top \boldsymbol{\chi_1} & \boldsymbol{r_3}^\top \boldsymbol{\chi_2} & \boldsymbol{r_3}^\top \boldsymbol{\chi_3} & \boldsymbol{r_3}^\top \boldsymbol{\chi_4} & \boldsymbol{r_3}^\top \boldsymbol{\chi_5} + \boldsymbol{w_2}^\top \boldsymbol{\eta_1} & \boldsymbol{r_3}^\top \boldsymbol{\chi_6} + \boldsymbol{w_2}^\top \boldsymbol{\eta_2} \\ \boldsymbol{r_2}^\top \boldsymbol{\chi_1} & \boldsymbol{r_2}^\top \boldsymbol{\chi_2} & \boldsymbol{r_2}^\top \boldsymbol{\chi_3} & \boldsymbol{r_2}^\top \boldsymbol{\chi_4} & \boldsymbol{r_2}^\top \boldsymbol{\chi_5} + \boldsymbol{w_3}^\top \boldsymbol{\eta_1} & \boldsymbol{r_2}^\top \boldsymbol{\chi_6} + \boldsymbol{w_3}^\top \boldsymbol{\eta_2} \\ -\boldsymbol{r_1}^\top \boldsymbol{\chi_1} & -\boldsymbol{r_1}^\top \boldsymbol{\chi_2} & -\boldsymbol{r_1}^\top \boldsymbol{\chi_3} & -\boldsymbol{r_1}^\top \boldsymbol{\chi_4} & -\boldsymbol{r_1}^\top \boldsymbol{\chi_5} + \boldsymbol{w_4}^\top \boldsymbol{\eta_1} & -\boldsymbol{r_1}^\top \boldsymbol{\chi_6} + \boldsymbol{w_4}^\top \boldsymbol{\eta_2} \\ \boldsymbol{\beta_1}^\top \boldsymbol{\chi_1} & \boldsymbol{\beta_1}^\top \boldsymbol{\chi_2} & \boldsymbol{\beta_1}^\top \boldsymbol{\chi_3} & \boldsymbol{\beta_1}^\top \boldsymbol{\chi_4} & \boldsymbol{\beta_1}^\top \boldsymbol{\chi_5} + \boldsymbol{w_5}^\top \boldsymbol{\eta_1} & \boldsymbol{\beta_1}^\top \boldsymbol{\chi_6} + \boldsymbol{w_5}^\top \boldsymbol{\eta_2} \\ \boldsymbol{\beta_2}^\top \boldsymbol{\chi_1} & \boldsymbol{\beta_2}^\top \boldsymbol{\chi_2} & \boldsymbol{\beta_2}^\top \boldsymbol{\chi_3} & \boldsymbol{\beta_2}^\top \boldsymbol{\chi_4} & \boldsymbol{\beta_2}^\top \boldsymbol{\chi_5} + \boldsymbol{w_6}^\top \boldsymbol{\eta_1} & \boldsymbol{\beta_2}^\top \boldsymbol{\chi_6} + \boldsymbol{w_6}^\top \boldsymbol{\eta_2} \end{bmatrix}, \tag{3.91}$$

where

$$\begin{aligned}\boldsymbol{\eta_1} &= \alpha_1 \boldsymbol{\chi_1} + \alpha_2 \boldsymbol{\chi_2} + \boldsymbol{\chi_3}, \\ \boldsymbol{\eta_2} &= \alpha_3 \boldsymbol{\chi_1} + \alpha_4 \boldsymbol{\chi_2} + \boldsymbol{\chi_4}, \\ \boldsymbol{\beta_1} &= \alpha_1 \boldsymbol{w_1} + \alpha_2 \boldsymbol{w_2} + \boldsymbol{w_3}, \\ \boldsymbol{\beta_2} &= \alpha_3 \boldsymbol{w_1} + \alpha_4 \boldsymbol{w_2} + \boldsymbol{w_4}.\end{aligned} \tag{3.92}$$

The compliance matrix is then defined as:

$$\mathbf{S} = \left(\boldsymbol{\Phi_1^{-1}}\right)^\top \boldsymbol{\Phi_3} \boldsymbol{\Phi_1^{-1}}. \tag{3.93}$$

The 6×6 Timoshenko stiffness matrix of the cross-section is defined as:

$$\mathbf{K}_{\text{cs}} = \mathbf{S^{-1}} = \boldsymbol{\Phi_1} \boldsymbol{\Phi_3^{-1}} \boldsymbol{\Phi_1}^\top. \tag{3.94}$$

3.B. RIGID BODY MOTION RELATIONS

Starting with the rigid body translation by considering a unit translation ($u = 1$) in the x direction:

$$\boldsymbol{q} = \begin{bmatrix} 1 \\ 0 \\ 0 \end{bmatrix} = \boldsymbol{t_1} \quad , \quad \boldsymbol{q'} = \mathbf{0}. \tag{3.95}$$

The rigid body translation does not cause any deformation, so the strain will be zero ($\boldsymbol{\varepsilon} = \mathbf{0}$):

$$\mathbf{B_0}\boldsymbol{t_1} = \begin{bmatrix} \frac{\partial 1}{\partial x} \\ 0 \\ 0 \\ 0 \\ 0 \\ 0 \end{bmatrix} = \mathbf{0}. \tag{3.96}$$

Similarly, considering a unit translation ($v = 1$) in the y direction.

$$\boldsymbol{t_2} = \begin{bmatrix} 0 \\ 1 \\ 0 \end{bmatrix}, \quad \mathbf{B_0}\boldsymbol{t_2} = \mathbf{0}. \tag{3.97}$$

Finally, considering a unit translation ($w = 1$) in the z direction.

$$\boldsymbol{t_3} = \begin{bmatrix} 0 \\ 0 \\ 1 \end{bmatrix}, \quad \mathbf{B_0}\boldsymbol{t_3} = \mathbf{0}. \tag{3.98}$$

Now for the rigid rotations, consider that around the z axis:

$$\boldsymbol{q} = \begin{bmatrix} -y \\ x \\ 0 \end{bmatrix} = \boldsymbol{r_3}, \quad \boldsymbol{q'} = \mathbf{0}, \tag{3.99}$$

where the positive velocity in the x direction due to rotation around the z axis is proportional to the distance in the negative y direction.

The strains are then defined as follows:

$$\mathbf{B_0}\boldsymbol{r_3} = \begin{bmatrix} \frac{\partial(-y)}{\partial x} \\ \frac{\partial x}{\partial y} \\ 0 \\ \frac{\partial 0}{\partial y} \\ \frac{\partial 0}{\partial x} \\ \frac{\partial(-y)}{\partial y} + \frac{\partial x}{\partial x} \end{bmatrix} = \mathbf{0}. \tag{3.100}$$

The rigid rotation around the x axis is defined as follows:

$$\boldsymbol{q} = \begin{bmatrix} 0 \\ -z \\ y \end{bmatrix} = \begin{bmatrix} 0 \\ 0 \\ y \end{bmatrix} + z \begin{bmatrix} 0 \\ -1 \\ 0 \end{bmatrix} = \boldsymbol{r_1} - z\,\boldsymbol{t_2} \tag{3.101}$$

which leads to:

$$\boldsymbol{q'} = -\boldsymbol{t_2} \tag{3.102}$$

Substituting Equations 3.101, 3.102 into Equation 3.17 leads to the following relation:

$$\mathbf{B_0}\boldsymbol{r_1} = \mathbf{B_1}\boldsymbol{t_2}. \tag{3.103}$$

Finally, looking at the rotation about the y axis:

$$\boldsymbol{q} = \begin{bmatrix} 0 \\ 0 \\ -x \end{bmatrix} + z \begin{bmatrix} 1 \\ 0 \\ 0 \end{bmatrix} = \boldsymbol{r_2} + z\,\boldsymbol{t_1} \tag{3.104}$$

which similarly results in the following:

$$\mathbf{B_0}\boldsymbol{r_2} = -\mathbf{B_1}\boldsymbol{t_1}. \tag{3.105}$$

From Equations 3.96, 3.97, 3.98 and 3.100, it is concluded that $\{\boldsymbol{t_1}, \boldsymbol{t_2}, \boldsymbol{t_3}, \boldsymbol{r_3}\}$ are in the null space of $\mathbf{B_0}$. From Equation 3.22, the following relations can be drawn:

$$\mathbf{K_{00}}\boldsymbol{t_1} = \mathbf{K_{00}}\boldsymbol{t_2} = \mathbf{K_{00}}\boldsymbol{t_3} = \mathbf{K_{00}}\boldsymbol{r_3} = \mathbf{0} \tag{3.106}$$

Consequently, $\{\boldsymbol{t_1}, \boldsymbol{t_2}, \boldsymbol{t_3}, \boldsymbol{r_3}\}$ are in the null space of $\mathbf{K_{00}}$, which means that $\mathbf{K_{00}}$ is singular.

The same vectors are also in the null space of $\mathbf{K_{10}}$:

$$\mathbf{K_{10}}\boldsymbol{t_1} = \mathbf{K_{10}}\boldsymbol{t_2} = \mathbf{K_{10}}\boldsymbol{t_3} = \mathbf{K_{10}}\boldsymbol{r_3} = \mathbf{0} \tag{3.107}$$

Similarly, from Equations 3.103, 3.105, the following relations can be drawn:

$$\mathbf{K_{01}}\boldsymbol{t_1} = -\mathbf{K_{00}}\boldsymbol{r_2}, \quad \mathbf{K_{01}}\boldsymbol{t_2} = \mathbf{K_{00}}\boldsymbol{r_1}, \tag{3.108}$$

Also,

$$\mathbf{K_{11}}\boldsymbol{t_1} = -\mathbf{K_{10}}\boldsymbol{r_2}, \quad \mathbf{K_{11}}\boldsymbol{t_2} = \mathbf{K_{10}}\boldsymbol{r_1}. \tag{3.109}$$

4

Postbuckling-Enabled Aeroelastic Optimisation of Composite Wings

The effect of postbuckling on the aeroelastic design of composite wings is investigated through a controlled three-case optimisation study applied to the FLEXOP demonstrator wing. The cases are designed to investigate the effect of removing the buckling constraint and to compare designs with and without physically consistent postbuckling stiffness degradation. The postbuckling model developed in Chapter 3 is embedded within the Proteus aeroelastic framework, capturing local panel stiffness degradation at the cross-sectional level and propagating it to the coupled aeroelastic response while retaining the computational efficiency required for use within an optimisation loop. For the demonstrator wing and load cases considered, removing the buckling constraint yields a structural mass reduction of approximately 50% relative to the conventional buckling-constrained design, the reduction being limited by the minimum thickness bound rather than by postbuckling capacity. The physically consistent postbuckling case converges to essentially the same structural mass as the case without postbuckling physics, with postbuckling stiffness degradation activating the strength constraint rather than the aeroelastic stability boundary. This constitutes a fundamental shift in the governing failure mode, from aeroelastic instability to material failure, driven solely by the physically consistent representation of postbuckling stiffness degradation. Postbuckling stiffness degradation is shown to substantially modify the aeroelastic response of the wing, independently of the mass reduction achieved by removing the buckling constraint. The results demonstrate that the conventional treatment of buckling as a hard design limit imposes a significant mass penalty and that postbuckling-enabled aeroelastic optimisation can substantially reduce structural mass while maintaining a physically consistent and aeroelastically stable design.

4.1. INTRODUCTION

The structural design of thin-walled composite wings in aeroelastic optimisation frameworks is typically governed by stability considerations. Buckling emerges as the first active constraint in mass minimisation problems and directly limits panel thicknesses and laminate stiffness distributions (Sodja et al., 2018, Dillinger et al., 2019). As a result, the structural response is restricted to the pre-buckling regime, consistent with classical composite design practice (Kassapoglou, 2010). Composite materials offer anisotropic stiffness properties that enable aeroelastic tailoring, and their benefits in terms of structural mass reduction, load alleviation, and flutter performance have been demonstrated extensively (Shirk et al., 1986, Weisshaar and Duke, 2006, Najmi et al., 2024). Aeroelastic optimisation frameworks differ in structural fidelity: high-fidelity approaches rely on shell finite element models with adjoint-based sensitivity analysis (Stanford et al., 2015, Dillinger et al., 2019), while reduced-order approaches represent the three-dimensional wingbox by a one-dimensional beam coupled with cross-sectional analysis, parametrising the structural design using lamination parameters and panel thicknesses to enable gradient-based optimisation with a large number of design variables (De Breuker, 2011, Werter and De Breuker, 2016, Sodja et al., 2018, Wang et al., 2022). The restriction of the structural response to the pre-buckling regime within both classes of framework is, however, conservative. Thin-walled composite structures can sustain load beyond buckling onset through stable postbuckling behaviour (Kassapoglou, 2010, Elalfy et al., 2026), indicating that a portion of the available load-carrying capacity remains unexploited when buckling is enforced as a hard design limit.

Operating beyond initial buckling introduces effects that extend beyond the structural domain. When a panel buckles locally, its stiffness is reduced and in-plane loads are redistributed towards the supported boundaries. This local stiffness degradation modifies the global structural response of the wing, altering natural frequencies, mode shapes, and the spanwise load distribution, with measurable consequences for aeroelastic stability and flutter behaviour (Oliveira et al., 2014). Accurately incorporating these effects within an aeroelastic analysis therefore requires that postbuckling stiffness degradation be reflected at the level of the structural model, not treated solely as a constraint boundary. Recent developments have incorporated large-deformation geometric nonlinearities within multidisciplinary aeroelastic optimisation frameworks (Farsadi et al., 2024), reflecting a growing recognition of the role of nonlinear structural effects in wing design. These approaches address global kinematic nonlinearity, however, and do not account for local panel postbuckling or the associated stiffness degradation.

In aeroelastic optimisation frameworks, buckling is imposed as a hard sizing constraint, directly limiting panel thicknesses and laminate stiffness distributions, whether in reduced-order beam-based frameworks (Sodja et al., 2018, Othman et al., 2019) or in higher-fidelity shell finite element formulations (Stodieck et al., 2017, Kenway et al., 2014). Efforts to exploit postbuckling within structural optimisation have been reported using exact strip methods at the panel level (Qu et al., 2012), semi-analytical effective-width models embedded within finite element frameworks (Daoud and Calomfirescu, 2010), and analytical plate stability equations with

stiffness-reduction approaches (Moors et al., 2019). Reported mass reductions reach up to 44%, yet these studies remain limited to structural optimisation and do not account for aeroelastic effects.

High-fidelity aeroelastic analyses have demonstrated the influence of postbuckling on wing structural response and flutter behaviour (Oliveira et al., 2014), although such studies rely on computationally expensive nonlinear finite element models and are not suitable for integration within design optimisation frameworks. More recently, Mitrotta et al. (2025) demonstrated within a structural optimisation context that conventional linear buckling constraints impose an overly conservative limit on the exploitable load-carrying capacity. This was achieved by replacing the linear buckling constraint with a nonlinear structural stability criterion based on monitoring the positive-definiteness of the tangent stiffness matrix along the equilibrium path. The approach achieved a mass reduction of approximately 10.9% on an idealised CRM wingbox. This result quantifies the mass penalty associated with the conventional treatment of buckling in structural design and motivates its investigation within an aeroelastic optimisation context. The stability criterion relies, however, on arc-length path-following evaluated using a gradient-free optimiser, a combination that is not compatible with the repeated coupled analyses required within reduced-order aeroelastic optimisation loops. The extension to coupled aeroelastic optimisation is identified by the authors as an open problem. Accordingly, the consistent incorporation of postbuckling behaviour within computationally efficient, coupled aeroelastic optimisation frameworks remains limited.

The present work addresses this limitation by embedding the postbuckling model developed in Elalfy et al. (2026) within Proteus (De Breuker, 2011). Proteus is a coupled aeroelastic framework based on a one-dimensional beam structural model and a vortex lattice aerodynamic model (Werter, 2017). Gradient-based optimisation is employed, with lamination parameters and panel thicknesses as design variables, subject to strain, aeroelastic stability, and angle of attack constraints. The effect on the aeroelastic design of composite wings is investigated through a mass minimisation study applied to the FLEXOP demonstrator wing (Sodja et al., 2018). The study quantifies the structural mass penalty imposed by the conventional buckling constraint and examines whether physically consistent postbuckling stiffness degradation imposes an additional mass penalty.

The remainder of this chapter is organised as follows. Section 4.2 presents the postbuckling-enabled optimisation framework, the case study selection, and the aeroelastic analysis and design parametrisation. Section 4.3 presents and discusses the optimisation convergence, active constraint behaviour, optimised structural mass, and aeroelastic response across the three cases. Finally, Section 4.4 summarises the main conclusions.

4.2. Methodology

The effect of postbuckling on the aeroelastic design is investigated through a controlled three-case comparison applied to the FLEXOP demonstrator wing (Sodja et al., 2018) under a set of representative load cases. The three cases, summarised in Table 4.1, differ in a single modelling choice at each step, so that the comparison

between Cases 1 and 2 isolates the effect of removing the buckling constraint and the comparison between Cases 2 and 3 isolates the effect of representing the resulting postbuckling stiffness degradation. The structural parametrisation and aeroelastic analysis setup are discussed in the subsections that follow.

Table 4.1: Summary of the three optimisation cases.

Case	Buckling constraint	Postbuckling	Role
1	Enforced	Not modelled	Buckling-constrained reference
2	Removed	Not modelled	Constraint removed, no stiffness degradation
3	Removed	Modelled	Physically consistent postbuckling design

4.2.1. POSTBUCKLING-ENABLED OPTIMISATION FRAMEWORK

The aeroelastic optimisation is performed using the Globally Convergent Method of Moving Asymptotes (GCMMA) (Svanberg, 2002), a gradient-based algorithm suitable for problems with a large number of design variables, and applied across three cases. In Case 1, all conventional constraints including a buckling constraint are enforced, serving as the reference design. Cases 2 and 3 both remove the buckling constraint, with Case 3 additionally incorporating the postbuckling behaviour developed in Chapter 3, providing a physically consistent postbuckling-enabled design. The structural design is parametrised in terms of lamination parameters and panel thicknesses within predefined design regions, enabling a continuous representation of the composite layup compatible with gradient-based optimisation. As such, the optimisation can be interpreted within an aeroelastic tailoring framework, where the structural design is adapted to achieve favourable aeroelastic behaviour.

For each design region $k = 1, \ldots, N_r$, the design variable vector is defined as:

$$\boldsymbol{x}_k = \left(V_{1A}^k,\, V_{2A}^k,\, V_{3A}^k,\, V_{4A}^k,\, V_{1D}^k,\, V_{2D}^k,\, V_{3D}^k,\, V_{4D}^k,\, h^k\right), \tag{4.1}$$

where h^k is the panel thickness of design region k. The lamination parameters are defined as (Dillinger, 2014):

$$\left(V_{1A}^k, V_{2A}^k, V_{3A}^k, V_{4A}^k\right) = \frac{1}{h^k} \int_{-h^k/2}^{h^k/2} \left(\cos 2\theta,\, \sin 2\theta,\, \cos 4\theta,\, \sin 4\theta\right) dz, \tag{4.2}$$

$$\left(V_{1D}^k, V_{2D}^k, V_{3D}^k, V_{4D}^k\right) = \frac{12}{(h^k)^3} \int_{-h^k/2}^{h^k/2} z^2 \left(\cos 2\theta,\, \sin 2\theta,\, \cos 4\theta,\, \sin 4\theta\right) dz, \tag{4.3}$$

where $\theta(z)$ is the local ply orientation through the laminate thickness. Symmetric laminates are assumed throughout, such that the coupling stiffness matrix $\mathbf{B} = \mathbf{0}$ and the associated lamination parameters $V_{(1,2,3,4)B}$ vanish identically.

The optimisation problem is stated as:

$$\begin{aligned} \min_{\boldsymbol{x}} \quad & m(\boldsymbol{x}) && (4.4)\\ \text{subject to} \quad & g_{\text{lp}}(\boldsymbol{x}) \leq 0, && (4.5)\\ & g_{\text{str}}(\boldsymbol{x}) \leq 0, && (4.6)\\ & g_{\text{buc}}(\boldsymbol{x}) \leq 0 \quad \text{(Case 1 only)}, && (4.7)\\ & g_{\text{stab}}(\boldsymbol{x}) \leq 0, && (4.8)\\ & g_{\text{aoa}}(\boldsymbol{x}) \leq 0, && (4.9)\\ & h_{\min} \leq h^k \leq h_{\max}, \quad k = 1, \ldots, N_r, && (4.10) \end{aligned}$$

where $m(\boldsymbol{x})$ is the structural mass of the wingbox, and $h_{\min}$ and $h_{\max}$ denote the minimum and maximum allowable panel thickness, respectively. The individual constraints are defined as follows.

The *lamination parameter feasibility* constraint g_{lp} enforces that the lamination parameters correspond to a physically realisable laminate, following the feasibility conditions derived in Dillinger (2014).

The *strain* constraint g_{str} is based on a failure index r_{str}, defined as the ratio of the actual strain vector to the boundary of a convex failure envelope constructed from the Tsai-Wu first-ply failure criterion, accounting for all possible fibre orientations (Dillinger, 2014):

$$g_{\text{str}}(\boldsymbol{x}) = r_{\text{str}}(\boldsymbol{x}) - 1 \leq 0, \tag{4.11}$$

where $r_{\text{str}} \leq 1$ denotes the structurally feasible region and $r_{\text{str}} > 1$ indicates strain failure.

The *buckling* constraint g_{buc} is expressed in terms of an inverse buckling factor r_{buc}, defined as the ratio of the applied in-plane load to the critical buckling load of each skin panel, idealised as a simply supported flat plate (Dillinger, 2014):

$$g_{\text{buc}}(\boldsymbol{x}) = r_{\text{buc}}(\boldsymbol{x}) - 1 \leq 0, \tag{4.12}$$

where r_{buc} is obtained by solving the panel-level eigenvalue problem:

$$(\mathbf{K}_g - r_{\text{buc}}\,\mathbf{K})\,\boldsymbol{a} = \mathbf{0}, \tag{4.13}$$

with $\mathbf{K}$ and $\mathbf{K}_g$ the panel elastic stiffness and geometric stiffness matrices, and $\boldsymbol{a}$ the buckling mode shape vector, respectively (Dillinger, 2014). This constraint is enforced in Case 1 only and removed in Cases 2 and 3.

The *aeroelastic stability* constraint g_{stab} restricts the real part of the eigenvalues of the linearised aeroelastic state matrix $\mathbf{A}_{ss}$, evaluated at each flight condition (Werter, 2017, Sodja et al., 2018):

$$g_{\text{stab}}(\boldsymbol{x}) = \max_i \, \text{Re}\,(\lambda_i) \leq 0, \tag{4.14}$$

where λ_i are the eigenvalues of $\mathbf{A}_{ss}$. Flutter onset corresponds to $\text{Re}(\lambda_i) = 0$ for any aeroelastic mode i.

The *angle of attack* constraint g_{aoa} imposes an upper bound on the trim angle of attack α, which is obtained as part of the coupled aeroelastic equilibrium solution at each load case (De Breuker, 2011) and subsequently enforced as an explicit inequality constraint within the optimisation loop:

$$g_{\text{aoa}} = \alpha - \alpha_{\max} \leq 0, \tag{4.15}$$

where $\alpha_{\max} = 15$ deg.

With the constraint set defined, the role of the buckling constraint within this formulation can now be examined. In conventional formulations, the buckling constraint typically emerges as the active design driver during the optimisation process (Sodja et al., 2018), thereby limiting further load-carrying capacity beyond buckling onset. This motivates the investigation of formulations in which buckling is not enforced as a constraint, enabling the optimiser to explore designs that make use of the additional load-carrying capacity available in the postbuckling regime.

Removing the buckling constraint introduces several important implications. The design can therefore enter the postbuckling regime within the design space, with the implementation of postbuckling behaviour detailed in Chapter 3. The governing mechanism of the design shifts as a result, with the strain constraint becoming more critical. As discussed in Chapter 3, postbuckling is accounted for by incorporating degraded stiffness within the buckled regions of the cross-sections, resulting in a more compliant structural response and consequently higher strain levels, which in turn increases the significance of the strain constraint in the optimisation process.

Despite the inclusion of postbuckling effects, no explicit reformulation of the sensitivity analysis is introduced. The postbuckling behaviour is incorporated at the level of the cross-sectional stiffness, as described in Chapter 3, and therefore naturally embedded within the existing structural analysis framework. As a result, the optimiser continues to operate on the updated structural response without requiring modifications to the optimisation formulation. Furthermore, as shown in Chapter 3, the tip load-displacement response does not exhibit a pronounced change in slope upon buckling onset. This indicates that local panel stiffness degradation does not abruptly alter the global structural behaviour at the beam level. Consequently, the existing gradients remain sufficiently representative of the system response for the purposes of the optimisation, although their accuracy is reduced in the postbuckling regime. This approximation primarily affects the rate of convergence rather than the ability of the optimiser to reach a feasible design. This behaviour is analogous to inexact and quasi-Newton methods, where reduced accuracy in the sensitivities may lead to slower convergence while still providing valid search directions (Nocedal and Wright, 2006).

4.2.2. Case Study Selection

The present study requires a configuration for which the aircraft mass and load cases are fully prescribed, so that the structural loads are determined independently of assumed design parameters. In the absence of a known aircraft mass, the trimmed loads depend on the assumed wing loading, and different assumptions may lead to designs governed by buckling, strength, or aeroelastic stability, making the op-

timisation conclusions configuration-dependent. It should further correspond to a buckling-driven design, where potential structural capacity remains unexploited due to the enforcement of a hard buckling limit.

The wingbox configurations examined in Chapter 3 do not satisfy these criteria. Since these configurations are derived from the literature for structural validation purposes rather than a specific aircraft application, no consistent mission or loading scenario is prescribed. Defining representative load cases, therefore requires an estimate of the aircraft mass, which is not uniquely determined in the absence of a defined aircraft configuration. It was found that, without knowing the mass, assuming a wing loading has a strong influence on the resulting structural loads and strain levels, rendering the optimisation outcomes sensitive to the assumed design parameters and limiting the generality of the conclusions.

The FLEXOP wing presented by Sodja et al. (2018) is adopted as the reference configuration for the present study, as it addresses both of the above considerations. The load cases comprise a $1g$ cruise condition and positive and negative manoeuvre load factors of $+5g$ and $-2g$. Since the $1g$ cruise condition does not govern any active constraint in the optimisation, the results presented in this study focus on the manoeuvre load cases LC2 and LC3 defined in Table 4.2.

Table 4.2: Load case definitions for the FLEXOP wing, taken from the FLEXOP project design data Sodja et al. (2018).

Load case	Load factor	EAS [m/s]	Altitude [m]
LC2	$+5g$	43.29	800
LC3	$-2g$	43.29	800

Critically, Sodja et al. (2018) demonstrated that both the reference and the aeroelastically tailored variants of this wing are governed by the buckling constraint throughout the optimisation, with most of the top and bottom skin critical in buckling under the manoeuvre load cases, while the strain constraint remains inactive. This establishes the FLEXOP wing as a representative and well-motivated test case for investigating the aeroelastic design consequences of relaxing the buckling constraint. The wing and its representation within the modelling framework are shown in Figure 4.1.

4.2.3. Aeroelastic Analysis and Design Parametrisation

Sodja et al. (2018) defined the optimisation parametrisation using a set of design regions. In the present work, the number of design regions is increased to match the structural panels bounded by adjacent ribs (rib bays), as illustrated in Figure 4.2, resulting in 24 design regions per wingbox component. The upper skin, lower skin, front spar web and rear spar web are parametrised independently, giving $N_r = 96$ design regions in total.

Having one design region per rib bay ensures that each region corresponds to a potential buckling panel. This enables a more accurate representation of local buckling behaviour within the optimisation process. The material properties correspond

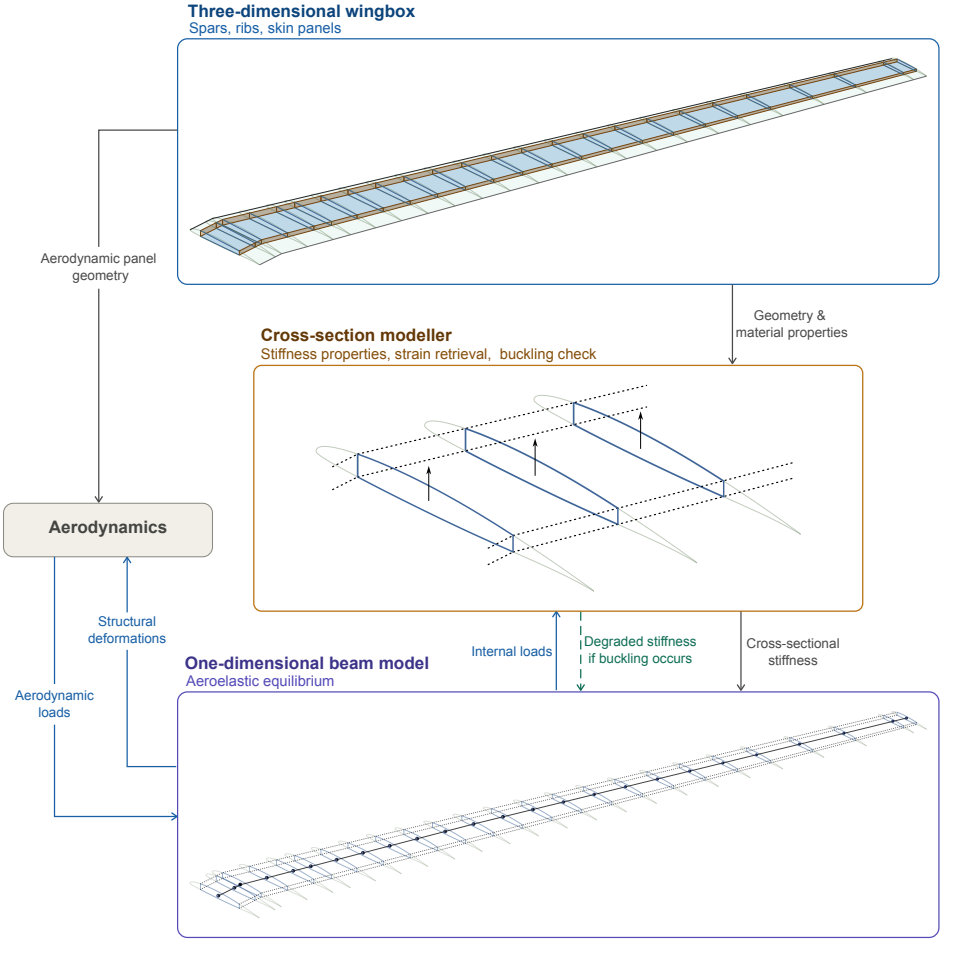

Figure 4.1: Representation of the FLEXOP demonstrator wing across the modelling levels of the aeroelastic framework.

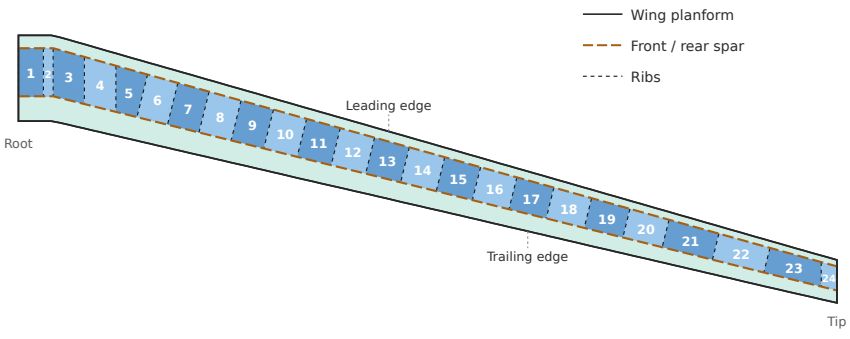

Figure 4.2: Design region distribution of the FLEXOP wing, showing the 24 rib bays used as individual design regions for each wingbox component. The front and rear spars are located at 15% and 71% chord, respectively.

to the unidirectional carbon-fibre composite FACC C 8552S/34%/UD134/AS4, as defined in Sodja et al. (2018).

The overall solution procedure is illustrated in Figure 4.3. In contrast to Chapter 3, where the structural response is evaluated under prescribed load increments, the present work adopts a velocity-based formulation. The flight velocity is incremented in steps proportional to V^2, ensuring uniform increments in dynamic pressure and consequently in aerodynamic loading.

At each velocity step, the aerodynamic forces are evaluated using a steady vortex lattice method (VLM) (Werter, 2017). The wing surface is discretised using vortex ring elements, and the resulting forces are transferred to the structural beam nodes through a spline-based coupling (Werter, 2017). The aeroelastic equilibrium is then obtained using a monolithically coupled Newton-Raphson solver (De Breuker, 2011, Werter, 2017). The trim condition requires that lift equals aircraft weight, which introduces the trim angle of attack α as an additional unknown. The structural degrees of freedom and α are therefore solved simultaneously from the augmented system (Werter, 2017):

$$\begin{bmatrix} \mathbf{J} & -\boldsymbol{f}_\alpha \\ \dfrac{\partial L}{\partial \boldsymbol{p}} & \dfrac{\partial L}{\partial \alpha} \end{bmatrix} \begin{pmatrix} \Delta \boldsymbol{p} \\ \Delta \alpha \end{pmatrix} = \begin{pmatrix} \boldsymbol{R}_0 \\ W - L(\boldsymbol{p}, \alpha) \end{pmatrix}, \tag{4.16}$$

where $\mathbf{J}$ is the aeroelastic Jacobian, $\boldsymbol{f}_\alpha = \partial \boldsymbol{F}_a / \partial \alpha$, $L(\boldsymbol{p}, \alpha)$ is the total lift, W is the aircraft weight, and $\boldsymbol{R}_0$ is the aeroelastic residual (Werter, 2017).

Each converged solution corresponds to a trimmed aeroelastic state at the current flight velocity. Panel strains are then evaluated for each panel and used to solve the eigenvalue problem of Equation 2.32 in Chapter 2. The onset of buckling is detected when $r_{\text{buc}} > 1$. If no buckling is detected, the velocity is advanced by a fixed step size proportional to V^2 and the procedure repeats from the aerodynamic model. If

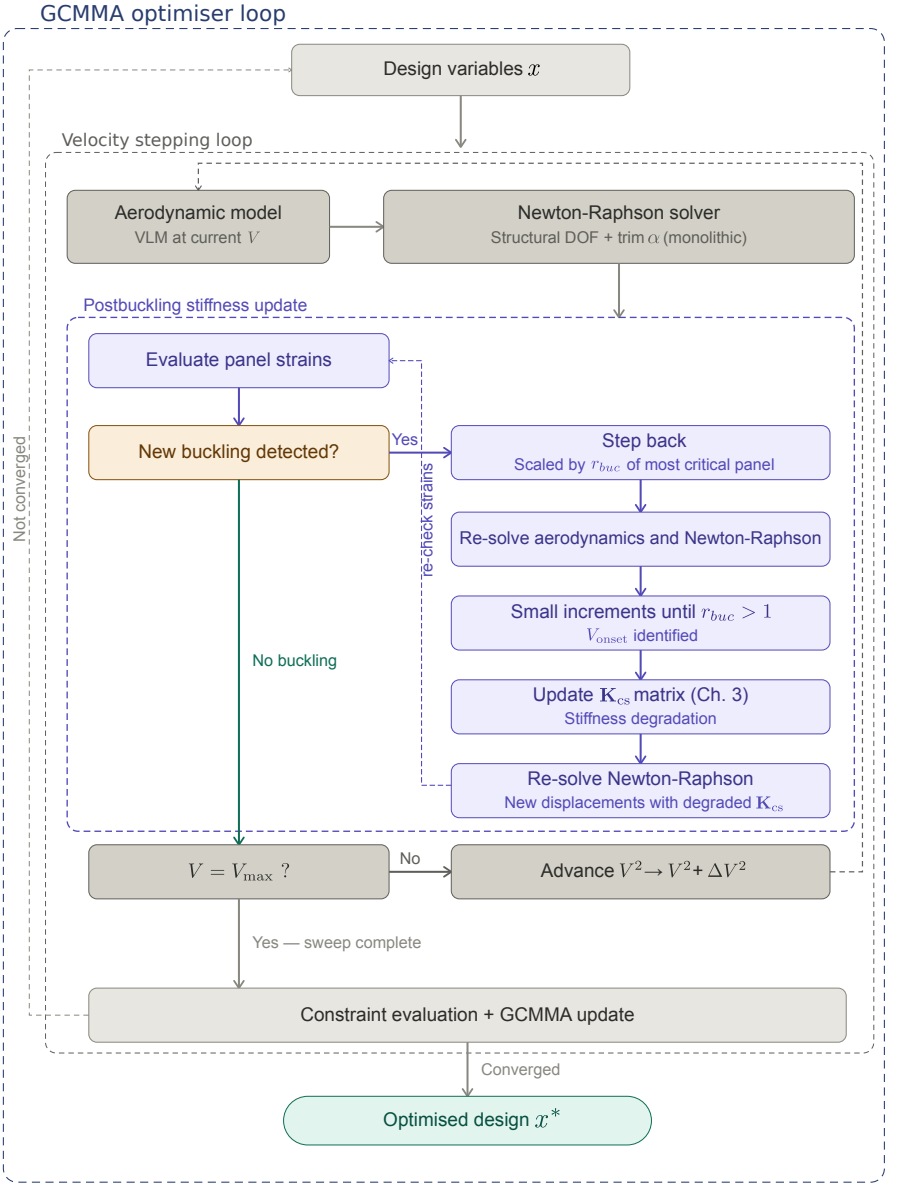

Figure 4.3: Solution procedure for the postbuckling-enabled aeroelastic optimisation of the FLEXOP wing.

buckling is detected, a step-back inversely proportional to r_{buc} of the most critical panel is applied, returning the solution to a velocity just before the buckling onset. Small fixed increments are then applied until the onset of buckling at velocity V_{onset}. The post-buckled in-plane stiffness matrix $\mathbf{A}_{\text{PB}}$ of Equation 3.11 is evaluated at the panel strain state at V_{onset} and used to update $\mathbf{K}_{\text{cs}}$ of Equation 3.94. The Newton-Raphson solver is then re-run at V_{onset} with the updated $\mathbf{K}_{\text{cs}}$, yielding updated displacements and strains. The eigenvalue problem of Equation 2.32 is then re-evaluated, as the load redistribution following the first buckling event may drive additional panels into buckling. The velocity sweep then continues from V_{onset} with the normal step size resumed.

4.3. Results

The results of the three optimisation cases, summarised in Table 4.1, are presented and discussed in the following subsections.

4.3.1. Optimisation Convergence

The convergence histories of the three cases are summarised in Table 4.3, reporting the converged structural mass and the number of outer iterations required.

Table 4.3: Optimisation convergence summary for all three cases. Mass reduction is reported relative to Case 1 (5.15 kg).

Case	Outer iterations	Final mass [kg]	Mass reduction vs. Case 1 [%]
1	24	5.15	–
2	9	2.57	50.2
3	6	2.57	50.2

Case 1 converges after 24 outer iterations, reducing the structural mass from 17.40 kg to 5.15 kg, as shown in Figure 4.4. The convergence exhibits two distinct phases. In the first phase, spanning outer iterations 1 to 8, the buckling constraint is directly active and drives a rapid reduction in structural mass as the optimiser aggressively reduces panel thicknesses to their buckling limit. In the second phase, spanning outer iterations 9 to 24, the rate of reduction decreases markedly. The buckling constraint has by this point shaped the design into a tightly constrained region where the lamination parameter feasibility constraints become the most critical at each accepted iterate, with margins close to zero. The limited gradient signal available in this region results in small, incremental design updates until convergence is declared. The slow convergence tail is therefore a consequence of the tight constraint landscape imposed by the buckling-driven design, rather than a change in the governing design mechanism.

The inner loop behaviour reflects this picture. During the first phase, each outer iteration starts with a large number of violated constraints in the inner loop. These violations are consistently resolved before the outer iterate is accepted, confirming

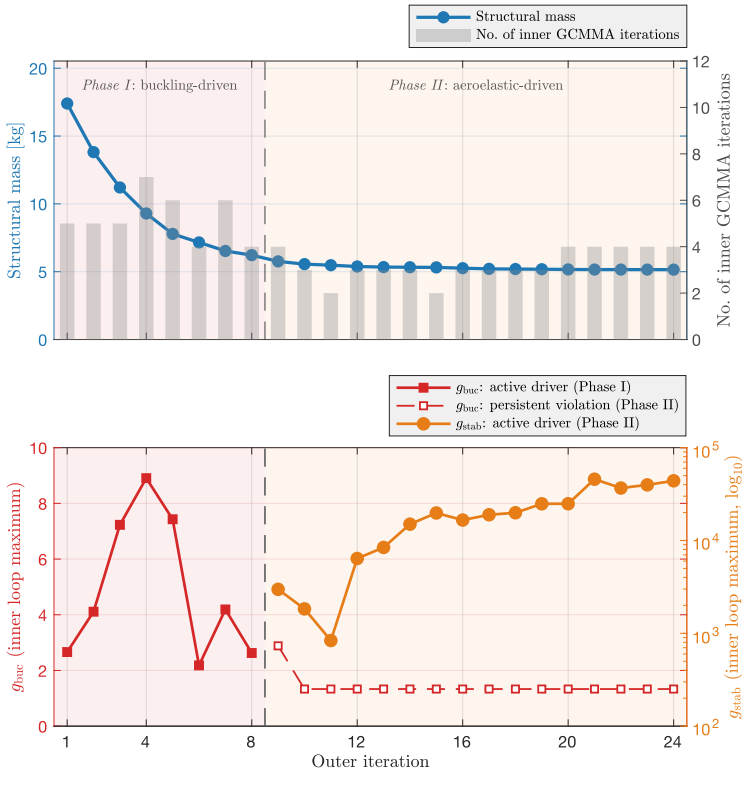

Figure 4.4: Convergence history for Case 1: structural mass and inner GCMMA iteration count per outer iteration (top), and active violated constraint per outer iteration (bottom). The dashed vertical line marks the boundary between the buckling-driven and aeroelastic-driven convergence phases. The bottom panel uses a dual axis: g_{buc} values (left, linear) g_{stab} values (right, $\log_{10}$) at the inner loop maximum.

that every accepted design remains feasible. From outer iteration 9 onward, the aeroelastic stability constraint appears as the most violated constraint at the start of the inner loop, indicating that the optimiser regularly proposes design updates that would violate the stability margin. GCMMA corrects these updates before acceptance, and all converged designs remain aeroelastically stable throughout.

Cases 2 and 3 converge substantially faster, in 9 and 6 outer iterations respectively. In Case 2, the removal of the buckling constraint eliminates the dominant source of constraint violations in the inner loop. The violations that do occur are limited to lamination parameter feasibility constraints and are resolved within one or two inner iterations. The optimiser approaches the aeroelastic stability boundary efficiently without the constraint landscape complexity characteristic of Case 1. The convergence behaviour of Case 2 is summarised in Figure 4.5.

Case 3 achieves the fewest outer iterations, but the inner loop at outer itera-

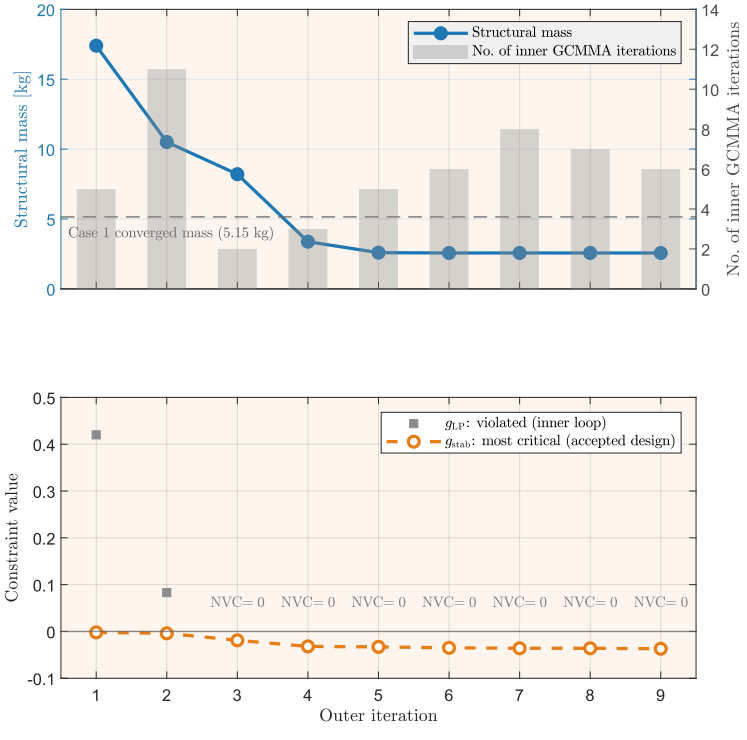

Figure 4.5: Convergence history for Case 2: structural mass and inner GCMMA iteration count per outer iteration (top), and constraint activity per outer iteration (bottom). The filled marker shows the maximum violated constraint across all inner iterations; the open markers show the aeroelastic stability margin at the accepted design. The dashed horizontal line indicates the converged mass of Case 1 for reference.

tion 3 warrants closer examination. At the start of the inner loop, the aeroelastic stability constraint under the $+5g$ load case is violated; at the subsequent inner iteration, the strength constraint under the $+5g$ load case is additionally violated as the optimiser overshoots into an infeasible region, raising the number of violated constraints sharply. Feasibility is recovered within three inner iterations, as illustrated in Figure 4.6. This behaviour is a direct consequence of the approximate sensitivity treatment of the postbuckling stiffness degradation, as discussed in the methodology section. The optimiser proposes a design update based on gradients evaluated at the current stiffness state. When panels buckle and their stiffness is degraded, the resulting structural response is more compliant than predicted by the gradients, leading to higher strain levels than anticipated and a temporary violation of the strength constraint. GCMMA detects the infeasibility, tightens its asymptotes, and recovers a feasible design within three inner iterations. The rapid recovery confirms

that the approximate sensitivity treatment, while introducing a temporary violation, does not prevent convergence to a feasible and physically consistent design.

This behaviour confirms that the inclusion of postbuckling stiffness degradation tightens the feasible design space by activating the strength constraint as buckled panels lose stiffness and local strain levels rise. Convergence is reached at the same structural mass as Case 2, but with a physically consistent structural response that correctly captures the governing constraints. Neglecting stiffness degradation, as in Case 2, produces a design at the same mass that underestimates the structural response under load and therefore does not represent a valid optimised design.

4.3.2. Constraint Activity at the Optimised Design

The active constraints at the converged design are examined here in terms of their spatial distribution and physical significance, complementing the convergence behaviour discussed in the previous section.

In Case 1, the buckling constraint is the active design driver throughout the optimisation, governing the rapid mass reduction and shaping the design into a tightly constrained region where further mass reduction yields only marginal gains. The critical region migrates progressively inboard as the optimiser redistributes material from the outboard panels – which buckle first under the $+5g$ and $-2g$ load cases – toward the root. In the subsequent convergence tail, the optimiser makes incremental updates within this region until convergence is declared. The strength constraint remains inactive throughout, consistent with the findings of (Sodja et al., 2018) for the reference and tailored wings.

In Case 2, the aeroelastic stability constraint is the most critical at the converged design. The absence of the buckling constraint allows the optimiser to reduce mass substantially, until the minimum thickness bound is reached across the skin regions. Inner loop violations are limited to lamination parameter feasibility in the first two outer iterations and are absent thereafter, indicating that the optimiser operates in a feasible region throughout the majority of the optimisation. The strength constraint remains inactive throughout. The convergence behaviour is illustrated in Figure 4.5.

Despite converging to essentially the same structural mass as Case 2, the inclusion of postbuckling stiffness degradation produces a qualitatively different constraint activity picture at the converged design. Lamination parameter feasibility constraints are violated during the inner loop at outer iterations 1 and 2. At outer iteration 3, the aeroelastic stability constraint is violated at the start of the inner loop, followed by a temporary violation of the strength constraint as the optimiser overshoots into an infeasible region; both are recovered within three inner iterations. The stiffness degradation raises local strain levels, and the strength constraint subsequently governs the converged design under the $+5g$ load case. The aeroelastic stability constraint remains at a margin comparable to that in Case 2, indicating that the strength constraint, rather than the stability boundary, would govern further mass reduction were the design not already at the minimum thickness bound. The distinction between violated constraints driving the inner loop and the most critical constraint at the accepted design is illustrated in Figure 4.6.

The difference between Cases 2 and 3 highlights that the inclusion of postbuck-

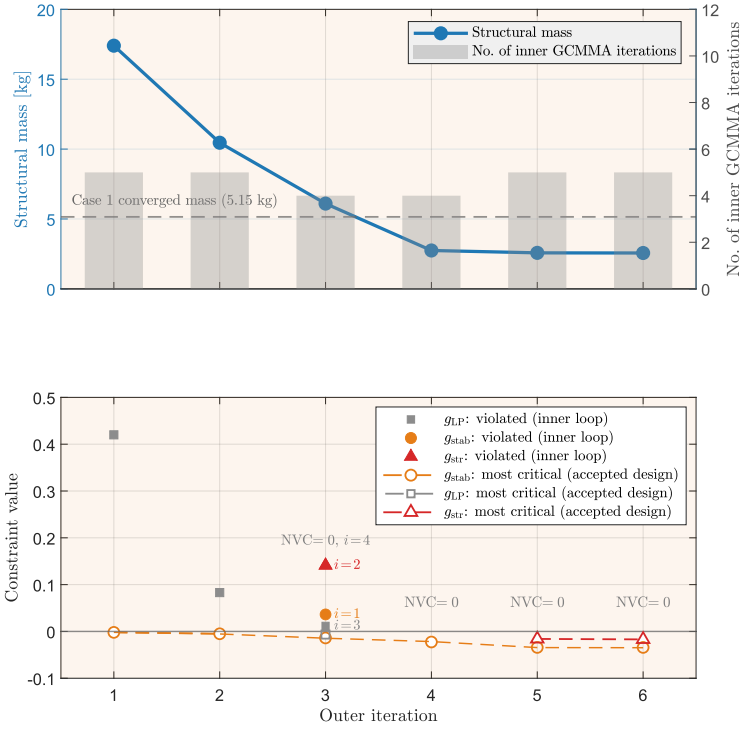

Figure 4.6: Convergence history for Case 3: structural mass and inner GCMMA iteration count per outer iteration (top), and constraint activity per outer iteration (bottom). Filled markers indicate the maximum violated constraint across all inner iterations; open markers indicate the most critical constraints at the accepted design. At outer iteration 3, individual inner iteration violations are shown and labelled by inner iteration index i. The dashed horizontal line indicates the converged mass of Case 1 for reference.

ling stiffness degradation changes the underlying structural response and, consequently, which constraint becomes active and governs the design. In Case 3, the representation of stiffness degradation leads to increased strain levels in the buckled panels, resulting in the activation of the strength constraint, which is then the most critical one at the converged design. In contrast, when this behaviour is not represented (Case 2), the structural response remains qualitatively different, and the optimiser is instead driven toward the aeroelastic stability boundary. This constitutes a fundamental shift in the governing failure mode, from aeroelastic instability to material failure, driven solely by the physically consistent representation of post-buckling stiffness degradation.

4.3.3. OPTIMISED STRUCTURAL MASS

The optimised mass values are listed in Table 4.3, where mass reductions are reported relative to Case 1. Both Cases 2 and 3 achieve a reduction of 50.2% relative to Case 1 (5.15 kg), converging to a final mass of 2.57 kg. The mass difference between Cases 2 and 3 is less than 0.1 g, so no mass penalty associated with the postbuckling stiffness degradation is observed in this configuration at the minimum thickness bound. Both Cases 2 and 3 converge to the lower thickness bound across all skin regions, with minor spar deviations inboard and at the tip. At this common mass, however, the two designs differ in their proximity to the constraint boundaries, as shown in Figure 4.5 and Figure 4.6. In Case 2 the aeroelastic stability constraint is the most critical one, whereas in Case 3 the stability margin is comparable while the strength constraint lies closer to its boundary without being reached. The penalty is therefore visible in the constraint margins rather than in the mass. A lower thickness bound would allow it to appear as a mass difference, with further reduction limited by the strength constraint in Case 3 and by the aeroelastic stability constraint in Case 2. Figure 4.7 shows the thickness distribution for Case 1, where the buckling constraint forces substantially greater material allocation across all regions.

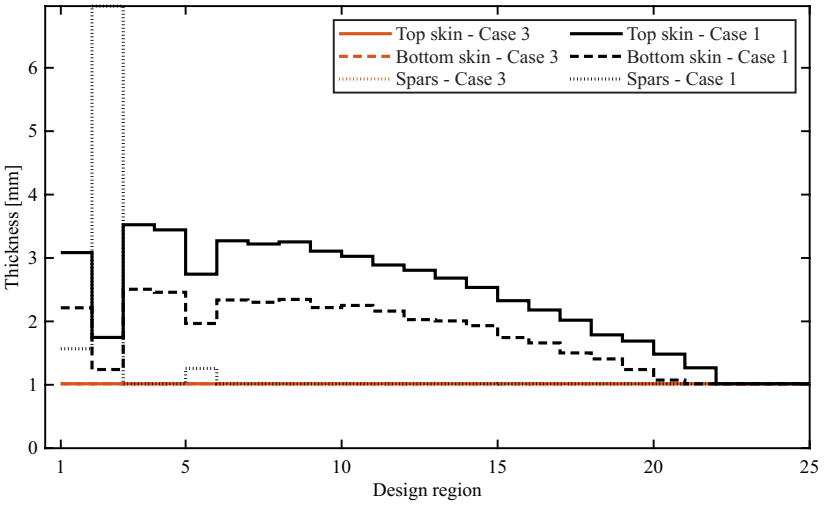

Figure 4.7: Optimised thickness distribution for Cases 1 and 3.

The strength constraint does become active in Case 3 as the reduced stiffness of buckled panels raises local strain levels, and this mechanism would impose a larger mass penalty in configurations where panels buckle at lower load levels. Case 2 does not represent this stiffness reduction and therefore produces a physically inconsistent design: the structural response under load is underestimated, allowing the same mass as Case 3 to be reached without the strength constraint becoming active. The distinction between the two cases is therefore not primarily one of mass, but of the governing failure mode and the fidelity of the predicted aeroelastic response, as

discussed in the following section.

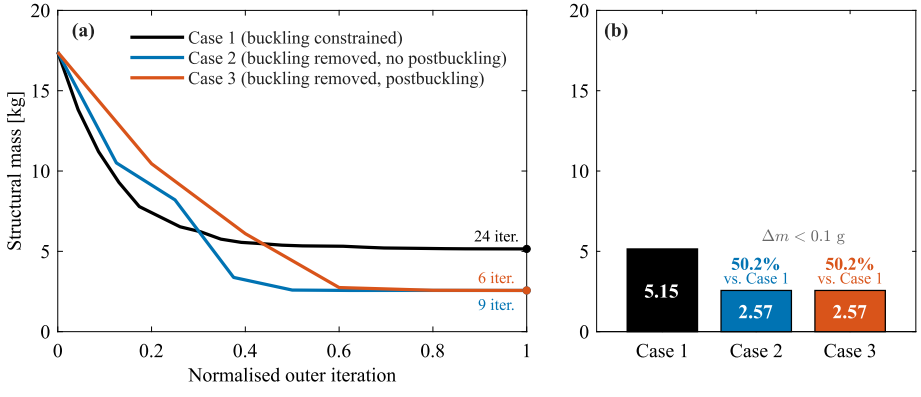

Figure 4.8: Comparison of optimised structural mass for the three cases: convergence history on a normalised iteration axis (a) and converged mass with percentage reduction relative to Case 1 (b). Labels in panel (a) indicate the total number of outer iterations.

4.3.4. Aeroelastic Response

The aeroelastic response at the converged design is compared across all three cases. The differences observed reflect the structural designs produced by the respective constraint landscapes rather than any deliberate aeroelastic tailoring.

The bending and torsional stiffness distributions at the converged designs are extracted from the cross-sectional stiffness matrix $\mathbf{K}_{\text{cs}}$. Figures 4.9 and 4.10 show the spanwise distributions of bending and torsional stiffness for all three cases. The difference between Cases 1 and 3 in both quantities is driven primarily by the large thickness difference shown in Figure 4.7, with Case 1 carrying substantially more material due to the buckling constraint. The difference between Cases 2 and 3 in bending stiffness is attributable to the postbuckling stiffness degradation in Case 3, despite the identical thickness distributions of the two cases. The stiffness degradation reduces the effective axial stiffness contribution of the buckled panels to the cross-section. The torsional stiffness, governed primarily by the enclosed wingbox area and wall thickness, is largely unaffected by panel degradation and remains nearly identical between Cases 2 and 3.

The tip displacements at the converged designs are reported in Table 4.4. Case 3 exhibits tip displacements approximately 2.5 to 2.6 times larger than Case 1 under both manoeuvre load cases, reflecting the substantially lower bending stiffness shown in Figure 4.9.

The full spanwise deflection profiles at the converged designs are shown in Figure 4.11 for both manoeuvre load cases.

The inclusion of Case 2 in Table 4.4 isolates the contribution of postbuckling stiffness degradation to the increased compliance of Case 3. Cases 2 and 3 converge to essentially the same structural mass, yet Case 3 produces a tip displacement of 0.963 m under the $+5g$ load case compared to 0.672 m in Case 2, a difference of 43%.

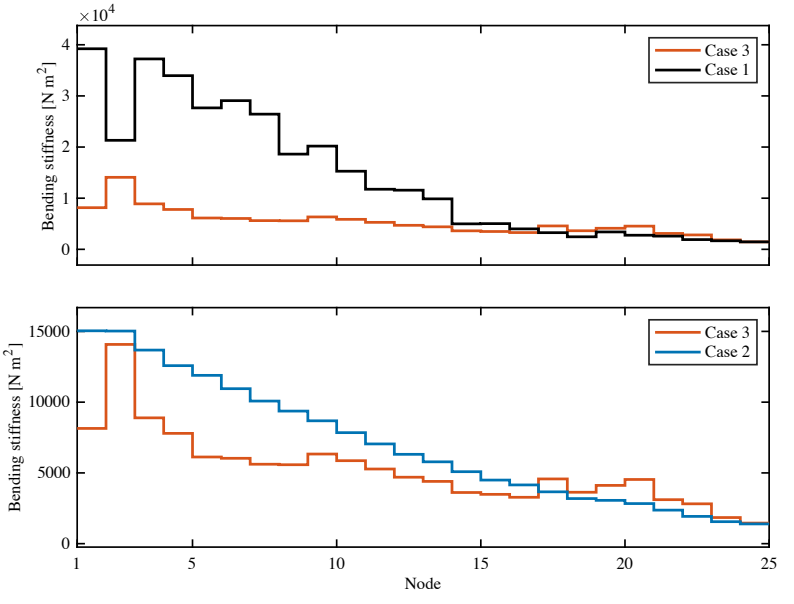

Figure 4.9: Spanwise bending stiffness distribution at the converged design.

Table 4.4: Tip out-of-plane displacement [m] at the converged design.

	LC2 ($+5g$)	LC3 ($-2g$)
Case 1	0.389	−0.150
Case 2	0.672	−0.274
Case 3	0.963	−0.391

Mass reduction alone, therefore, does not account for the increased compliance of Case 3; the postbuckling stiffness degradation is a distinct contributor.

Under the $+5g$ load case, the root bending moment is −1612 Nm in Case 3 compared to −1326 Nm in Case 1. The structural mass depends on the panel thicknesses alone. In Case 1 the laminate stiffness distribution can relax the buckling constraint and permit reduced thickness, which may provide an incentive to tailor it, whereas in Case 3 the skin thicknesses are already at their lower bound. Tailoring of this kind has been reported for this wing to promote load redistribution towards the wing root (Sodja et al., 2018). This difference reflects the aeroelastic consequences of the mass-driven design, where the optimiser reduces structural thickness without explicitly controlling the resulting deformation and load redistribution.

The maximum strain index, defined as the ratio of the maximum panel strain to the longitudinal tensile failure strain, increases from 0.273 in Case 1 to 0.650 in Case 3 under the $+5g$ load case, an increase of approximately 138%. The strain in Case 3 approaches the material allowable limit, consistent with the strength constraint being the most critical at the converged design. This stands in direct

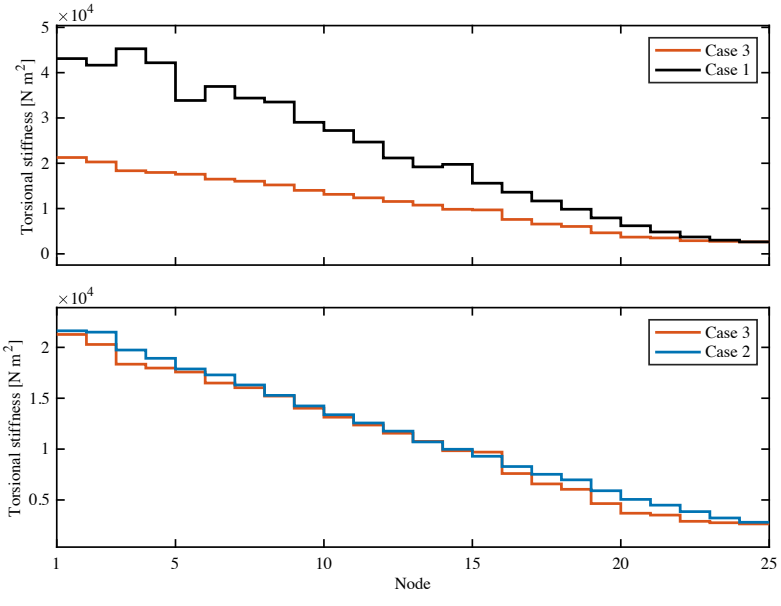

Figure 4.10: Spanwise torsional stiffness distribution at the converged design.

contrast to Case 1, where the buckling constraint governs the design and strain levels remain well below the allowable. The additional material required to satisfy the buckling constraint keeps strain levels well within the allowable in Case 1.

These observations indicate that postbuckling stiffness degradation substantially modifies the aeroelastic response of the wing in this configuration. This is consistent with previous findings on the influence of postbuckling stiffness degradation on aeroelastic behaviour (Oliveira et al., 2014).

4.4. Conclusion

We presented a postbuckling-enabled aeroelastic optimisation framework in which local panel stiffness degradation is incorporated at the cross-sectional level of a beam-based structural model and propagated to the coupled aeroelastic response within a gradient-based optimisation loop. The framework was applied to the FLEXOP demonstrator wing through a controlled three-case comparison, designed to isolate the contribution of constraint removal from the contribution of the postbuckling physics.

Removing the buckling constraint reduced the structural mass by approximately 50% relative to the conventional buckling-constrained reference, demonstrating that the conventional treatment of buckling as a hard design limit imposes a substantial mass penalty. Both the case with and without postbuckling physics converge to essentially the same structural mass, with both optimised designs driven to the lower thickness bound across all skin regions. No mass penalty associated with post-

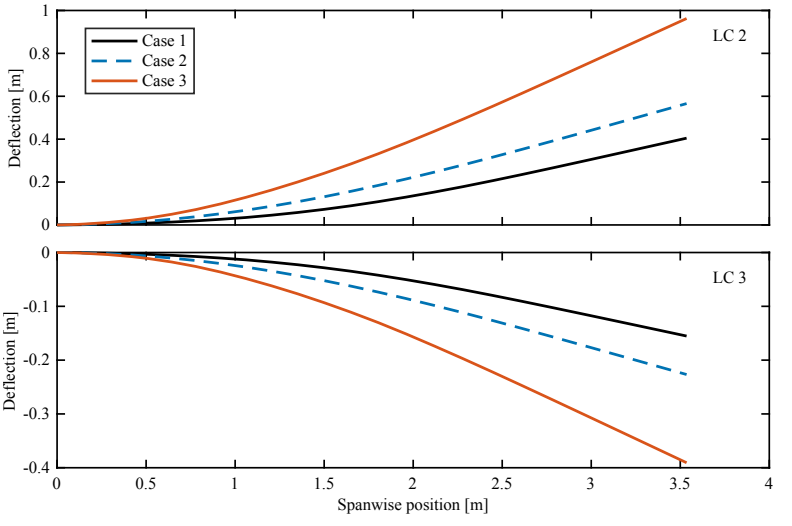

Figure 4.11: Spanwise out-of-plane deflection profiles for all three cases under LC2 ($+5g$) and LC3 ($-2g$).

buckling stiffness degradation is therefore observed at this bound. The case without postbuckling physics does not, however, represent a physically consistent design: without representing stiffness degradation, the structural response under load is underestimated and the resulting design is not sized against the response it would actually exhibit. The physically consistent postbuckling case converged in six outer iterations, substantially faster than the reference, reflecting the tightening of the feasible design space through activation of the strength constraint by the degraded panel stiffness. The inclusion of postbuckling stiffness degradation produces a fundamental shift in the governing failure mode, from aeroelastic instability to material failure, a consequence that is absent when postbuckling physics are neglected.

The postbuckling-enabled design exhibits a substantially more compliant structural response, with tip displacements approximately 2.5 to 2.6 times larger than the reference across both load cases. The root bending moment increases relative to the reference, reflecting the aeroelastic consequences of a mass-driven formulation that does not explicitly control the resulting deformation and load redistribution. At the same structural mass, the postbuckling-enabled design produces substantially larger tip displacements than the design without postbuckling physics, confirming that stiffness degradation is the dominant contributor to the increased wing compliance rather than mass reduction alone. These aeroelastic consequences are consistent with the influence of postbuckling stiffness degradation on wing structural response reported in the literature (Oliveira et al., 2014).

The present work demonstrates that postbuckling behaviour can be incorporated within a computationally efficient coupled aeroelastic optimisation framework without reformulating the sensitivity analysis, by embedding the stiffness degrada-

tion at the cross-sectional level. The approximate sensitivity treatment introduces temporary constraint violations during the optimisation, but these are recovered within three inner iterations by GCMMA, confirming that convergence to a feasible and physically consistent design is maintained. Future work should investigate the extension to explicit postbuckling sensitivity analysis to improve convergence robustness, the incorporation of aeroelastic tailoring objectives alongside mass minimisation to control the deformation response in the postbuckling regime, and the application to higher-fidelity structural representations to assess the influence of modelling assumptions on the optimised design.

Bibliography

F. Daoud and M. Calomfirescu. Optimization of composite aircraft structures in consideration of postbuckling behavior. In *International Journal of Structural Stability and Dynamics*, volume 10, pages 905–916, 10 2010. doi: 10.1142/S0219455410003804.

R. De Breuker. *Energy-based Aeroelastic Analysis and Optimisation of Morphing Wings*. PhD thesis, Delft University of Technology, 2011.

J. K. S. Dillinger. *Static Aeroelastic Optimization of Composite Wings with Variable Stiffness Laminates*. PhD thesis, Delft University of Technology, 2014.

J. K. S. Dillinger, M. M. Abdalla, Y. M. Meddaikar, and T. Klimmek. Static aeroelastic stiffness optimization of a forward swept composite wing with cfd-corrected aero loads. *CEAS Aeronautical Journal*, 10(4):1015–1032, May 2019. ISSN 1869-5590. doi: 10.1007/s13272-019-00397-y.

M. H. Elalfy, R. De Breuker, and S. G. Castro. An efficient semi-analytical approach for postbuckling analysis of laminated composite plates with straight edges. *Thin-Walled Structures*, 222:114394, 2026. ISSN 0263-8231. doi: https://doi.org/10.1016/j.tws.2025.114394.

T. Farsadi, M. Ahmadi, M. Sahin, H. Haddad Khodaparast, A. Kayran, and M. I. Friswell. High aspect ratio composite wings: Geometrically nonlinear aeroelasticity, multi-disciplinary design optimization, manufacturing, and experimental testing. *Aerospace*, 11(3), 2024. ISSN 2226-4310. doi: 10.3390/aerospace11030193.

C. Kassapoglou. *Design and Analysis of Composite Structures: With Applications to Aerospace Structures*. Wiley, Sept. 2010. ISBN 9780470972700. doi: 10.1002/9780470972700.

G. K. Kenway, J. R. Martins, and G. J. Kennedy. *Aerostructural optimization of the common research model configuration*. American Institute of Aeronautics and Astronautics Inc., 2014. ISBN 9781624102837. doi: 10.2514/6.2014-3274.

F. Mitrotta, A. Pirrera, T. Macquart, J. Cooper, A. Pereira do Prado, and P. Higino Cabral. Proof of concept of a nonlinear structural stability constraint for aeroelastic optimisation. *The Aeronautical Journal*, 129(1335):1237–1264, Jan. 2025. ISSN 2059-6464. doi: 10.1017/aer.2024.151.

G. Moors, C. Kassapoglou, S. F. M. de Almeida, and C. A. E. Ferreira. Weight trades in the design of a composite wing box: effect of various design choices. *CEAS Aeronautical Journal*, 10(2):403–417, 6 2019. ISSN 18695590. doi: 10.1007/s13272-018-0321-4.

J. Najmi, H. A. Khan, S. S. Javaid, A. Hameed, and F. Siddiqui. Aeroelastic tailoring for aerospace applications. *Heliyon*, 10(2):e24151, 2024. ISSN 2405-8440. doi: https://doi.org/10.1016/j.heliyon.2024.e24151.

J. Nocedal and S. J. Wright. *Numerical Optimization*. Springer, New York, 2nd edition, 2006.

L. C. D. Oliveira, R. Degenhardt, and T. Klimmek. Aeroelastic behavior of composite wings in post buckling regime. *29th Congress of the International Council of the Aeronautical Sciences, ICAS 2014*, pages 1–8, 2014.

M. F. Othman, G. H. Silva, P. H. Cabral, A. P. Prado, A. Pirrera, and J. E. Cooper. A robust and reliability-based aeroelastic tailoring framework for composite aircraft wings. *Composite Structures*, 208:101–113, 1 2019. ISSN 02638223. doi: 10.1016/j.compstruct.2018.09.086.

S. Qu, D. Kennedy, and C. A. Featherston. A multilevel framework for optimization of an aircraft wing incorporating postbuckling effects. *Proceedings of the Institution of Mechanical Engineers, Part G: Journal of Aerospace Engineering*, 226(7): 830–845, 7 2012. ISSN 0954-4100. doi: 10.1177/0954410011415158.

M. H. Shirk, T. J. Hertz, and T. A. Weisshaar. Aeroelastic tailoring - theory, practice, and promise. *Journal of Aircraft*, 23(1):6–18, 1986. doi: 10.2514/3.45260.

J. Sodja, N. P. Werter, and R. De Breuker. Design of a flying demonstrator wing for manoeuvre load alleviation with cruise shape constraint. In *AIAA/ASCE/AHS/ASC Structures, Structural Dynamics, and Materials Conference, 2018*, number 210049. American Institute of Aeronautics and Astronautics Inc, AIAA, 2018. ISBN 9781624105326. doi: 10.2514/6.2018-2153.

B. Stanford, C. D. Wieseman, and C. Jutte. Aeroelastic tailoring of transport wings including transonic flutter constraints. In *56th AIAA/ASCE/AHS/ASC Structures, Structural Dynamics, and Materials Conference*, Kissimmee, Florida, January 2015. American Institute of Aeronautics and Astronautics. doi: 10.2514/6.2015-1127.

O. Stodieck, J. E. Cooper, P. M. Weaver, and P. Kealy. Aeroelastic tailoring of a representative wing box using tow-steered composites. *AIAA Journal*, 55:1425–1439, 2017. ISSN 00011452. doi: 10.2514/1.J055364.

K. Svanberg. A class of globally convergent optimization methods based on conservative convex separable approximations. *SIAM Journal on Optimization*, 12(2): 555–573, 2002. doi: 10.1137/S1052623499362822.

Z. Wang, D. Peeters, and R. De Breuker. An aeroelastic optimisation framework for manufacturable variable stiffness composite wings including critical gust loads. *Structural and Multidisciplinary Optimization*, 65(10), Sept. 2022. ISSN 1615-1488. doi: 10.1007/s00158-022-03375-x.

T. A. Weisshaar and D. K. Duke. Induced drag reduction using aeroelastic tailoring with adaptive control surfaces. *Journal of Aircraft*, 43(1):157–164, 2006. doi: 10.2514/1.12040.

N. Werter. *Aeroelastic Modelling and Design of Aeroelastically Tailored and Morphing Wings*. PhD thesis, Delft University of Technology, 2017.

N. P. Werter and R. De Breuker. A novel dynamic aeroelastic framework for aeroelastic tailoring and structural optimisation. *Composite Structures*, 158:369–386, 12 2016. ISSN 02638223. doi: 10.1016/j.compstruct.2016.09.044.

5

Conclusion and Future Research

5.1. Conclusions

The effect of exploiting the load-carrying capacity beyond the onset of buckling on the structural mass of composite wings optimised within a coupled aeroelastic framework is presented in this dissertation.

5.1.1. RQ1: Efficient Prediction of Postbuckling Stiffness Under General Boundary Conditions

A semi-analytical postbuckling formulation was developed for laminated composite plates with straight edges, combining the Rayleigh–Ritz method with hierarchical polynomials as the shape functions. Replacing the trigonometric shape functions used by Seresta et al. (2008) with hierarchical polynomials yields two principal advantages: general boundary conditions are accommodated, and all strain-energy integrals are evaluated in closed form through polynomial recurrence relations, eliminating the need for numerical integration.

Two solution strategies were presented. The perturbation-based approach provided the reduced stiffness matrix through fourth-order tensor evaluations, giving a fast and closed-form approximation valid in the neighbourhood of the buckling load. Secondly, the iterative correction scheme based on the Normal Flow Algorithm traced the nonlinear equilibrium path deeper into the postbuckling regime and maintained close agreement with Abaqus across a range of laminate configurations and loading conditions.

For the intended application to wingbox-type panels, the perturbation-based solution captured the postbuckling stiffness in the main loading direction with adequate accuracy in the vicinity of the buckling load, with errors below 2% for cross-ply laminates under biaxial loading and below 20% under uniaxial loading. Deviations increase deeper into the postbuckling regime and for angle-ply laminates, where

modal interaction and increased nonlinearity exceed the validity range of the perturbation expansion, with discrepancies in $\bar{N}_x$ reaching approximately 58–59%. In a wingbox context, however, once a panel buckles locally, load redistributes to the adjacent structure, such that the perturbation solution remains a valid approximation for the stiffness reduction near the onset of buckling.

5.1.2. RQ2: Beam-Like Representation of Local Panel Postbuckling in Wingbox Structures and Its Limitations

A methodology was developed to incorporate the stiffness reduction of locally buckled panels into the cross-sectional stiffness matrix of a one-dimensional Timoshenko beam element. The semi-analytical postbuckling model of Chapter 2 provides the panel-level stiffness reduction, which is integrated into the cross-section modeller to produce a degraded 6×6 beam stiffness matrix reflecting the buckled state.

Verification against Abaqus Riks analyses across four isotropic wingbox configurations confirmed that the methodology captured the onset and progression of buckling accurately, and the global load-displacement response is tracked consistently through the postbuckling regime. Critically, the global tip load-displacement response did not exhibit a pronounced change in slope at buckling onset, and the model followed the postbuckling response consistently until cross-sectional sagging develops. This confirms that local panel stiffness degradation does not abruptly alter the global structural response at the beam level, a finding that directly underpins the approximate sensitivity treatment adopted in Chapter 4.

The identified limitation of the approach is Brazier-type cross-sectional sagging. Once the enclosed cross-sectional area begins to change, the beam model diverged from the shell-based reference, as the one-dimensional kinematic assumptions preclude the representation of cross-sectional shape change. The deviation grows as cross-sectional area loss increases.

5.1.3. RQ3: Effect of Postbuckling on Structural Mass and Aeroelastic Response

The methodology of Chapter 3 was embedded within Proteus, a reduced-order beam-based aeroelastic optimisation framework (De Breuker, 2011), and applied to the FLEXOP demonstrator wing through a controlled three-case comparison. The comparison was designed to isolate the contribution of constraint removal from the contribution of postbuckling stiffness degradation. Case 1 enforced a conventional buckling constraint and served as the reference. Case 2 removed the buckling constraint without representing postbuckling stiffness degradation. Case 3 removed the buckling constraint and incorporated the postbuckling stiffness degradation model of Chapter 3, constituting the physically consistent postbuckling-enabled design.

Several conclusions follow from this comparison.

The conventional buckling constraint imposes a substantial structural mass penalty. For the demonstrator wing and load cases considered here, removing the buckling constraint while retaining physically consistent postbuckling physics reduced the structural mass by approximately 50% relative to the conventional reference (Case 1: 5.15 kg; Case 3: 2.57 kg). This mass penalty arises because the

buckling constraint, once active, directly governs panel thicknesses and laminate stiffness distributions, preventing the optimiser from accessing designs that exploit the load-carrying capacity available beyond the onset of buckling. The 50% mass reduction achieved here is substantially larger than the 10.9% reported by Mitrotta et al. (2025), who achieved this saving by replacing the linear buckling constraint with a nonlinear structural stability criterion in a structural optimisation of an idealised metallic CRM wingbox. This difference reflects the dominant role of the buckling constraint in the beam-based aeroelastic framework and the specific characteristics of the FLEXOP configuration.

Physical consistency is required to obtain a representative design. Case 2, which removed the buckling constraint without representing stiffness degradation, converged to essentially the same structural mass as Case 3. Both designs reach the minimum thickness bound across the skin regions, so no mass penalty associated with postbuckling stiffness degradation is observed in this configuration. Without accounting for the stiffness reduction associated with buckled panels, however, the structural response under load is underestimated and the resulting design is not sized against the response it would actually exhibit. Case 2 therefore does not constitute a valid optimised design, and the distinction between Cases 2 and 3 lies not in the achieved mass but in the physical consistency of the structural response and the governing failure mode.

Postbuckling physics produce a fundamental shift in the governing failure mode. In Case 1, the buckling constraint is the active design driver throughout the optimisation. In Case 2, aeroelastic stability governs the converged design. In Case 3, the reduced stiffness of buckled panels raised local strain levels until the strength constraint was activated, which was then the most critical one at the converged design under the $+5g$ load case. This constitutes a shift in the governing failure mode from aeroelastic instability to material failure, driven solely by the physically consistent representation of postbuckling stiffness degradation.

Postbuckling stiffness degradation substantially modifies the aeroelastic response. The postbuckling-enabled design exhibited tip displacements approximately 2.5 to 2.6 times larger than the reference across both load cases (Case 3: 0.963 m versus Case 1: 0.389 m under the $+5g$ load case). The root bending moment under the $+5g$ load case increased from -1326 Nm in Case 1 to -1612 Nm in Case 3. The maximum strain index under the $+5g$ load case increased from 0.273 in Case 1 to 0.650 in Case 3, an increase of approximately 138%, approaching the material allowable limit consistently with the strength constraint being the most critical at the converged design. At the same structural mass, Case 3 produced substantially larger tip displacements than Case 2, confirming that stiffness degradation is the dominant contributor to the increased wing compliance rather than mass reduction alone.

Postbuckling behaviour can be incorporated within a computationally efficient aeroelastic optimisation framework without reformulating the sensitivity analysis. The stiffness degradation is embedded at the cross-sectional level and propagates naturally to the coupled aeroelastic response, without requiring modifications to the optimisation formulation or the adjoint-based sensitivity computation. The ap-

proximate sensitivity treatment introduces temporary constraint violations during the optimisation, but these are recovered within three inner iterations by GCMMA, confirming that convergence to a feasible and physically consistent design is maintained. This behaviour is consistent with the smooth global load-displacement response identified in Chapter 3: because local panel buckling does not produce a pronounced kink in the beam-level response, the existing sensitivities provide adequate search directions throughout the optimisation. Case 3 converges in six outer iterations, substantially fewer than the 24 required by Case 1, reflecting the tightening of the feasible design space through early activation of the strength constraint by the degraded panel stiffness.

5.1.4. Overall Conclusions

The work collectively demonstrated that postbuckling behaviour can be incorporated within a computationally efficient, gradient-based aeroelastic optimisation framework through a hierarchical modelling approach: panel-level stiffness degradation was computed semi-analytically, embedded into the beam cross-sectional stiffness, and propagated to the coupled aeroelastic response. The resulting framework is physically consistent and computationally tractable, addressing the gap identified in the literature where the extension to coupled aeroelastic optimisation had not been realised.

The results established that the conventional treatment of buckling as a hard design constraint imposes a substantial and quantifiable mass penalty, that relaxing this constraint requires physically consistent representation of the postbuckling load path to yield a valid design, and that incorporating postbuckling physics changes the governing failure mode and aeroelastic response of the wing independently of the mass reduction achieved by removing the buckling constraint.

5.2. Future Research

The limitations identified across the three research questions motivate the following directions for future work.

5.2.1. Explicit Postbuckling Sensitivity Analysis

The present work relies on approximate sensitivities that do not account for the stiffness change at buckling onset. While the results of Chapter 4 confirmed that GCMMA recovers feasibility within a small number of inner iterations, the approximate treatment reduces convergence robustness and may become inadequate for configurations where multiple panels buckle in rapid succession or where the buckling load is strongly dependent on the design variables. Developing explicit sensitivity analysis for the postbuckling stiffness degradation would improve convergence robustness and is a natural immediate extension of the present framework.

5.2.2. Aeroelastic Performance Objectives in the Postbuckling Regime

The optimisation of Chapter 4 minimised structural mass without constraints on root bending moment or cruise shape. Neither the root bending moment nor the resulting wing deformation therefore enters the constraint set, and the aeroelastic consequences of the increased compliance of the postbuckling-enabled design are not controlled by the optimiser. Incorporating such constraints within the postbuckling framework would allow the aeroelastic consequences of postbuckling compliance to be actively managed, and represents a natural extension of the present work. Control effectiveness and reversal speed are similarly not constrained: the spanwise stiffness redistribution available to the optimiser is free to trade mass against control surface performance, since no reversal margin or effectiveness requirement enters the constraint set. The comparison between Cases 1 to 3 remains internally consistent, as all three cases are optimised under the same remaining constraint set, so the relative effect of removing the buckling constraint is isolated from this omission. The absolute optimum obtained, however, is not guaranteed to preserve control effectiveness, and incorporating a reversal speed or effectiveness constraint into the optimisation is a necessary extension for the framework to produce preliminary designs that remain viable at later design stages.

5.2.3. Cross-Sectional Shape Change

Chapter 3 identifies Brazier-type cross-sectional sagging as the mechanism that limits the fidelity of the beam model at higher load levels. The cross-sectional geometry is held fixed throughout the analysis, and the deviation from the shell-based reference grows as cross-sectional area loss increases. Follower forces amplify this effect by accelerating the geometric changes through the increased bending moment, causing divergence to appear at lower load levels. Extending the framework to account for finite cross-sectional deformation would address this limitation. The nonlinear Variational Asymptotic Beam Sectional Analysis of Jiang and Yu Jiang and Yu (2024), which captures cross-sectional collapse under pure bending through a nonlinear two-dimensional cross-sectional analysis, represents a promising direction, though its applicability and performance for wingbox configurations with multiple simultaneously buckled panels remain topics for future research.

5.2.4. Fibre Path Optimisation for Strength-Critical Designs

The current straight-fibre laminate parametrisation imposes a spatially uniform in-plane stiffness distribution across each buckling panel, which cannot adapt to the non-uniform stress field that develops in the postbuckling regime, where load concentrates towards the supported edges. A finer subdivision of the design regions in the chordwise direction would allow the benefit of laminate variability across the chord to be assessed. Variable-angle tow laminates, which allow fibre orientations to be steered continuously across the panel, offer the potential to align the laminate stiffness with the redistributed postbuckling load path, reducing peak strains and expanding the feasible design space for strength-critical postbuckling designs.

5.2.5. Multifidelity Optimisation

The reduced-order beam-based framework developed in this work enables efficient design space exploration but cannot capture all three-dimensional effects of local postbuckling, as established by the verification studies of Chapter 3. Embedding the present framework within a multifidelity optimisation strategy, where the reduced-order model drives the optimisation and higher-fidelity shell-based analyses are used to correct or validate the design at selected points, would allow the computational efficiency of the beam model to be retained while managing the modelling assumptions that govern its validity.

5.2.6. Progressive Damage and Delamination

The present work employs a strain-based failure criterion that does not account for delamination, which can be initiated by the interlaminar stresses that develop in the postbuckling regime under repeated loading. The fatigue life of panels cycling through buckling and postbuckling states is similarly not addressed. Incorporating progressive damage models that capture delamination onset and growth, alongside fatigue considerations, would provide a more complete picture of the structural integrity of postbuckling-enabled designs. Resolving interlaminar stress fields requires higher-fidelity representations than the beam model can provide, reinforcing the case for the multifidelity optimisation strategy discussed above.

5.2.7. Fibre Metal Laminates

The framework presented here does not extend to fibre metal laminates. The design variables are lamination parameters defined for a single material, whereas a hybrid layup requires a parameter set per block. Silva and Meddaikar (2020) provide such an extension by superposing offset material blocks, preserving the classical form of the stiffness relations and the established feasibility conditions. Symmetric laminates are assumed here, so the coupling lamination parameters are eliminated, whereas that scheme requires the first-moment parameters of each block because the blocks are offset from the laminate mid-plane even when the overall laminate is symmetric. It also requires the material groups and their order to be prescribed.

5.2.8. Uncertainty Quantification and Reliability-Based Optimisation

The optimisation problem is formulated deterministically, with nominal material properties, nominal geometry and prescribed load cases. Postbuckling behaviour is sensitive to geometric imperfections, material scatter and manufacturing tolerances, none of which are represented. A reliability-based or robust formulation would establish the required margins explicitly and quantify the confidence with which the reported mass reductions can be realised.

Bibliography

R. De Breuker. *Energy-based Aeroelastic Analysis and Optimisation of Morphing Wings*. PhD thesis, Delft University of Technology, 2011.

F. Jiang and W. Yu. Prediction of sectional collapse of thin-walled structure under pure bending by nonlinear composite beam theory. *Thin-Walled Structures*, 205: 112414, Dec. 2024. ISSN 0263-8231. doi: 10.1016/j.tws.2024.112414.

F. Mitrotta, A. Pirrera, T. Macquart, J. Cooper, A. Pereira do Prado, and P. Higino Cabral. Proof of concept of a nonlinear structural stability constraint for aeroelastic optimisation. *The Aeronautical Journal*, 129(1335):1237–1264, Jan. 2025. ISSN 2059-6464. doi: 10.1017/aer.2024.151.

O. Seresta, M. M. Abdalla, and Z. Gürdal. Approximate internal load prediction in composite structures with locally buckled panels. *Journal of Aircraft*, 45:513–522, 2008. ISSN 15333868. doi: 10.2514/1.30465.

G. H. C. Silva and Y. Meddaikar. Lamination parameters for sandwich and hybrid material composites. *AIAA Journal*, 58(10):4604–4611, 2020. doi: 10.2514/1.J059093.

Curriculum Vitæ

Mohamed Hassan Ibrahim ELALFY

He was born on 23 April 1994 in Port-Said, Egypt. He obtained his Bachelor of Science degree in Aerospace Engineering from Zewail City University of Science and Technology, Egypt, in 2018, graduating Summa Cum Laude. His Bachelor's thesis focused on the aeroelastic analysis of a flapping wing micro-aerial vehicle, investigating the structural response of flexible wing structures under flapping motion. During his undergraduate studies, he undertook a research internship at the University of Illinois at Urbana-Champaign (UIUC), USA, in 2017, where he contributed to the implementation of a nonlinear thermo-mechanical constitutive model, resulting in a peer-reviewed publication.

He obtained his Master of Science degree in Aerospace Engineering from Cairo University, Egypt, in 2021, under the supervision of Dr. Mostafa Abdallah. His Master's thesis focused on the numerical generation of omnistrain failure envelopes for composite laminates, developing ply-independent failure criteria through micro-mechanical modelling and parametric finite element simulations, which resulted in a peer-reviewed publication in the *Journal of Composite Materials*.

In 2022, he joined the Department of Aerospace Structures and Materials at Delft University of Technology, The Netherlands, as a PhD candidate under the supervision of Prof. dr. Roeland De Breuker and Dr. Saullo G. P. Castro. His doctoral research focused on the development of computationally efficient frameworks for postbuckling analysis of composite structures and their integration into aeroelastic optimisation, demonstrating structural weight savings achievable by exploiting load-carrying capacity beyond initial buckling.

TU Delft

ISBN 978-94-6518-442-5